Tolerable Experimental Imperfections for a Quadrupole Blade Ion Trap and Practical Qudit Gates with Trapped Ions

by

Pei Jiang Low

A thesis
presented to the University of Waterloo
in fulfillment of the
thesis requirement for the degree of
Master of Science
in
Physics

Waterloo, Ontario, Canada, 2019

Author's Declaration

I hereby declare that I am the sole author of this thesis. This is a true copy of the thesis, including any required final revisions, as accepted by my examiners.

I understand that my thesis may be made electronically available to the public.

Abstract

Trapped ions are one of the leading technologies in quantum information technology due to their long coherence time and low noise presence. For trapping ions, there are a plethora of ion trap architectures. Among them is a quadrupole blade trap design, which has the benefit of large optical access from all axes. It has also been shown to be able to trap up to 100 ions. This thesis gives a first detailed analysis of tolerable experimental imperfections of a quadrupole blade trap design from calculations and numerical simulations. In this work, it is found that the critical imperfections are electrical trans-phase shift and axially-asymmetric geometric misalignment. The second part of this thesis presents qudit-based quantum gates for trapped ions. A qudit encodes multiple quantum states within an elementary unit of quantum information. The denser encoding allows access to a larger Hilbert space, which enables more efficient quantum algorithms and use of quantum resource. However, in terms of practical realization of qudits, the additional complexities involved with manipulating multiple states within a single elementary unit may compromise fidelity of quantum operations. In this thesis, quantum gates generalized to qudits and the protocols to implement them on trapped $^{137}Ba^{+}$ ions are presented. Numerical simulations and calculations are performed to obtain the fidelity of each qudit gate to assess the practicality of realizing trapped ion qudit gates. From this work, it is found that single qudit gates can easily achieve better than 99.25% fidelity. The 3-level qudit entangling gate can achieve at least 99.10% fidelity.

Acknowledgements

My course through the Master's program in Physics has been rich and fruitful, which is only made possible by the wonderful people that I have met along this journey. First, I would like to thank my advisor, Crystal Senko. Trapped ion quantum computing was a new field of research to me when I first started my graduate program and Crystal has been very helpful in providing guidance throughout the course. Crystal is also open to new suggestions and discussion on the projects in the laboratory, which cultivates a creative work environment. Many thanks to Crystal for the opportunity to work on and build a trapped ion quantum computing system. I would also like to thank my advisory committee members Kazi Rajibul Islam and Michal Bajcsy for pointing out aspects that I should pay more attention to and their guidance during advisory committee meetings.

I took up some electrical and electronics projects for the laboratory. I was a novice in the field of electronics and I received many guidance from Richard Rademacher. I have learned a lot about electronics and even making custom printed circuit boards while working on these projects, and it is only possible thanks to Rich. I also had the pleasure of working closely with Brendan White and Matthew Day on our paper on practical realization of a qudit-based quantum computer and initial attempts to trap barium ions. Thanks also to Noah Greenberg who made the first helical resonator for our lab, which served as a fantastic reference for my project on the helical resonator.

I would also like to thank the many talented former and current undergraduate students in the team. Many thanks to Andrew Cox for his significant contribution on single qudit gate decomposition. The low photon counts from ion fluorescence was a mystery to us when we first trapped ions. It is thanks to Nigel Anderson that we solved the mystery by obtaining a more realistic photon scattering rate from his calculations. Ahmed Shalabi has worked diligently on computing a more realistic error due to motional heating of ions for our qudit entangling gate with wonderful results and I am grateful for that.

We have also collaborated and worked closely with Rajibul Islam's group. Nikhil Kotibhaskar and I worked closely on trap designs for both groups. I am also thankful to Gilbert (Chung-You) Shih for his guidance on Zemax simulations and various exchanges of ideas regarding optical setups. Many thanks also to Manas Sajjan, Roland Hablützel and Sainath Motlakunta for the collaborative effort in building up a trapped ion system.

I had the opportunity to learn machining skills and techniques for various tasks. Special thanks to Hiruy Haile, who is a wonderful machinist, for teaching me machining know-how.

Studying abroad far away must have been somewhat difficult for my family. Nevertheless, they are very supportive of my endeavour and I am very grateful for that. I would also

like to thank my uncle and aunt, Low John Seng and Low Huan Lang, for their support. Finally, I am forever grateful to my loving wife, Siong Chyi, who came with me for my studies, leaving her home and family half a globe away. Her continuous love and support have been instrumental to my progress.

Dedication

Dedicated to Siong Chyi.

Table of Contents

List of Tables

List of Figures

Chapter 1

Introduction

Quantum computing is a computational technique which exploits the quantum nature of certain systems to carry out logical computations. Due to the quantum nature that is not present in classical systems, quantum computation can theoretically solve certain problems much faster than classical computations would. For example, to factorize a large integer, classical computing would need sub-exponential time while Shors algorithm, utilizing quantum computing, can solve it in a much faster polynomial time [1]. Thus, research on the practical realization of quantum computing is a meaningful endeavor that can potentially bring about significant technological advancement.

A quantum bit (qubit) is an elementary unit of quantum information which encodes the bit signals of 0 and 1 with two respective quantum states. As opposed to a classical bit, where it has to be either 0 or 1, a qubit can be in a superposition of 0 and 1. In addition, they can form entangled states with other qubits that are unique to a quantum system. These properties allow clever algorithms to speed up some computation processes. The generalized version of a qubit is called a qudit, where d-level signals are encoded in d states, with d being any integer larger than 1. For example, a 5-level qudit would have 5 encoded quantum states representing the signals 0, 1, 2, 3 and 4. Encoding more quantum states within an elementary unit of quantum information is one way to scale up a quantum computer which is physically limited in terms of the number of elementary units. The Hilbert space dimension for N number of qubits scale with 2^N while d-level qudits scale with d^N. A 5-qubit system would have a dimension of $2^5 = 32$ while 5-level qudits would have a dimension of $5^5 = 3125$, which is 2 orders of magnitude larger than the qubit case. With the access to a larger Hilbert space, it has been shown that it is possible to implement more efficient algorithms, such as the reduction in quantum gate required for a Toffoli gate

[2, 3] and the reduced number of qudits required for quantum phase estimations with higher qudit dimensions [4].

A linear trapped ion system consists of a linear ion chain trapped in an oscillating electromagnetic field. Quantum information is encoded in the energy states of the ions, with selected energy states representing the computational states of 0, 1, and more for the case of qudits. Quantum entanglement between the ions is mediated by their shared vibrational phonon modes. A trapped ion system is one of the best candidates for practical quantum computation due to its long coherence time and the ability to perform high-fidelity quantum operations [5, 6, 7]. However, there is a limit to the number of ions that is possible to be trapped in a single linear Paul trap, with the current record being roughly ~ 100 in a single quadrupole blade trap to the best of my knowledge [8]. Thus, the problem of having limited physical resources is still a relevant problem in a trapped ion system as of the current state. Accessing unused energy levels in an ion for quantum computation (and thus making it a higher-dimensional qudit) is one way to increase the Hilbert space substantially given a limited number of ions.

There are many possible architectures for a linear Paul trap. Examples include four-rod traps [9, 10], quadrupole blade traps [7, 8, 11, 12], and micro-fabricated chip traps [13, 14, 15]. Among the aforementioned architectures, four-rod traps and blade traps are the ones which can be assembled manually. Although a blade trap geometry may offer advantages such as better control of electric field potential over a four-rod trap, there are more degrees of freedom associated with assembling a blade trap. With these additional complexities, it could be easier to have imperfections associated with the assembly. These imperfections can adversely affect a trapped ion experiment, particularly, they can introduce excess mircomotion which increases the Doppler cooling limit of an ion [9]. The micro-fabricated chip trap architecture allows the most control of electrical potential in the trap among the architectures discussed, but has much more limited optical access as compared to the quadrupole blade trap design. Thus, if large optical access is desired or is more convenient for certain experiments as compared to the benefits of having additional degrees of electric potential control, a quadrupole blade trap would generally be more preferable.

It is known from Ref. [9] that stray electric field and electrical trans-phase shift on the trap electrodes (which will be defined in Chapter 2 of this thesis) contribute to excess micromotion. There are other types of electrical imperfections that are not explicitly discussed in the literature, but may have been implied to not cause excess micromotion by omission. Nevertheless, this thesis provides an in-depth assessment of the effects of other electrical imperfections. Geometric misalignment of trap electrodes causes stray electric field. The stray electric field may be static or oscillating. For static stray field, the standard method for compensating excess micromotion is done by applying static biasing voltages.

The excess micromotion compensation for oscillating stray field and electrical trans-phase shift is more elaborate, which involves applying additional oscillating voltages to extra electrodes with matching frequencies with the trap electrode and properly tuned electrical phases and amplitudes [16]. Since this compensation scheme is much more difficult to implement as compared to applying static biasing voltages, we regard imperfections that require this more complex compensation scheme to be the critical ones. The extent of excess micromotion introduced due to certain electrical or geometrical imperfections are dependent on individual trap designs. Thus, the critical imperfections and their thresholds have to be analyzed and determined for individual trap designs. An example can be seen from Ref. [17], where numerical simulations and analysis are performed to determine the critical imperfections and thresholds of a layered linear Paul trap. In our work, we plan to build an adapted version of the five-segment quadrupole blade traps used in Ref. [8, 11]. Although this trap design has been shown to work well, the critical types of trap imperfections which lead to excess micromotion are not quantified. Those who intend to replicate or adapt the trap design without access to the same manufacturers for the trap components may have uncertainties with regards to the trap performance. Thus, it is valuable to quantify the extent of excess micromotion introduced for the imperfection in each degree of freedom and identify the ones that are tolerable and those that need to be properly addressed.

A complete quantum computing protocol includes quantum state preparation, state measurement, implementing single qudit (or qubit) gates and also entangling gates. Each of these quantum operations have some level of error as it is inevitable to have some error sources in a realistic experimental environment [15]. Fault-tolerance thresholds are the error thresholds where error correcting codes can be implemented to correct logical outputs to an arbitrary accuracy. To assess if a certain level of experimental error is acceptable, the fault-tolerance threshold is an appropriate benchmark. For a qubit system, the fault-tolerance threshold is reported to be 99.25% for a surface code [18]. For qudit systems, it is found that the fault-tolerance threshold would be more relaxed for higher qudit dimensions [19, 20]. However, to experimentally realize a trapped ion qudit system, there may be more errors due to the additional complexities involved with manipulating multiple energy states within a single ion. Thus, it is not immediately obvious that a qudit system would be more advantageous over a qubit system in terms of practical realization. To this date, some control of 3-level qudits have been realized experimentally [21, 22], but not to the extent of demonstrating a reliable and complete quantum computing scheme as has been done for qubits in Ref. [15]. There are several physical implementation of qudits with trapped ions that have been proposed [23, 24, 25, 26]. The proposals mostly focus on the feasibility of implementing qudit-based universal quantum computing and little analysis

on the expected (increase in) error for scaling up the qudit dimension is provided. In these proposals, qudit entangling gates are performed with generalized Cirac-Zoller schemes [27]. This scheme is known to be sensitive to the initial phonon states of the ions [5], which leads to difficulties in practical implementations. The Mølmer-Sørensen scheme is known to be much more robust against the initial phonon states [28], and has been shown to be capable of high-fidelity performance (error of 0.8×10^{-4}) [15]. Thus, the Mølmer-Sørensen scheme is generally preferred over the Cirac-Zoller scheme. In this thesis, a generalized Mølmer-Sørensen scheme for qudits is formulated for the first time. Furthermore, the practicality of qudit gates are also assessed by estimating the theoretically achievable fidelities after taking into account known error sources [15], which is an original effort to the best of my knowledge.

In the following chapters, two main studies are described. First, the investigations to quantify and determine the critical imperfections for a blade trap is described. Second, the estimated errors for single and two-qudit gates of 3 and 5-level qudits are investigated with numerical analysis. My work on building up an ion trap is also presented. Chapter 2 introduces the basic theory for a linear Paul trap and describes the calculations as well as numerical simulations performed to determine tolerable imperfections in a blade trap. Chapters 3 and 4 describe the experimental work in setting up voltage sources for a four-rod trap and the imaging system built to image the ions. Chapter 5 presents the single qudit gates and the estimated errors for a trapped $^{137}Ba^{+}$ ions. Chapter 6 describes the generalized version of the Mølmer-Sørensen gate for qudits and the estimated errors. Finally, Chapter 7 gives a conclusion on the two main studies presented.

Chapter 2

Estimation of Tolerable Imperfections in a Linear Paul Trap

2.1 Paul Trap Theory

In this chapter, my work on estimating tolerable imperfections for a quadrupole blade trap is presented. First, the theory for an idealized linear Paul trap is presented, which details the derivation for the motion of a trapped ion. Next, effects of electrical imperfections in a quadrupole trap are evaluated analytically via line-charge approximation. Finally, numerical simulations of an ion in an imperfect quadrupole blade trap are carried out. The motives of this are both to investigate and quantify the critical imperfections in our desired quadrupole blade trap and verify the analytical forms of the effects of electrical imperfections from line-charge approximation.

2.1.1 Ion Motion

A Paul ion trap utilizes the responsiveness of an ion to electrical forces to confine it to a fixed position. However, it is not possible to create an electrical potential minimum with static electric field for ion trapping from Earnshaw's theorem. The resolution to this is to have an oscillating electric field that effectively behaves like a potential sink to an ion. In an ideal linear Paul trap, 4 long hyperbolic electrodes are arranged as shown in Figure 2.1a for confinement in the transverse direction. 2 additional hyperbolic electrodes are used for axial confinement as shown in Figure 2.1b [29]. Oscillating voltages are applied to

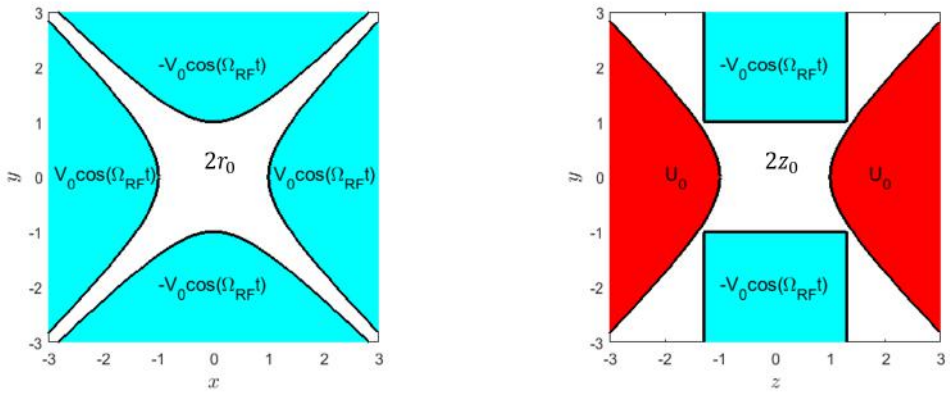

(a) (b)

Figure 2.1: Illustrations of hyperbolic electrodes for an ideal linear Paul trap. (a) Cross-section of the linear Paul trap, which is in the xy-plane. RF voltages are applied to the electrodes for transverse confinement. (b) Axial view of an ideal linear Paul trap, the yz-plane. DC voltages are applied to the endcap electrodes for axial confinement.

the 4 electrodes for transverse confinement. The frequency of these voltages are typically in the radiofrequency (RF) range for ion trapping purposes. The oscillating component shall be referred from hereon as the RF component in this thesis. Constant voltages are applied to the other 2 electrodes for axial confinement, which can also be referred to as endcap electrodes. This static component of the potential shall be referred to as the DC (direct current) component from hereon in this thesis. The ideal forms of the RF and DC components of the electrical potential are

$$\begin{aligned} V &= V_0 \frac{x^2 - y^2}{r_0^2} \cos\left(\Omega_{RF} t\right) \\ U &= U_0 \left(\frac{z^2}{z_0^2} - \frac{x^2 + y^2}{2 z_0^2} \right) \end{aligned} \tag{2.1}$$

where V is the RF component of the electrical potential, V_0 is the amplitude of the electrode potential, Ω_{RF} is the oscillation frequency of the RF potential, t is time, U is the DC component of the electrical potential, U_0 is the potential at the electrode, r_0 is the closest distance from the trap centre to a transversely confining electrode, z_0 is the distance from the trap centre to an axially confining electrode along the trap axis. x, y, and z are the coordinate from the centre of the trap.

The net potential experienced by is the summation of both the RF and DC components.

$$V_{net} = V + U = V_0 \frac{x^2 - y^2}{r_0^2} \cos(\Omega_{RF} t) + U_0 \left(\frac{z^2}{z_0^2} - \frac{x^2 + y^2}{2z_0^2} \right) \tag{2.2}$$

The acceleration experienced by an ion of charge Q and mass m in this field is $-\frac{Q}{m}\nabla V_{net}$. For the x-direction, the acceleration is

$$\frac{d^2x}{dt^2} = -\frac{Q}{m}\frac{dV_{net}}{dx} = -\frac{2QV_0 x}{mr_0^2} \cos(\Omega_{RF} t) + \frac{QU_0 x}{mz_0^2} \tag{2.3}$$

Defining $\tau = \frac{\Omega_{RF} t}{2}$, the left hand side (LHS) of Equation 2.3 becomes

$$\frac{d^2x}{dt^2} = \frac{d\tau}{dt}\frac{d}{dt}\left(\frac{dx}{dt}\right) = \left(\frac{d\tau}{dt}\right)^2 \left(\frac{d^2x}{d\tau^2}\right) \tag{2.4}$$

With $\frac{d\tau}{dt} = \frac{\Omega_{RF}}{2}$, Equation 2.3 can be rewritten as

$$\frac{d^2x}{d\tau^2} + [a - 2q\cos(2\tau)]x = 0 \tag{2.5}$$

where

$$a = -\frac{4QU_0}{\Omega_{RF}^2 m z_0^2}, \quad q = -\frac{4QV_0}{\Omega_{RF}^2 m r_0^2} \tag{2.6}$$

which is the form of Mathieu's differential equation.

From Equation 2.6, we can see that the a parameter is directly related to axial confinement, as it is directly proportional to the endcap-electrodes potential, U_0. For a linear Paul trap, a weak axial confinement relative to the transverse confinement is desired, so that ions would crystalize in a straight chain axially along the trap. Thus, the a parameter is typically small for a linear Paul trap. We shall see later in Section 2.1.2 that in the regime of small a, a small q parameter is required to trap an ion. Before going through the thorough mathematical derivations, the intuitive physical understanding of how an ion is trapped in a linear Paul trap in the regime of small a is as follows. The trapping region of the oscillating voltage in the transverse plane can be visualized as a saddle point with a flipping surface potential. At any given point in time, an ion is confined from one direction and is anti-confined for the direction perpendicular to it. Before the ion can be accelerated out of the trap along the anti-confining direction, the potential is flipped, pushing the ion back to the saddle point. Thus, it can be understood intuitively that the oscillating frequency, Ω_{RF}, needs to be large, which corresponds to a lower q parameter. It can also

be intuitively understood that a large oscillating voltage, V_0, has to be compensated with large Ω_{RF} too as an ion is being accelerated faster out of the saddle point at a given point in time. The potential has to be flipped faster to prevent the ion from leaving the trapping region.

The following derivations to obtain a solution to Mathieu's equation is adapted from and based on Ref. [10, 30]. Since Equation 2.5 is a second order differential equation, it has 2 linearly independent solutions. Let $x_1(\tau)$ and $x_2(\tau)$ be the 2 linearly independent solutions. Evaluating a solution translated in the dimensionless time by π, $\tau' = \tau + \pi$, gives

$$\frac{d^2}{d\tau^2}x(\tau+\pi) + [a - 2q\cos(2\tau)]x(\tau+\pi) = \frac{d^2}{d\tau'^2}x(\tau') + [a - 2q\cos(2\tau')]x(\tau') = 0 \tag{2.7}$$

which implies that $x(\tau+\pi)$ is also a solution to the Mathieu equation if $x(\tau)$ is a solution. Thus, we can express $x_1(\tau+\pi)$ and $x_2(\tau+\pi)$ as a linear combination of $x_1(\tau)$ and $x_2(\tau)$.

$$\begin{aligned} x_1(\tau+\pi) &= T_{11}x_1(\tau) + T_{21}x_2(\tau) \\ x_2(\tau+\pi) &= T_{12}x_1(\tau) + T_{22}x_2(\tau) \end{aligned} \tag{2.8}$$

From Equation 2.8, a time evolution operator that translates in the dimensionless time by π can be constructed

$$\hat{T}_\pi = \begin{pmatrix} T_{11} & T_{12} \\ T_{21} & T_{22} \end{pmatrix} \tag{2.9}$$

Since a time evolution operator is unitary, it is diagonalizable. Without loss of generality, we choose $x_1(\tau)$ and $x_2(\tau)$ such that $\hat{T}_\pi$ is in a diagonal form. This implies

$$\begin{aligned} \hat{T}_\pi x_1(\tau) &= x_1(\tau+\pi) = T_{11}x_1(\tau) \\ \hat{T}_\pi x_2(\tau) &= x_2(\tau+\pi) = T_{22}x_2(\tau) \end{aligned} \tag{2.10}$$

We can rewrite T_{11} and T_{22} as

$$\begin{aligned} T_{11} &= e^{(\alpha_1+i\nu_1)\pi} \\ T_{22} &= e^{(\alpha_2+i\nu_2)\pi} \end{aligned} \tag{2.11}$$

We note that

$$\hat{T}_\pi^n x(\tau) = x(\tau+n\pi) = e^{(\alpha+i\nu)n\pi}x(\tau) \tag{2.12}$$

To satisfy $\frac{x(\tau+n\pi)}{x(\tau)} = e^{(\alpha+i\nu)n\pi}$, an obvious solution is

$$x(\tau) = e^{(\alpha+i\nu)\tau}f(\tau) \tag{2.13}$$

where $f(\tau)$ is a function periodic with π, $f(\tau+\pi) = f(\tau)$. From the properties of a unitary operator,

$$\det(\hat{T}) = 1 \tag{2.14}$$

and thus

$$T_{22} = e^{(\alpha_2+i\nu_2)\pi} = e^{-(\alpha_1+i\nu_1)\pi} \tag{2.15}$$

Rewriting $\alpha = \alpha_1$ and $\nu = \nu_1$, the following is obtained

$$\begin{aligned} x_1(\tau) &= e^{(\alpha+i\nu)\tau} f_1(\tau) \\ x_2(\tau) &= e^{-(\alpha+i\nu)\tau} f_2(\tau) \end{aligned} \tag{2.16}$$

Note that x_1 or x_2 alone is not a purely real function for a general ν, which is not physical in describing the motion of an ion. The motion of ion is described by a linear combination of x_1 and x_2. From Equation 2.16, either x_1 or x_2 will increase indefinitely with τ for non-zero α. Physically, it means that an ion would not be trapped for non-zero α. Since $f_1(\tau)$ is periodic with π, we can write it as a Fourier series

$$\begin{aligned} f_1(\tau) &= \sum_{k=-\infty}^{\infty} c_k e^{i2k\tau} \\ f_2(\tau) &= \sum_{k=-\infty}^{\infty} d_k e^{i2k\tau} \end{aligned} \tag{2.17}$$

For $\alpha = 0$, we have

$$\begin{aligned} x_1(\tau) &= \sum_{k=-\infty}^{\infty} c_k e^{i(2k+\nu)\tau} \\ x_2(\tau) &= \sum_{k=-\infty}^{\infty} d_k e^{i(2k-\nu)\tau} \end{aligned} \tag{2.18}$$

From Equation 2.18, it can be observed that ν from 0 to 1 spans all possibilities. Plugging x_1 in Equation 2.18 into Equation 2.5 gives

$$\begin{aligned} &\frac{d^2}{d\tau^2}\left[\sum_{k=-\infty}^{\infty} c_k e^{i(2k+\nu)\tau}\right] + [a - 2q\cos(2\tau)] \sum_{k=-\infty}^{\infty} c_k e^{i(2k+\nu)\tau} \\ &= -\sum_{k=-\infty}^{\infty} c_k (2k+\nu)^2 e^{i(2k+\nu)\tau} + [a - q(e^{i2\tau} + e^{-i2\tau})] \sum_{k=-\infty}^{\infty} c_k e^{i(2k+\nu)\tau} = 0 \end{aligned} \tag{2.19}$$

For the LHS of Equation 2.19 to be zero for all values of τ, the terms with the same exponents have to add up to zero, i.e.

$$-c_k(2k+\nu)^2 + ac_k - qc_{k+1} - qc_{k-1} = 0 \tag{2.20}$$

If a solution for Equation 2.20 exists with a real valued ν, its physical significance is that the motion of an ion is bounded - it is trapped. The values of a and q where such solutions exist are called the stability region. A numerical method of finding the stability region is elaborated in Section 2.1.2.

Defining

$$D_k = \frac{a-(2k+\nu)^2}{q} \tag{2.21}$$

Equation 2.20 can be rewritten as the following 2 forms

$$\frac{c_k}{c_{k-1}} = \frac{1}{D_k - \frac{c_{k+1}}{c_k}} \tag{2.22}$$

$$\frac{c_k}{c_{k+1}} = \frac{1}{D_k - \frac{c_{k-1}}{c_k}} \tag{2.23}$$

Note that Equations 2.22 and 2.23 forms a recurrence relation

$$\frac{c_k}{c_{k-1}} = \frac{1}{D_k - \frac{1}{D_{k+1} - \ldots}} \tag{2.24}$$

$$\frac{c_k}{c_{k+1}} = \frac{1}{D_k - \frac{1}{D_{k-1} - \ldots}} \tag{2.25}$$

Since D_k increases quadratically with magnitude of k, Equation 2.24 indicates that c_k converges to zero for large $|k|$, where $k > 0$. Likewise, c_k for $k < 0$ converges to zero for large $|k|$ from Equation 2.25. Making a first order approximation, c_k is set to 0 for $|k| \geq 2$. Equation 2.20 for $k = 0$ can then be rewritten as

$$D_0 - \frac{1}{D_1} - \frac{1}{D_{-1}} = 0 \tag{2.26}$$

For the case where $|a|$ is small and $\nu \ll 2$, we obtain

$$\begin{aligned} D_0 - \frac{1}{D_1} - \frac{1}{D_{-1}} &= \frac{a-\nu^2}{q} - \frac{q}{a-(2+\nu)^2} - \frac{q}{a-(-2+\nu)^2} \\ &\approx \frac{a-\nu^2}{q} - \frac{q}{2} \end{aligned} \tag{2.27}$$

ν can then be obtained to be

$$\nu = \sqrt{a + \frac{q^2}{2}} \tag{2.28}$$

It will be shown in Section 2.1.2 that $q < 1$ when $|a|$ is small. Thus, the assumption that $\nu \ll 2$ generally holds.

As elucidated earlier,he motion of ion is described by a linear combination of x_1 and x_2.

$$x_m(\tau) = K_1 x_1(\tau) + K_2 x_2(\tau) = K_1 \sum_{k=-\infty}^{\infty} c_k e^{i(2k+\nu)\tau} + K_2 \sum_{k=-\infty}^{\infty} d_k e^{i(2k-\nu)\tau} \tag{2.29}$$

For x_m to be real,

$$K_1 c_k = K_2^* d_{-k}^* \tag{2.30}$$

Writing K_1 in the form $K_1 = |K_1|e^{i\theta}$ and let c_0 be real without loss of generality, the equation of motion can then be written as

$$x_m(\tau) = |K_1| \sum_{k=0}^{\infty} 2c_k \cos\left((2k+\nu)\tau + \theta\right) \tag{2.31}$$

Making the aforementioned first order approximation where $c_k = 0$ for $|k| \geq 2$, and for the case where a is small and $\nu_1 \ll 2$,

$$x_m(\tau) \approx 2|K_1|c_0 \left(\cos\left(\nu\tau + \theta\right) + \frac{q}{2}\cos\left(2\tau\right)\cos\left(\nu\tau + \theta\right)\right) \tag{2.32}$$

Converting back to an expression in terms of t and defining $\omega_s = \frac{\nu\Omega_{RF}}{2}$ gives

$$\begin{aligned} x_m(t) &\approx 2|K_1|c_0 \left(\cos\left(\frac{\nu\Omega_{RF}}{2}t + \theta\right) + \frac{q}{2}\cos\left(\Omega_{RF}t\right)\cos\left(\frac{\nu\Omega_{RF}}{2}t + \theta\right)\right) \\ &= 2|K_1|c_0 \left(\cos\left(\omega_s t + \theta\right) + \frac{q}{2}\cos\left(\Omega_{RF}t\right)\cos\left(\omega_s t + \theta\right)\right) \end{aligned} \tag{2.33}$$

From Equation 2.33, it can be seen that the ion mainly oscillates at frequency ω_s. This component of the motion is commonly known as the secular motion, and ω_s is the secular frequency. The q parameter is typically small for an ion trap experiment, as we desire the ion motion to be close to a simple harmonic oscillator. From the second term in Equation 2.33, there is also a small amplitude oscillation (due to small q) at frequency Ω_{RF}, beating with the frequency ω_s. This high frequency oscillation is known as a micromotion. The

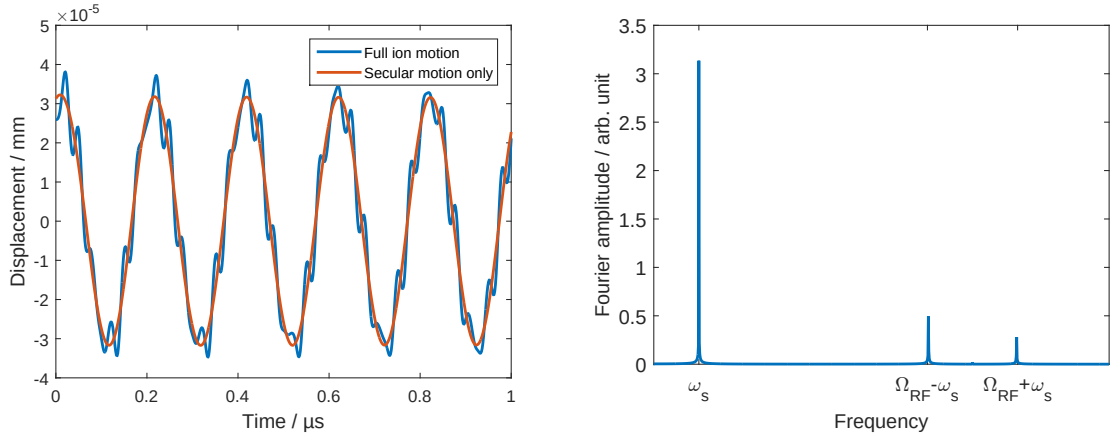

(a) (b)

Figure 2.2: Ion motion simulated with SIMION (see Section 2.5). (a) Displacement of ion with time. The blue curve is the full motion which satisfies Mathieu's equation. The red curve is the secular motion of the ion. (b) Fourier transform of the full ion motion.

ion motion and its Fourier components are shown in Figure 2.2. From the solution to Mathieu's equation, we also see that the existence of micromotion is inevitable in a Paul ion trap system. Thus, we further specify this as intrinsic micromotion. We shall see in Section 2.2 that there is another type of micromotion stemming from imperfections in an ion trap, which is called excess micromotion.

From Equation 2.28, we see that for the case where a and q are small, the secular motion frequency can be approximated to be

$$\omega_s \approx \frac{\Omega_{RF}}{2}\sqrt{a+\frac{q^2}{2}} \tag{2.34}$$

For the motion in y-direction, computing the equation of motion from the electrical potential in Equation 2.2 gives

$$\frac{d^2y}{dt^2} = -\frac{Q}{m}\frac{dV_{net}}{dy} = \frac{2QV_0x}{mr_0^2}\cos\left(\Omega_{RF}t\right) + \frac{QU_0x}{mz_0^2} \tag{2.35}$$

which only results in a flip in sign of the q parameter in the Mathieu's equation. Evaluating the solution similar to the procedure for x-motion, the resultant form of y motion is approximately

$$y_m(t) \approx 2|K_y|c_0\left(\cos\left(\omega_s t+\theta\right) - \frac{q}{2}\cos\left(\Omega_{RF}t\right)\cos\left(\omega_s t+\theta\right)\right) \tag{2.36}$$

Similar to the x-motion, it also has secular and micromotion components.

For motion in z-direction, the equation of motion derived from Equation 2.2 is

$$\frac{d^2z}{dt^2} = -\frac{2QU_0}{mz_0^2}z \tag{2.37}$$

which is just a simple harmonic motion. The solution for the z-motion is

$$z = |K_z| \cos(\omega_z t + \theta_z) \tag{2.38}$$

where the axial motional frequency is

$$\omega_z = \sqrt{\frac{2QU_0}{mz_0^2}} \tag{2.39}$$

2.1.2 Mathieu's Equation Stability Region

As discussed in the previous section, an ion is only trapped when there is a solution to Equation 2.20 with real valued ν. Whether a solution exists depends on the values of a and q parameters. The range of a and q parameters where such a solution exists is called the stability region. Following Ref. [31], the stability region can be obtained numerically. Equation 2.20 can be written in a matrix form as

$$\mathbf{H}_\nu \mathbf{c} = \mathbf{0} \tag{2.40}$$

where

$$\mathbf{H}_\nu = \begin{pmatrix} \cdots & \cdots & \cdots & \cdots & \cdots & \cdots & \cdots \\ \vdots & (-4+\nu)^2 - a & q & 0 & 0 & 0 & \vdots \\ \vdots & q & (-2+\nu)^2 - a & q & 0 & 0 & \vdots \\ \vdots & 0 & q & \nu^2 - a & q & 0 & \vdots \\ \vdots & 0 & 0 & q & (2+\nu)^2 - a & q & \vdots \\ \vdots & 0 & 0 & 0 & q & (4+\nu)^2 - a & \vdots \\ \cdots & \cdots & \cdots & \cdots & \cdots & \cdots & \cdots \end{pmatrix},$$

$$\mathbf{c} = \begin{pmatrix} \vdots \\ c_{-1} \\ c_0 \\ c_1 \\ \vdots \end{pmatrix} \tag{2.41}$$

For Equation 2.40 to have a non-trivial solution, $\det(\mathbf{H}_\nu) = 0$. Thus, for a certain value of ν, one can scan the values of a and q and evaluate $\det(\mathbf{H}_\nu)$ numerically. The set of parameters that results in $\det(\mathbf{H}_\nu) = 0$ are within the stability region. This can be repeated for other values of ν_1 spanning from 0 to 1 to obtain the complete stability region. Note that $\mathbf{H}_\nu$ and $\mathbf{c}$ are theoretically infinite in size, and it is computationally impossible to evaluate an infinitely large matrix. However, since we have shown that c_k converges to zero for large $|k|$, an accurate enough approximation can be obtained as long as the matrix is truncated at a large enough threshold $|k_{threshold}|$ value. Figure 2.3a shows the stability region of Mathieu's equation generated with the described numerical method with $|k_{threshold}| = 10$. When designing an ion trap it is important to choose the trap parameters such that the a and q parameters fall within the stability region. From Section 2.1.1, the q parameter for the y-motion is the negative value of the q parameter for the x-motion. From Figure 2.3a, the stability region is symmetric for the transformation $q \to -q$. Thus, x and y-motion share the same stability region. For axial confinement, the endcap electrode potentials have to positive valued for positively charged ions. This implies $a < 0$. Therefore, q should be chosen accordingly in the negative a area of the stability region to trap an ion.

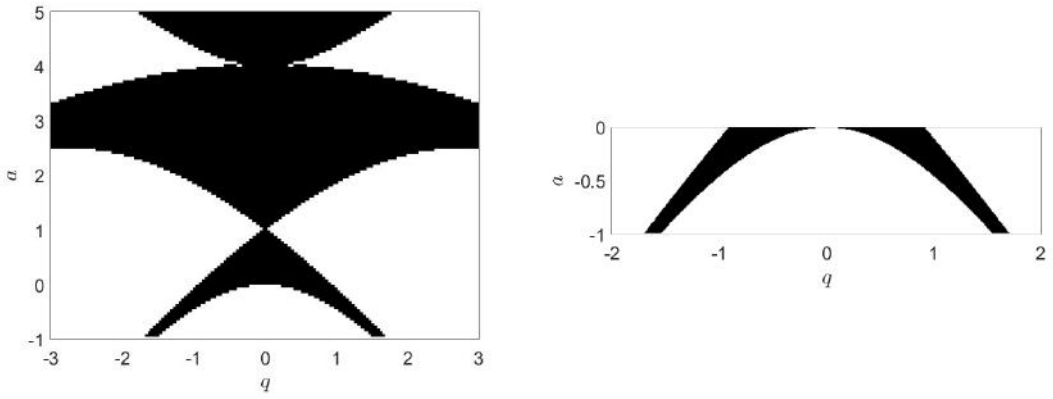

(a) (b)

Figure 2.3: (a) Stability region (black) of Mathieu's equation obtained numerically. (b) Relevant stability region for our trap.

2.2 Excess Micromotion

As stated in Section 2.1.1, there is another type of micromotion in addition to intrinsic micromotion which arises from experimental imperfections. A simple example is when there is a static electric field displacing an ion in the transverse direction with respect to the trap axis from the point with zero force from the RF potential (at $x = 0$ and $y = 0$), which will be referred to from hereon as the RF null.

Let there be a static electrical potential linear in the x-direction

$$V_{offset} = \xi x \tag{2.42}$$

where ξ is the electric field. This modifies the electrical potential in an ion trap to

$$V_{net} = V_0 \frac{x^2 - y^2}{r_0^2} \cos(\Omega_{RF} t) + U_0 \left(\frac{z^2}{z_0^2} - \frac{x^2 + y^2}{2z_0^2} \right) + \xi x \tag{2.43}$$

Evaluating the equation of motion in the x-direction gives

$$\frac{d^2x}{dt^2} = -\frac{2QV_0 x}{mr_0^2} \cos(\Omega_{RF} t) + \frac{QU_0 x}{mz_0^2} - \frac{Q\xi}{m} \tag{2.44}$$

Expressing the equation of motion in terms of τ, a and q, we obtain

$$\frac{d^2x}{d\tau^2} + [a - 2q\cos(2\tau)]x = -\frac{4Q\xi}{m\Omega_{RF}^2} \tag{2.45}$$

which transforms Mathieu's equation to an inhomogeneous second order differential equation. Thus, the general solution is of the form

$$x(\tau) = K_1 x_1(\tau) + K_2 x_2(\tau) + X(\tau) \tag{2.46}$$

where $x_1(\tau)$ and $x_2(\tau)$ are linearly independent solutions to the Mathieu equation, X is the specific solution to the inhomogeneous form. We make a smart guess and try

$$X(\tau) = \sum_{k=-\infty}^{\infty} c_k e^{i2k\tau} \tag{2.47}$$

Plugging $X(\tau)$ into Equation 2.45 gives

$$\begin{aligned} ac_0 - qc_1 - qc_{-1} &= -\frac{4Q\xi}{m\Omega_{RF}^2}, \quad k = 0 \\ -c_k(2k)^2 + ac_k - qc_{k+1} - qc_{k-1} &= 0, \quad k \neq 0 \end{aligned} \tag{2.48}$$

Making a first order approximation where $c_k = 0$ for $|k| \geq 2$, solving for c_0 and c_1 gives

$$c_0 = \frac{4Q\xi(4-a)}{(a(a-4)-2q^2)m\Omega_{RF}^2} \tag{2.49}$$

$$c_1 = \frac{4Q\xi q}{(a(4-a)+2q^2)m\Omega_{RF}^2} \tag{2.50}$$

This indicates that the equilibrium position of the ion is displaced by a distance of $c_0 = \frac{4Q\xi(4-a)}{(a(a-4)-2q^2)m\Omega_{RF}^2}$ and it introduces an excess micromotion oscillating at frequency Ω_{RF} with a fixed amplitude of $\frac{8Q\xi q}{(a(4-a)+2q^2)m\Omega_{RF}^2}$. It is important to keep excess micromotion low as it limits the Doppler cooling limit of an ion [9]. Figure 2.4 shows the Fourier components of an ion motion with excess micromotion.

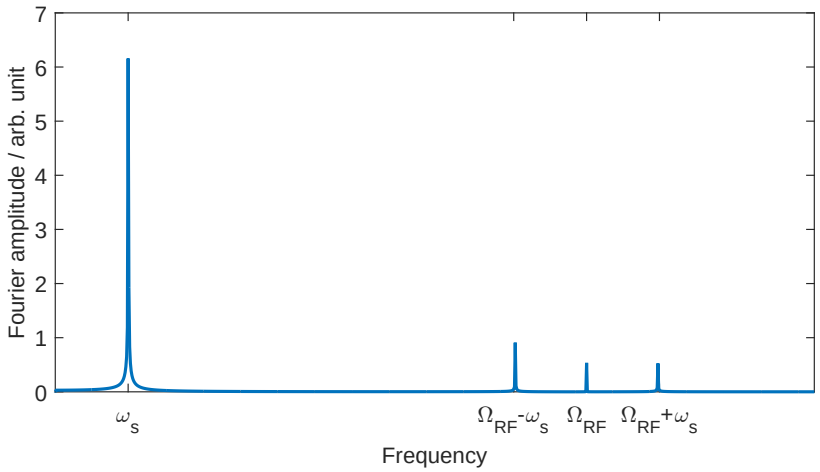

Figure 2.4: Fourier components of an ion motion with excess micromotion.

There are other sources of excess micromotion, which will be further explored in Sections 2.3 and 2.5.

2.3 Line Charge Approximation

To study the behaviour of the motion of an ion in an ion trap, it is useful to model the electrodes for transverse confinement with lines of charges. This section gives detailed

derivations for different experimental imperfections with line charge approximation for readers who are potentially interested to follow them. Readers who are not interested in the nitty-gritty derivations can skip to the last paragraphs of each subsection for the implication of an experimental imperfection.

2.3.1 Initial Derivation

In this section, I show that electrode configurations that electrode configurations that can be approximated with 4 line charges can generate the desired RF potential as shown in Equation 2.1, up to some geometrical factor. With 4 line-charge electrodes, the potential at the ion position (x, y, z) due to one of the 4 electrodes is

$$\begin{aligned} V &= \int_{-z_0-z}^{z_0-z} \frac{C}{4\pi\epsilon_0\sqrt{r^2+z^2}} \\ &= \frac{C}{4\pi\epsilon_0} \ln\left(\frac{\sqrt{(z_0-z)^2+r^2}+z_0-z}{\sqrt{(z_0-z)^2+r^2}-z_0-z}\right) \end{aligned} \tag{2.51}$$

where C is the line charge density, $r = \sqrt{x^2+y^2}$, ϵ_0 is the electrical permittivity in free space and $2z_0$ is the length of a line charge. Arranging the electrodes as shown in Figure 2.5, the radial distances of an ion to each rod are

$$\begin{aligned} r_1^2 &= x^2 + (R_0 - y)^2 \\ r_2^2 &= (R_0 - x)^2 + y^2 \\ r_3^2 &= x^2 + (R_0 + y)^2 \\ r_4^2 &= (R_0 + x)^2 + y^2 \end{aligned} \tag{2.52}$$

where R_0 is defined as the radial distance from the centre of the trap to a line charge, in order to distinguish it from r_0 as defined in Section 2.1, which is the closest radial distance to an electrode surface. For a linear Paul trap, the RF confining electrodes are typically long to minimize RF component in the axial direction. Thus, $z_0 \gg R_0$. We also assume that the trapped ion is cold. Thus, $x \ll R_0$, $y \ll R_0$ and $z \ll R_0$. With $|z| \ll |z_0|$, we can approximate the potential as

$$V \approx \frac{C}{4\pi\epsilon_0} \ln\left(\frac{\sqrt{z_0^2+r^2}+z_0}{\sqrt{z_0^2+r^2}-z_0}\right) \tag{2.53}$$

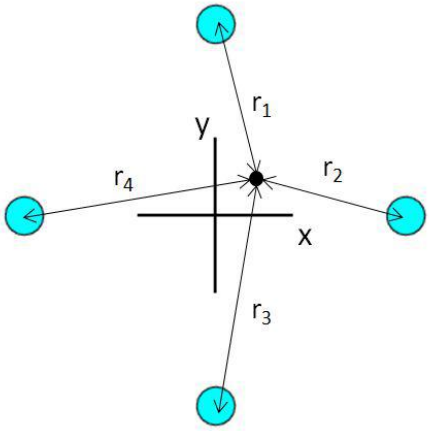

Figure 2.5: Sketch of an ion in a cross-section of a linear Paul trap with sets of line charges approximating the electrodes. The black dot represents an ion. Cyan circles represent the line charge electrodes. r_i is the radial distance to the i^{th} electrode.

With time-varying line charge density of $C = +C_0 \cos(\Omega t)$ at electrodes 2 and 4, and $C = -C_0 \cos(\Omega t)$ at electrodes 1 and 3, the potential at the ion is then

$$V \approx \frac{C_0}{4\pi\epsilon_0} \cos(\Omega t) \sum_{l=1}^{4} (-1)^l \ln\left(\frac{\sqrt{z_0^2 + r_l^2} + z_0}{\sqrt{z_0^2 + r_l^2} - z_0}\right) \tag{2.54}$$

With the condition $r_l^2 \ll z_0^2$, the logarithmic term can be simplified to

$$\begin{aligned} \ln\left(\frac{\sqrt{z_0^2 + r_l^2} + z_0}{\sqrt{z_0^2 + r_l^2} - z_0}\right) &= \ln z_0 + \ln\left(1 + \sqrt{1 + \frac{r_l^2}{z_0^2}}\right) - \ln\left(z_0\left(\sqrt{1 + \frac{r_l^2}{z_0^2}} - 1\right)\right) \\ &\approx A + \ln\left(1 + \frac{r_l^2}{4z_0^2}\right) - \ln r_l^2 \end{aligned} \tag{2.55}$$

where $A = \ln z_0 + \ln 2 + \ln 2z_0$. Thus,

$$\begin{aligned} \sum_{l=1}^{4} (-1)^l \ln\left(\frac{\sqrt{z_0^2 + r_l^2} + z_0}{\sqrt{z_0^2 + r_l^2} - z_0}\right) &\approx \sum_{l=1}^{4} (-1)^l \left[\ln\left(1 + \frac{r_l^2}{4z_0^2}\right) - \ln r_l^2\right] \\ &= \ln(r_1^2 r_3^2) - \ln(r_2^2 r_4^2) + \sum_{l=1}^{4} (-1)^l \ln\left(1 + \frac{r_l^2}{4z_0^2}\right) \end{aligned} \tag{2.56}$$

From Equations 2.52, the first two terms in Equation 2.56 can be rewritten as

$$\begin{aligned}\ln\left(r_1^2 r_3^2\right) - \ln\left(r_2^2 r_4^2\right) = &\ln\left(1 + \frac{x^4 + y^4 + 2x^2y^2 + 2R_0^2x^2 - 2R_0y^2}{R_0^4}\right) \\ &- \ln\left(1 + \frac{x^4 + y^4 + 2x^2y^2 - 2R_0^2x^2 + 2R_0y^2}{R_0^4}\right)\end{aligned} \tag{2.57}$$

Since $|x|, |y| \ll R_0$, the logarithmic terms can be approximated with Taylor expansion. Preserving only the terms up to the second order, i.e. the terms $\frac{x^m y^n}{R_0^{m+n}}$ where $m + n \leq 2$, we obtain

$$\begin{aligned}&\ln\left(1 + \frac{x^4 + y^4 + 2x^2y^2 + 2R_0^2x^2 - 2R_0y^2}{R_0^4}\right) - \ln\left(1 + \frac{x^4 + y^4 + 2x^2y^2 - 2R_0^2x^2 + 2R_0y^2}{R_0^4}\right) \\ &\approx 4\frac{x^2 - y^2}{R_0^2}\end{aligned} \tag{2.58}$$

For the remaining terms in Equation 2.56, expanding them in Taylor series gives

$$\sum_{l=1}^{4}(-1)^l \ln\left(1 + \frac{r_l^2}{4z_0^2}\right) = \sum_{l=1}^{4}(-1)^l \left[\frac{r_l^2}{4z_0^2} - \frac{r_l^4}{32z_0^4} + O\left(\frac{r_l^6}{z_0^6}\right)\right] \tag{2.59}$$

Including up to the terms $x^m y^n$ where $m + n \leq 2$, we obtain

$$\begin{aligned}&\sum_{l=1}^{4}(-1)^l \left[\frac{r_l^2}{4z_0^2} - \frac{r_l^4}{32z_0^4} + O\left(\frac{r_l^6}{z_0^6}\right)\right] \\ &\approx \frac{R_0y^2 - R_0x^2}{8z_0^4}\end{aligned} \tag{2.60}$$

Thus, Equation 2.56 can be simplified to

$$\sum_{l=1}^{4}(-1)^l \ln\left(\frac{\sqrt{z_0^2 + r_l^2} + z_0}{\sqrt{z_0^2 + r_l^2} - z_0}\right) \approx 4\frac{x^2 - y^2}{R_0^2} + \frac{R_0^2y^2 - R_0^2x^2}{8z_0^4} \tag{2.61}$$

Since $\frac{R_0^2}{z_0^4} \ll \frac{1}{R_0^2}$, we can simplify it further to

$$\sum_{l=1}^{4}(-1)^l \ln\left(\frac{\sqrt{z_0^2 + r_l^2} + z_0}{\sqrt{z_0^2 + r_l^2} - z_0}\right) \approx 4\frac{x^2 - y^2}{R_0^2} \tag{2.62}$$

Finally, we arrive the the potential due to the four electrodes

$$V = \frac{C_0}{\pi\epsilon_0}\frac{x^2 - y^2}{R_0^2}\cos\left(\Omega_{RF}t\right) \tag{2.63}$$

By defining $\kappa_{RF}V_0 = \frac{C_0 R_0^2}{\pi\epsilon_0 r_0^2}$, where κ_{RF} is the RF geometrical factor that is dependent on trap geometry, we arrive at the same form as the RF Paul trap potential in Equation 2.1. This method of deriving the Paul trap potential is useful for computing the effect of imperfections in our trap, as shown in the following sections.

2.3.2 Cis-phase shift

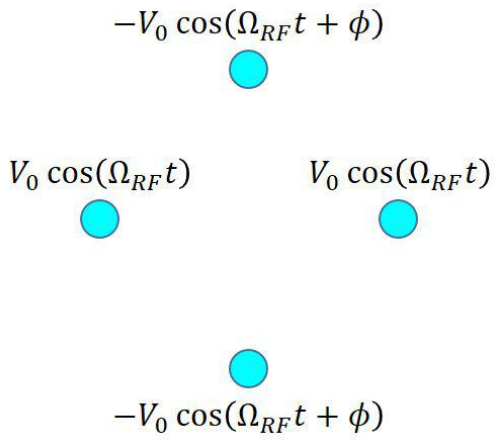

Figure 2.6: Illustration of cis-phase shift applied to line charge electrodes 1 and 3.

Cis-phase shift is defined in this thesis as the case where an opposing pair of electrodes has a phase shift in its RF potential as compared to the other pair. An illustration is shown in Figure 2.6. To predict the effect of a cis-phase shift on the overall potential, the line charge approximation method can be used. The charge densities in the electrodes are modelled to be time varying as follows

$$\begin{aligned} C_1(t) &= -C_0\cos\left(\Omega_{RF}t + \phi\right) \\ C_2(t) &= C_0\cos\left(\Omega_{RF}t\right) \\ C_3(t) &= -C_0\cos\left(\Omega_{RF}t + \phi\right) \\ C_4(t) &= C_0\cos\left(\Omega_{RF}t\right) \end{aligned} \tag{2.64}$$

Summing the potential from all four electrodes gives

$$
\begin{aligned}
V &= \sum_{l=1}^{4} V_l \\
&= \frac{V_0}{4}\left[\cos\left(\Omega_{RF}t\right)\left(\ln\left(\frac{\sqrt{(z_0-z)^2+r_2^2}+z_0-z}{\sqrt{(z_0-z)^2+r_2^2}-z_0-z}\right)+\ln\left(\frac{\sqrt{(z_0-z)^2+r_4^2}+z_0-z}{\sqrt{(z_0-z)^2+r_4^2}-z_0-z}\right)\right)\right. \\
&\left. -\cos\left(\Omega_{RF}t+\phi\right)\left(\ln\left(\frac{\sqrt{(z_0-z)^2+r_1^2}+z_0-z}{\sqrt{(z_0-z)^2+r_1^2}-z_0-z}\right)+\ln\left(\frac{\sqrt{(z_0-z)^2+r_3^2}+z_0-z}{\sqrt{(z_0-z)^2+r_3^2}-z_0-z}\right)\right)\right]
\end{aligned}
\tag{2.65}
$$

Making the same approximations as Section 2.3.1, the following is derived

$$
\begin{aligned}
V &\approx \frac{V_0}{4}\left[\cos\left(\Omega_{RF}t\right)\left(2A+\ln\left(1+\frac{r_2^2}{4z_0^2}\right)-\ln\left(r_2^2\right)+\ln\left(1+\frac{r_4^2}{4z_0^2}\right)-\ln\left(r_4^2\right)\right)\right. \\
&\left. -\cos\left(\Omega_{RF}t+\phi\right)\left(2A+\ln\left(1+\frac{r_1^2}{4z_0^2}\right)-\ln\left(r_1^2\right)+\ln\left(1+\frac{r_3^2}{4z_0^2}\right)-\ln\left(r_3^2\right)\right)\right] \\
&\approx \frac{V_0}{4}\left[\cos\left(\Omega_{RF}t\right)\left(A_1+\frac{r_2^2+r_4^2}{4z_0^2}-\frac{-x^2-2R_0x+y^2}{R_0^2}-\frac{-x^2+2R_0x+y^2}{R_0^2}\right)\right. \\
&\left. -\cos\left(\Omega_{RF}t+\phi\right)\left(A_1+\frac{r_1^2+r_3^2}{4z_0^2}-\frac{x^2-2R_0y-y^2}{R_0^2}-\frac{x^2+2R_0y-y^2}{R_0^2}\right)\right] \\
&= \frac{V_0}{4}\left[\cos\left(\Omega_{RF}t\right)\left(A_1+\frac{x^2+y^2+R_0^2}{2z_0^2}+2\frac{x^2-y^2}{R_0^2}\right)\right. \\
&\left. -\cos\left(\Omega_{RF}t+\phi\right)\left(A_1+\frac{x^2+y^2+R_0^2}{2z_0^2}-2\frac{x^2-y^2}{R_0^2}\right)\right] \\
&= \frac{V_0}{4}\left[2\frac{x^2-y^2}{R_0^2}[\cos\left(\Omega_{RF}t\right)+\cos\left(\Omega_{RF}t+\phi\right)]\right. \\
&\left. +\frac{x^2+y^2}{2z_0^2}[\cos\left(\Omega_{RF}t\right)-\cos\left(\Omega_{RF}t+\phi\right)]+A_2\right] \\
&= V_0\frac{x^2-y^2}{R_0^2}\cos\left(\frac{\phi}{2}\right)\cos\left(\Omega_{RF}t\right)+V_0\frac{x^2+y^2}{4z_0^2}\sin\left(\frac{\phi}{2}\right)\sin\left(\Omega_{RF}t\right)+A_3
\end{aligned}
\tag{2.66}
$$

where A_n are terms independent of ion position. $A_1 = 2A + \ln\left(R_0^2\right)$,
$A_2 = 2\left(A_1 + \frac{R_0^2}{2z_0^2}\right)\sin\left(\frac{\phi}{2}\right)\sin\left(\Omega_{RF}t\right)$, $A_3 = \frac{V_0}{4}A_2$.

Since $R_0^2 \ll z_0^2$, the sine term can be ignored and the following is obtained

$$V \approx V_0 \frac{x^2 - y^2}{R_0^2} \cos\left(\frac{\phi}{2}\right) \cos\left(\Omega_{RF} t\right) + A_3 \tag{2.67}$$

From the derived form, having cis-phase shift only weakens the trapping potential compared to the case without by a factor of $\cos\left(\frac{\phi}{2}\right)$, and does not introduce any excess micromotion.

2.3.3 Trans-phase shift

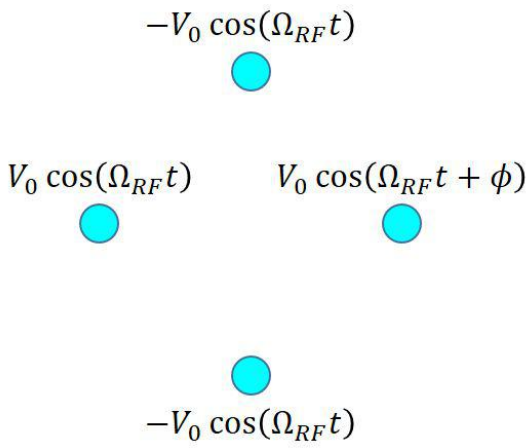

Figure 2.7: Illustration of trans-phase shift applied to line charge electrode 2.

In this thesis, trans-phase shift is defined as the case where an electrode opposite to another electrode has a phase shift of ϕ, as shown in Figure 2.7.

Without loss of generality, electrode 2 is chosen as the electrode with a phase shift of

ϕ. Evaluating the potential from all four electrodes gives

$$
\begin{aligned}
V = \sum_{l=1}^{4} V_l \approx \frac{V_0}{4} \Bigg[& \cos\left(\Omega_{RF} t + \phi\right) \left(\frac{A_1}{2} + \frac{x^2 - 2R_0 x + y^2 + R_0^2}{4z_0^2} - \frac{-x^2 - 2R_0 x + y^2}{R_0^2} \right) \\
& + \cos\left(\Omega_{RF} t\right) \left(\frac{A_1}{2} + \frac{x^2 + 2R_0 x + y^2 + R_0^2}{4z_0^2} - \frac{-x^2 + R_0 x + y^2}{R_0^2} \right) \\
& - \cos\left(\Omega_{RF} t\right) \left(A_1 + \frac{x^2 + y^2 + R_0^2}{2z_0^2} - 2\frac{x^2 - y^2}{R_0^2} \right) \Bigg] \\
= \frac{V_0}{4} \Bigg[& \cos\left(\Omega_{RF} t + \phi\right) \left(\left(\frac{A_1}{2} + \frac{x^2 + y^2 + R_0^2}{4z_0^2} - \frac{-x^2 + y^2}{R_0^2} \right) + \left(\frac{2x}{R_0} - \frac{R_0 x}{2z_0^2} \right) \right) \\
& + \cos\left(\Omega_{RF} t\right) \left(\left(\frac{A_1}{2} + \frac{x^2 + y^2 + R_0^2}{4z_0^2} - \frac{-x^2 + y^2}{R_0^2} \right) - \left(\frac{2x}{R_0} - \frac{R_0 x}{2z_0^2} \right) \right) \\
& - \cos\left(\Omega_{RF} t\right) \left(A_1 + \frac{x^2 + y^2 + R_0^2}{2z_0^2} - 2\frac{x^2 - y^2}{R_0^2} \right) \Bigg] \\
= \frac{V_0}{4} \Bigg[& \left(\cos\left(\Omega_{RF} t + \phi\right) + \cos\left(\Omega_{RF} t\right) \right) \left(\frac{A_1}{2} + \frac{x^2 + y^2 + R_0^2}{4z_0^2} - \frac{-x^2 + y^2}{R_0^2} \right) \\
& + \left(\cos\left(\Omega_{RF} t + \phi\right) - \cos\left(\Omega_{RF} t\right) \right) \left(\frac{2x}{R_0} - \frac{R_0 x}{2z_0^2} \right) \\
& - \cos\left(\Omega_{RF} t\right) \left(A_1 + \frac{x^2 + y^2 + R_0^2}{2z_0^2} - 2\frac{x^2 - y^2}{R_0^2} \right) \Bigg] \\
= \frac{V_0}{4} \Bigg[& \left(A_4 + \frac{x^2 + y^2}{2z_0^2} + 2\frac{x^2 - y^2}{R_0^2} \right) \cos\left(\frac{\phi}{2}\right) \cos\left(\Omega_{RF} t\right) \\
& + \left(\frac{R_0 x}{z_0^2} - \frac{4x}{R_0} \right) \sin\left(\frac{\phi}{2}\right) \sin\left(\Omega_{RF} t\right) \\
& - \left(A_4 + \frac{x^2 + y^2}{2z_0^2} - 2\frac{x^2 - y^2}{R_0^2} \right) \cos\left(\Omega_{RF} t\right) \Bigg] \\
= \frac{V_0}{4} \Bigg[& \left(A_4 + \frac{x^2 + y^2}{2z_0^2} \right) \left(\cos\left(\frac{\phi}{2}\right) - 1 \right) \cos\left(\Omega_{RF} t\right) \\
& + 2\frac{x^2 - y^2}{R_0^2} \left(\cos\left(\frac{\phi}{2}\right) + 1 \right) \cos\left(\Omega_{RF} t\right) + \left(\frac{R_0 x}{z_0^2} - \frac{4x}{R_0} \right) \sin\left(\frac{\phi}{2}\right) \sin\left(\Omega_{RF} t\right) \Bigg]
\end{aligned}
\tag{2.68}
$$

where $A_4 = A_1 + \frac{R_0^2}{2z_0^2}$. For $x^2 + y^2 \ll z_0^2$ and $R_0^2 \ll z_0^2$, we obtain

$$V \approx V_0 \frac{\cos(\phi/2) + 1}{2} \left(\frac{x^2 - y^2}{R_0^2} \right) \cos(\Omega_{RF} t) - \frac{V_0}{R_0} \sin\left(\frac{\phi}{2}\right) \sin(\Omega_{RF} t) x + A_5 \tag{2.69}$$

where $A_5 = \frac{V_0}{4} A_4 \left(\cos\left(\frac{\phi}{2}\right) - 1\right) \cos(\Omega_{RF} t)$.

Thus, the radial confinement is weakened by a factor of $\frac{\cos(\phi/2)+1}{2}$ and there is an extra time varying term that is dependent on x. The effect of the extra term is explored by evaluating the equation of motion.

Let U be the DC component of the electric potential from end electrodes.

$$U = \frac{U_0}{z_0^2} \left(z^2 - \frac{1}{2}\left(x^2 + y^2\right) \right) \tag{2.70}$$

The electric field due to the DC component in the x-direction is

$$\xi_{x,DC} = -\frac{dU}{dx} = \frac{U_0}{z_0^2} x \tag{2.71}$$

The electric field due to the RF component in the x-direction is

$$\xi_{x,RF} = -\frac{dV}{dx} = -\frac{V_0}{R_0^2} \left(\cos\left(\frac{\phi}{2} + 1\right) \right) \cos(\Omega_{RF} t) x + \frac{V_0}{R_0} \sin\left(\frac{\phi}{2}\right) \sin(\Omega_{RF} t) \tag{2.72}$$

The equation of motion in the x-direction is

$$\begin{aligned} \frac{d^2x}{dt^2} &= \frac{Q}{m}(\xi_{x,DC} + \xi_{x,RF}) \\ &= \left[\frac{U_0 Q}{m z_0^2} - \frac{V_0 Q}{m R_0^2} \left(\cos\left(\frac{\phi}{2}\right) + 1 \right) \cos(\Omega_{RF} t) \right] x + \frac{V_0 Q}{m R_0} \sin\left(\frac{\phi}{2}\right) \sin(\Omega_{RF} t) \end{aligned} \tag{2.73}$$

Rearranging Equation 2.73 gives

$$\frac{d^2x}{dt^2} - \left[\frac{U_0 Q}{m z_0^2} - \frac{V_0 Q}{m R_0^2} \left(\cos\left(\frac{\phi}{2}\right) + 1 \right) \cos(\Omega_{RF} t) \right] x = \frac{V_0 Q}{m R_0} \sin\left(\frac{\phi}{2}\right) \sin(\Omega_{RF} t) \tag{2.74}$$

Defining $\tau = \frac{\Omega_{RF}}{2} t$,

$$\frac{d^2x}{d\tau^2} + [a - 2q\cos(2\tau)]x = F\sin(2\tau) \tag{2.75}$$

where

$$a = -\frac{4U_0Q}{m\Omega_{RF}^2 z_0^2}, \quad q = -\frac{2V_0Q}{m\Omega_{RF}^2 R_0^2}\left(\cos\left(\frac{\phi}{2}\right)+1\right), \quad F = \frac{4V_0Q}{m\Omega_{RF}^2 R_0}\sin\left(\frac{\phi}{2}\right) \tag{2.76}$$

Equation 2.74 is an inhomogeneous second order differential equation. As in the case in Section 2.2, the general solution is of the form

$$x(\tau) = K_1 x_1(\tau) + K_2 x_2(\tau) + X \tag{2.77}$$

where $x_1(\tau)$ and $x_2(\tau)$ are linearly independent solutions to the Mathieu equation. X is the specific solution to the inhomogeneous form. Similar to Section 2.2, try

$$X = \sum_{k=-\infty}^{\infty} c_k e^{i2k\tau} \tag{2.78}$$

Plugging the form of X into the left-hand side of Equation 2.74 gives

$$\begin{aligned}
&\frac{d^2X}{d\tau^2} + [a - 2q\cos(2\tau)]X \\
&= \sum_{k=-\infty}^{\infty} c_k \frac{d^2}{d\tau^2}(e^{i2k\tau}) + [a - q(e^{i2\tau} + e^{-i2\tau})] \sum_{k=-\infty}^{\infty} c_k e^{i2k\tau} \\
&= \sum_{k=-\infty}^{\infty} -4k^2 c_k e^{i2k\tau} + a c_k e^{i2k\tau} - q c_k e^{i2(k+1)\tau} - q c_k e^{i2(k-1)\tau} \\
&= \sum_{k=-\infty}^{\infty} e^{i2k\tau}[-4k^2 c_k + a c_k - q c_{k-1} - q c_{k+1}]
\end{aligned} \tag{2.79}$$

Thus we can write Equation 2.74 as

$$\sum_{k=-\infty}^{\infty} e^{i2k\tau}[-4k^2 c_k + a c_k - q c_{k-1} - q c_{k+1}] = F\left(\frac{e^{i2\tau} - e^{-i2\tau}}{2i} = F'(e^{i2\tau} - e^{-i2\tau})\right) \tag{2.80}$$

where $F' = \frac{F}{2i}$. For $k = 1$,

$$-4c_1 + a c_1 - q c_0 - q c_2 = F' \tag{2.81}$$

Rearranging Equation 2.81 gives

$$c_1 = \frac{F' + q(c_0 + c_2)}{a - 4} \tag{2.82}$$

Similarly, for $k = -1$,

$$\begin{aligned} -4c_{-1} + ac_{-1} - ac_{-2} - qc_0 &= -F' \\ c_{-1} &= \frac{-F' + q(c_0 + c_{-2})}{a - 4} \end{aligned} \tag{2.83}$$

For $k \neq \pm 1$,

$$-4k^2 c_k + ac_k - qc_{k-1} - qc_{k+1} = 0 \tag{2.84}$$

and we have a recurrence relation similar to that of the original Mathieu equation. For $k > 1$,

$$\frac{c_k}{c_{k-1}} = \frac{1}{D_k - \frac{c_{k+1}}{c_k}} \tag{2.85}$$

For $k < -1$,

$$\frac{c_k}{c_{k+1}} = \frac{1}{D_k - \frac{c_{k-1}}{c_k}} \tag{2.86}$$

where

$$D_k = \frac{a - 4k^2}{q} \tag{2.87}$$

To obtain a first order estimation, set $c_{\pm 2} = 0$, which gives $c_0 = 0$ upon evaluation. The oscillation amplitude at the driving frequency then becomes

$$|c_{\pm 1}| \approx \frac{|F'|}{4} = \frac{V_0 Q}{2m\Omega_{RF}^2 R_0} \sin\left(\frac{\phi}{2}\right) \tag{2.88}$$

Thus, the effect of trans-phase shift introduces an excess micromotion of motional amplitude $\frac{V_0 Q}{m\Omega_{RF}^2 R_0} \sin\left(\frac{\phi}{2}\right)$ at the RF frequency.

2.3.4 Cis-amplitude Mismatch

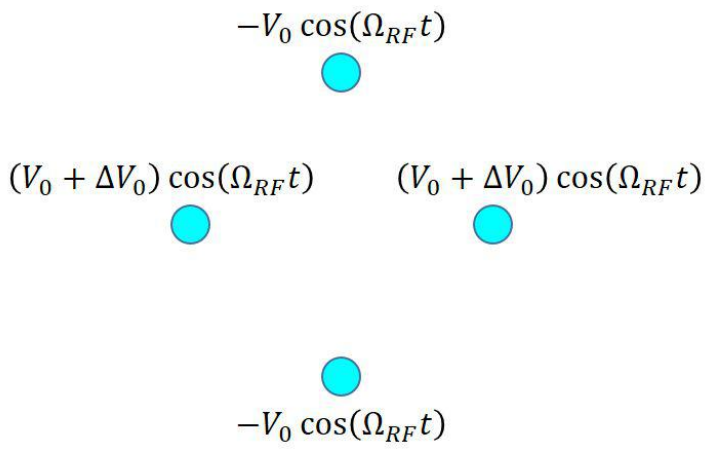

Figure 2.8: Illustration of cis-amplitude mismatch of ΔV_0 at line charge electrodes 2 and 4.

Similar to cis-phase shift, cis-amplitude mismatch is defined as one pair of electrodes opposite to each other having a voltage amplitude mismatch with the adjacent pairs as shown in Figure 2.8.

Evaluating the electric potential gives

$$\begin{aligned} V = \sum_{l=1}^{4} V_l &\approx \frac{\cos(\Omega_{RF}t)}{4}\left[(V_0+\Delta V_0)\left(A_1+\frac{x^2+y^2+R_0^2}{2z_0^2}+2\frac{x^2-y^2}{R_0^2}\right)\right. \\ &\left. - V_0\left(A_1+\frac{x^2+y^2+R_0^2}{2z_0^2}-2\frac{x^2-y^2}{R_0^2}\right)\right] \\ &= \frac{\cos(\Omega_{RF}t)}{4}\left[2(2V_0+\Delta V_0)\frac{x^2-y^2}{R_0^2}+\left(A_1+\frac{x^2+y^2+R_0^2}{2z_0^2}\right)\Delta V_0\right] \end{aligned} \tag{2.89}$$

The final form obtained is

$$V \approx \left(V_0+\frac{\Delta V_0}{2}\right)\frac{x^2-y^2}{R_0^2}\cos(\Omega_{RF}t)+\left(A_1+\frac{x^2+y^2+R_0^2}{2z_0^2}\right)\frac{\Delta V_0}{4}\cos(\Omega_{RF}t) \tag{2.90}$$

The resultant form from Equation 2.90 is

$$V \approx \left(V_0 + \frac{\Delta V_0}{2}\right)\frac{x^2 - y^2}{R_0^2}\cos\left(\Omega_{RF}t\right) + \left(A_1 + \frac{x^2 + y^2 + R_0^2}{2z_0^2}\right)\frac{\Delta V_0}{4}\cos\left(\Omega_{RF}t\right) \quad (2.91)$$

From Equation 2.91, cis-amplitude mismatch modifies radial confinement additively by $\frac{\Delta V_0}{2}$. The second term in the equation is negligible for large z_0. No excess micromotion is introduced.

2.3.5 Trans-amplitude Mismatch

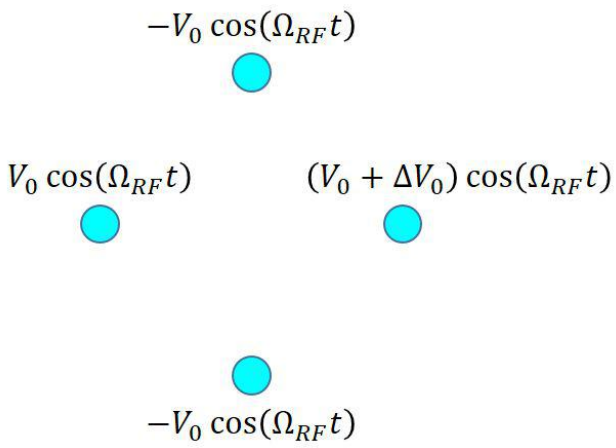

Figure 2.9: Illustration of trans-amplitude mismatch of ΔV_0 at line charge electrode 2.

Trans-amplitude mismatch is defined in this article as the case where an electrode has a RF amplitude mismatch with an opposite electrode. With similar evaluation in Section 2.3.3 for trans-phase shift, the potential experienced by an ion with trans-amplitude mismatch

as shown in Figure 2.9 is

$$
\begin{aligned}
V = \sum_{l=1}^{4} V_l \approx \frac{\cos(\Omega_{RF}t)}{4} \Bigg[& (V_0 + \Delta V_0) \left(\frac{A_1}{2} + \frac{x^2 - 2R_0x + y^2 + R_0^2}{4z_0^2} - \frac{-x^2 - 2R_0x + y^2}{R_0^2} \right) \\
& + V_0 \left(\frac{A_1}{2} + \frac{x^2 + 2R_0x + y^2 + R_0^2}{4z_0^2} - \frac{-x^2 + 2R_0x + y^2}{R_0^2} \right) \\
& - V_0 \left(A_1 + \frac{x^2 + y^2 + R_0^2}{2z_0^2} - 2\frac{x^2 - y^2}{R_0^2} \right) \Bigg] \\
= \frac{\cos(\Omega_{RF}t)}{4} \Bigg[& \left(V_0 + \frac{\Delta V_0}{2} \right) \left(A_4 + \frac{x^2 + y^2}{2z_0^2} + 2\frac{x^2 - y^2}{R_0^2} \right) + \Delta V_0 \left(\frac{R_0 x}{z_0^2} - \frac{4x}{R_0} \right) \\
& - V_0 \left(A_4 + \frac{x^2 + y^2}{2z_0^2} - 2\frac{x^2 - y^2}{R_0^2} \right) \Bigg] \\
= \frac{\cos(\Omega_{RF}t)}{4} \Bigg[& \frac{\Delta V_0}{2} \left(A_4 + \frac{x^2 + y^2}{2z_0^2} \right) + 4 \left(V_0 + \frac{\Delta V_0}{4} \right) \frac{x^2 - y^2}{R_0^2} \\
& + \Delta V_0 \left(\frac{R_0 x}{z_0^2} - \frac{4x}{R_0} \right) \Bigg]
\end{aligned}
\tag{2.92}
$$

For large z_0, the final form obtained is

$$
V \approx \left(V_0 + \frac{\Delta V_0}{4} \right) \frac{x^2 - y^2}{R_0^2} \cos(\Omega_{RF}t) - \frac{\Delta V_0}{R_0} x \cos(\Omega_{RF}t) + \frac{\Delta V_0}{8} A_4 \cos(\Omega_{RF}t) \tag{2.93}
$$

Thus, the transverse confinement is modified additively by $\frac{\Delta V_0}{4}$, and an excess micromotion is also introduced due to the second term in Equation 2.93. Evaluating the equation of motion gives

$$
\frac{d^2x}{d\tau^2} + [a - 2q\cos(2\tau)]x = F\cos(2\tau) \tag{2.94}
$$

where

$$
a = -\frac{4U_0Q}{m\Omega_{RF}^2 z_0^2}, \quad q = -\frac{4Q}{m\Omega_{RF}^2 R_0^2} \left(V_0 + \frac{\Delta V_0}{4} \right), \quad F = \frac{4\Delta V_0 Q}{m\Omega_{RF}^2 R_0} \tag{2.95}
$$

Similar to Section 2.3.3, we use

$$
X = \sum_{k=-\infty}^{\infty} c_k e^{i2k\tau} \tag{2.96}
$$

as a guess for the solution for the inhomogeneous differential equation in Equation 2.94. Plugging Equation 2.96 into Equation 2.94 gives

$$\sum_{k=-\infty}^{\infty} e^{i2k\tau}[-4k^2c_k + ac_k - qc_{k-1} - qc_{k+1}] = \frac{F}{2}(e^{i2\tau} + e^{-i2\tau}) \tag{2.97}$$

Evaluating the case for $k = 1$ and $k = -1$ gives

$$c_1 = c_{-1} = \frac{F/2 + q(c_0 + c_2)}{a - 4} \tag{2.98}$$

For $k = 0$, we get

$$c_0 = \frac{2qc_1}{a} \tag{2.99}$$

which implies that the ion is displaced from the origin. Making a first order approximation by setting $c_2 = 0$ and for the case $a \ll q^2$, evaluating $|c_1|$ gives

$$|c_1| \approx \frac{|aF|}{4q^2} \tag{2.100}$$

Thus, an excess micromotion of amplitude $\frac{|aF|}{2q^2}$ is introduced. However, it is noted that Equation 2.93 can be rewritten as

$$V \approx \left(V_0 + \frac{\Delta V_0}{4}\right)\frac{(x - \Delta x)^2 - y^2}{R_0^2}\cos(\Omega_{RF}t) + \frac{\Delta V_0}{8}A_4\cos(\Omega_{RF}t) - A_5\cos(\Omega_{RF}t) \tag{2.101}$$

where $\Delta x = \frac{\Delta V_0 R_0}{2(V_0 + V_0/4)}$ and $A_5 = \frac{\Delta V_0^2}{4V_0 + \Delta V_0}$. This indicates that the RF potential is effectively just shifted in the x-direction. By applying DC biasing voltages such that the DC null, which we define as the axial line where no force from the DC component of the potential acts on an ion in the transverse direction, matches the RF null, the excess micromotion can be eliminated.

2.3.6 Anisotropic Electrode Alignment

To break the degeneracy in the x and y motional frequencies, one way is to have an anisotropic electrode alignment [32]. It is thus also interesting to investigate the effect on

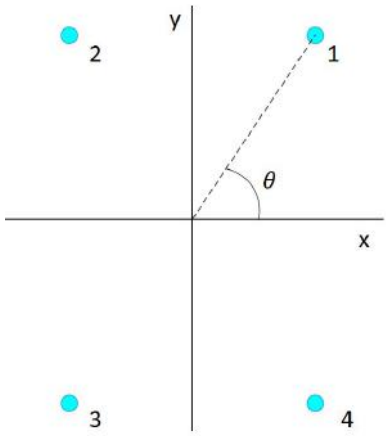

Figure 2.10: Sketch of an ion in a cross-section of a linear Paul trap with sets of line charges approximating the electrodes in an anisotropic configuration. Cyan circles represent the line charge electrodes.

the ion motion analytically with line charge approximations. With the setup as shown in Figure 2.10, the formulation for radial distance for each line charge is

$$\begin{aligned} r_1^2 &= (R_0\cos(\theta) - x)^2 + (R_0\sin(\theta) - y)^2 \\ r_2^2 &= (-R_0\cos(\theta) - x)^2 + (R_0\sin(\theta) - y)^2 \\ r_3^2 &= (-R_0\cos(\theta) - x)^2 + (-R_0\sin(\theta) - y)^2 \\ r_4^2 &= (R_0\cos(\theta) - x)^2 + (-R_0\sin(\theta) - y)^2 \end{aligned} \tag{2.102}$$

Evaluating the potential gives

$$\begin{aligned} V &\approx \frac{C}{4\pi\epsilon_0}\cos(\Omega_{RF}t)\left[\sum_{l=1}^{4}(-1)^l \ln\left(\frac{\sqrt{z_0^2 + r_l^2} + z_0}{\sqrt{z_0^2 + r_l^2} - z_0}\right)\right] \\ &\approx \frac{C}{4\pi\epsilon_0}\cos(\Omega_{RF}t)\left[\sum_{l=1}^{4}(-1)^l \left(A + \ln\left(1 + \frac{r_l^2}{4z_0^2}\right) - \ln(r_l^2)\right)\right] \\ &= \frac{C}{4\pi\epsilon_0}\cos(\Omega_{RF}t)\left[\ln(r_1^2 r_3^2) - \ln(r_2^2 r_4^2) + \sum_{l=1}^{4}(-1)^l \ln\left(1 + \frac{r_l^2}{4z_0^2}\right)\right] \end{aligned} \tag{2.103}$$

Evaluating $r_1^2 r_3^2$ and $r_2^2 r_4^2$ gives

$$\begin{aligned} r_1^2 r_3^2 &= (x^2 + y^2)^2 + R_0^4 + 2R_0^2\cos(2\theta)(y^2 - x^2) - 4xyR_0^2\sin(2\theta) \\ r_2^2 r_4^2 &= (x^2 + y^2)^2 + R_0^4 + 2R_0^2\cos(2\theta)(y^2 - x^2) + 4xyR_0^2\sin(2\theta) \end{aligned} \tag{2.104}$$

Making the approximation

$$\begin{aligned}
&\ln\left((x^2+y^2)^2 + R_0^4 + 2R_0^2\cos(2\theta)(y^2-x^2) \pm 4xyR_0^2\sin(2\theta)\right) \\
&= \ln R_0^4 + \ln\left(1 + \frac{(x^2+y^2)^2}{R_0^4} + \frac{2}{R_0^2}\cos(2\theta)(y^2-x^2) \pm \frac{4xy}{R_0^2}\sin(2\theta)\right) \\
&\approx \ln R_0^4 + \frac{(x^2+y^2)^2}{R_0^4} + \frac{2}{R_0^2}\cos(2\theta)(y^2-x^2) \pm \frac{4xy}{R_0^2}\sin(2\theta))
\end{aligned} \tag{2.105}$$

Thus, the potential is

$$V \approx \frac{C}{4\pi\epsilon_0}\cos(\Omega_{RF}t)\left[-\frac{8xy\sin(2\theta)}{R_0^2} + \sum_{l=1}^{4}(-1)^l \ln\left(1+\frac{r_l^2}{4z_0^2}\right)\right] \tag{2.106}$$

For large z_0, as shown in Section 2.3.1, $\ln\left(1+\frac{r_l^2}{4z_0^2} \approx 0\right)$, and we obtain

$$V \approx -\frac{2C}{\pi\epsilon_0}\left[\frac{xy\sin(2\theta)}{R_0^2}\right]\cos(\Omega_{RF}t) \tag{2.107}$$

Rotating the frame of reference such that $x' = \frac{1}{\sqrt{2}}(x+y)$ and $y' = \frac{1}{\sqrt{2}}(y-x)$, Equation 2.107 becomes

$$V \approx \frac{C}{\pi\epsilon_0}\left[\frac{x^2-y^2}{R_0^2}\sin(2\theta)\cos(\Omega_{RF}t)\right] \tag{2.108}$$

which is the same form as Equation 2.63, but scaled by a factor of $\sin(2\theta)$. This also implies that the RF component of the potential does not contribute to any anisotropy, it is the DC component that results in anisotropy in the trap.

2.4 Trap Designs

For a realistic Paul trap for quantum computation, hyperbolic shaped electrodes are impractical as this architecture severely limits optical access for light collection and optical addressing. The common options which can be manually assembled are the four-rod design and the blade trap, as mentioned in the Introduction. In a four-rod trap, 4 cylindrical rods replace the 4 hyperbolic electrodes in the idealized Paul trap and 2 needle electrodes replace the idealized endcap electrodes. For the four-rod trap, we follow the design as described in Ref. [10], with some modifications to the electrode mounts and needle spacing. A computer-aided design (CAD) drawing of it can be found in Figure 2.11. With a

deviated electrode architecture from the theoretical Paul trap, the potential at the trap centre is modified with some geometrical factors [9]

$$\begin{aligned} V &= \kappa_{RF} V_0 \frac{x^2 - y^2}{r_0^2} \cos\left(\Omega_{RF} t\right) \\ U &= \kappa_{DC} U_0 \left(\frac{z^2}{z_0^2} - \frac{x^2 + y^2}{2 z_0^2} \right) \end{aligned} \tag{2.109}$$

where κ_{RF} and κ_{DC} are the RF and DC geometrical factors, and they depend on the trap geometry.

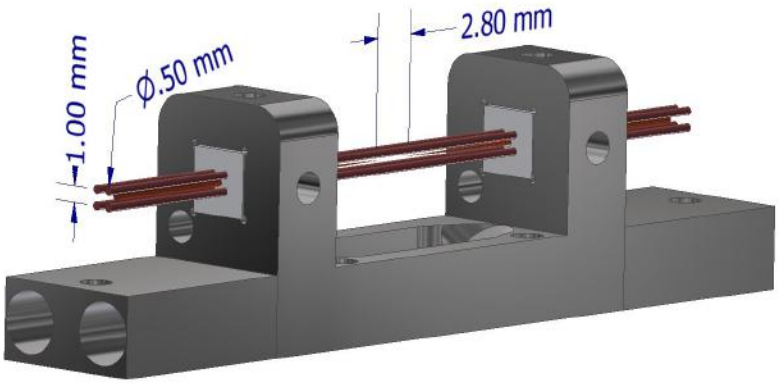

Figure 2.11: CAD drawing of our four-rod trap.

For our blade trap, we follow the design as outlined in Ref. [32], with some modifications to the blade design and assembly geometry (see Figure 2.12a). In our blade trap, 4 blade electrodes are placed in an anisotropic manner as shown in Figure 2.12b. The reason for the anisotropic geometry is to break the degeneracy of secular frequencies in the transverse motion of the ions. Each blade is segmented into 5 parts. RF voltages are applied to all the segments of each blade. The RF voltages for a pair of electrodes that are opposite to each other are in phase and 180° out of phase with the other pair, which provides confinement in the transverse direction. A relatively high voltage is applied to the end segments of each blade. This provides axial confinement for the ions and effectively acts as "endcap" electrodes. Technically, this is already sufficient to trap ions and it is unnecessary

to separate the middle segments into the remaining 3 parts. However, the additional segmentation allows better control of the electric potential which helps in micromotion compensation of an ion chain and enables more complex potential functions, such as a quartic potential, should they be desired. Each middle segment is 250 μm wide at the trap centre and they are separated by 50 μm gaps. In our finalized design, we have chosen $r_0 = 200\,\mu$m.

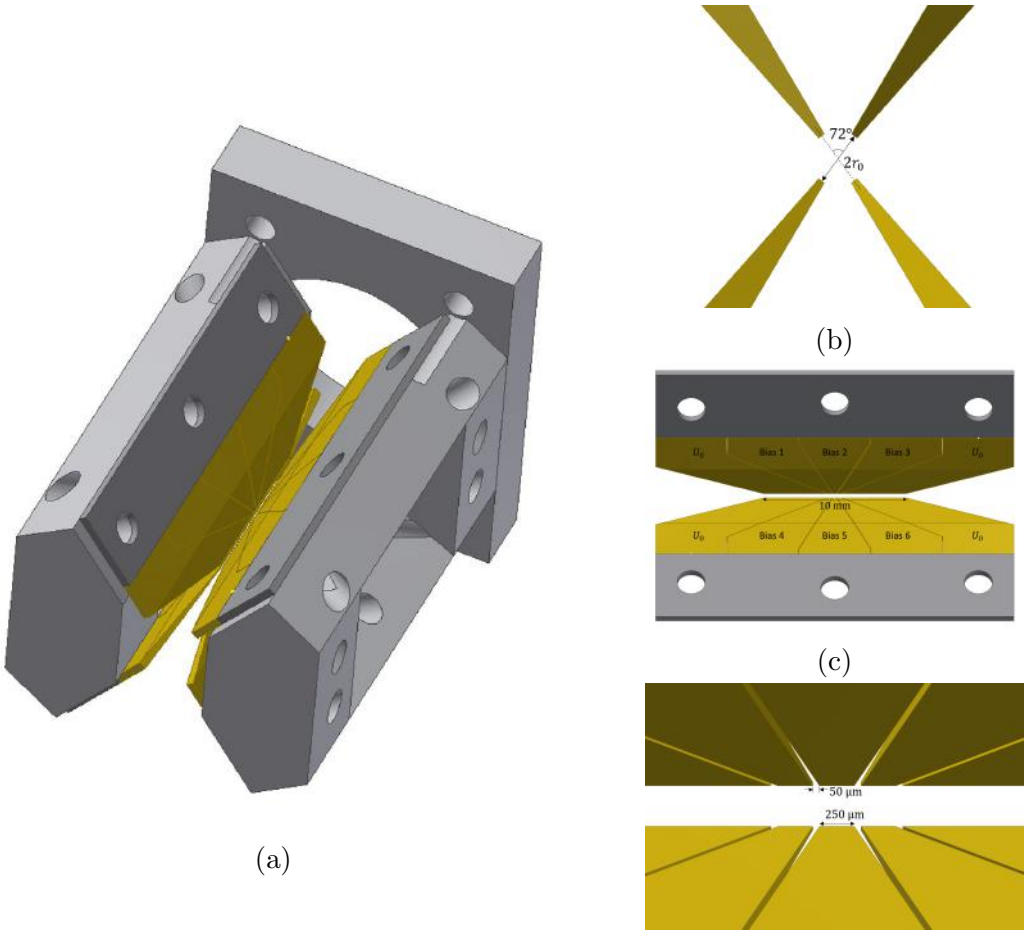

(a)

(b)

(c)

(d)

Figure 2.12: (a) CAD drawing of our blade trap on a mount. (b) xy-plane view of the blade electrodes. (c) yz-plane view of the blade electrodes, with the DC voltages labelled. (d) Zoomed in version of the yz-plane view of the blade electrodes.

2.5 Numerical Simulations of Ion Trap

SIMION is used to numerically simulate the motion of an ion in an ion trap. First, 3-dimensional (3D) electrode configurations are designed with a CAD program. The 3D drawing of the electrodes are then exported in STL format, which is compatible with SIMION. SIMION then converts the STL files to potential array (PA) files, which is a grid of potential values that form the basis functions of the electrodes. SIMION first generates a 3D array, for the grid points where there are overlaps with the surfaces on the STL files, SIMION sets them as "electrode points". These electrode points are used as boundary conditions when solving for the Laplacian of the electrostatic field. Once the solution for the Laplacian has converged, the potential array is saved as a PA file. The potential at a point in free space is a simple summation of the basis functions of each of the electrodes. A Lua script is used to control the potential of each electrode. With the charge, mass, initial position and velocity of an ion set in SIMION, the ion is allowed to "fly" in the simulation space. The acceleration of the ion is simply computed from the potential at the position of the ion generated by the electrodes. The position of the ion is recorded at each time step specified in SIMION. The trajectory files are then exported.

To ensure that an ion is moving at a low temperature, the ion starting position is set at the pseudopotential minimum of the trap. The pseudopotential minimum of the trap can be obtained by calculations and interpolations from the basis functions of the electrode. From Ref. [10], the pseudopotential from the RF component can be computed from

$$V_p = \frac{Q\left(\xi_0(x,y,z)\right)^2}{4m\Omega_{RF}^2} \tag{2.110}$$

where $\xi_0(x,y,z)$ is the electric field amplitude of the RF component in 3D space. The net pseudopotential is then the summation of the RF pseudopotential with the static potential. Alternatively, it can also be done by first running a simulation with an ion inside the trap. The ion trajectory is then passed through a low-pass filter using MATLAB to filter off micromotions. The position where the secular motion has the maximum speed is then computed. This position corresponds to the point where the pseudopotential is a minimum. I find that the latter technique to be more convenient as the first method would require processing and interpolating a 3D matrix, which is computationally more demanding. With the trajectory files, Fourier analysis can be performed to extract the motional amplitudes of the different frequencies. The excess micromotion is of particular interest due to the adverse effects as outlined in Section 2.2 and serves to quantify the severity of the impact of certain experimental imperfections. As shown in Sections 2.2 and 2.3, excess micromotion introduces a Fourier component at exactly the RF frequency,

Ω_{RF}. From Section 2.1, intrinsic micromotion manifests itself in the Fourier space as finite Fourier amplitudes at $\Omega_{RF} \pm \omega_s$. Thus, excess micromotion can be easily distinguished from intrinsic micromotion in the Fourier space. To quantify the level of excess micromotion in an ion trajectory, the Fourier amplitude at Ω_{RF} is obtained, which is then used to compute the maximum kinetic energy of the excess micromotion.

$$KE_{emm} = \frac{1}{2} m \Omega_{RF}^2 A_{emm}^2 \tag{2.111}$$

where KE_{emm} is the maximum kinetic energy of the excess micromotion, m is the mass of the ion, and A_{emm} is the Fourier amplitude of the excess micromotion.

2.5.1 Trap parameters

It is not straightforward to determine the trap parameters for the desired secular frequencies due to the unknown geometric factors as seen in Equation 2.109. Thus, simulations are performed to obtain the trap parameters for the trap geometries as outlined in Section 2.4. $^{133}Ba^+$ is one of the ion species that we intend to trap and the simulations are done with an ion of mass $m = 133\,\text{amu}$.

For the four-rod trap, the following parameters are used $\Omega_{RF} = 2\pi \times 20\,\text{MHz}$, $V_0 = 200\,\text{V}$, $U_0 = 250\,\text{V}$. Additionally, 2 V voltages are applied to a pair of opposing electrodes to break the degeneracy in the transverse secular motion. The resultant transverse motional frequencies obtained are $\omega_{s,1} = 2\pi \times 1.11\,\text{MHz}$ and $\omega_{s,2} = 2\pi \times 1.25\,\text{MHz}$. The axial motional frequency obtained is $\omega_z = 2\pi \times 250\,\text{kHz}$.

For the blade trap, the parameters $\Omega_{RF} = 2\pi \times 35\,\text{MHz}$, $V_0 = 304\,\text{V}$, $U_0 = 50\,\text{V}$ result in the following motional frequencies: $\omega_{s,1} = 2\pi \times 4.65\,\text{MHz}$, $\omega_{s,2} = 2\pi \times 4.80\,\text{MHz}$ and $\omega_z = 2\pi \times 1.10\,\text{MHz}$.

It is observed that the ion trajectory from a simulation still has transverse excess micromotion from DC and RF null mismatch, even when the trap is perfectly symmetric and in perfect alignment. This is speculated to be due to asymmetry of the sequence in solving for the Laplacian when SIMION is computing the electrode basis functions. DC biases are applied to correct for the DC and RF null mismatch. The method to obtain the bias voltages will be described in Section 2.5.5. For the subsequent sections, simulations with experimental imperfections are done exclusively for the blade trap, as that trap geometry is the one of interest regarding tolerable imperfections.

2.5.2 Cis-phase shift

From Section 2.3.2, it is derived that cis-phase shift results in weakening of radial confinement by a factor of $\cos\left(\frac{\phi}{2}\right)$. It effectively transforms RF voltage amplitude from V_0 to $V_0 \cos\left(\frac{\phi}{2}\right)$. From Equation 2.34, it can be seen that for the case where $a \ll \frac{q^2}{2}$,

$$\omega_s \approx \frac{q}{\sqrt{2}} \propto V_0 \tag{2.112}$$

This indicates that from the ion trajectory, we should observe that cis-phase shift shifts the secular frequency by a factor of $\cos\left(\frac{\phi}{2}\right)$.

$$\omega_s \propto \cos\left(\frac{\phi}{2}\right) \tag{2.113}$$

From Equations 2.6, 2.39 and 2.34, the magnitudes of the a and q parameters can be computed from the motional frequencies and the RF frequency as

$$\begin{aligned} |a| &= \frac{2\omega_z^2}{\Omega_{RF}^2} \\ q &\approx \sqrt{\frac{8\omega_s^2}{\Omega_{RF}^2} - 2a} \end{aligned} \tag{2.114}$$

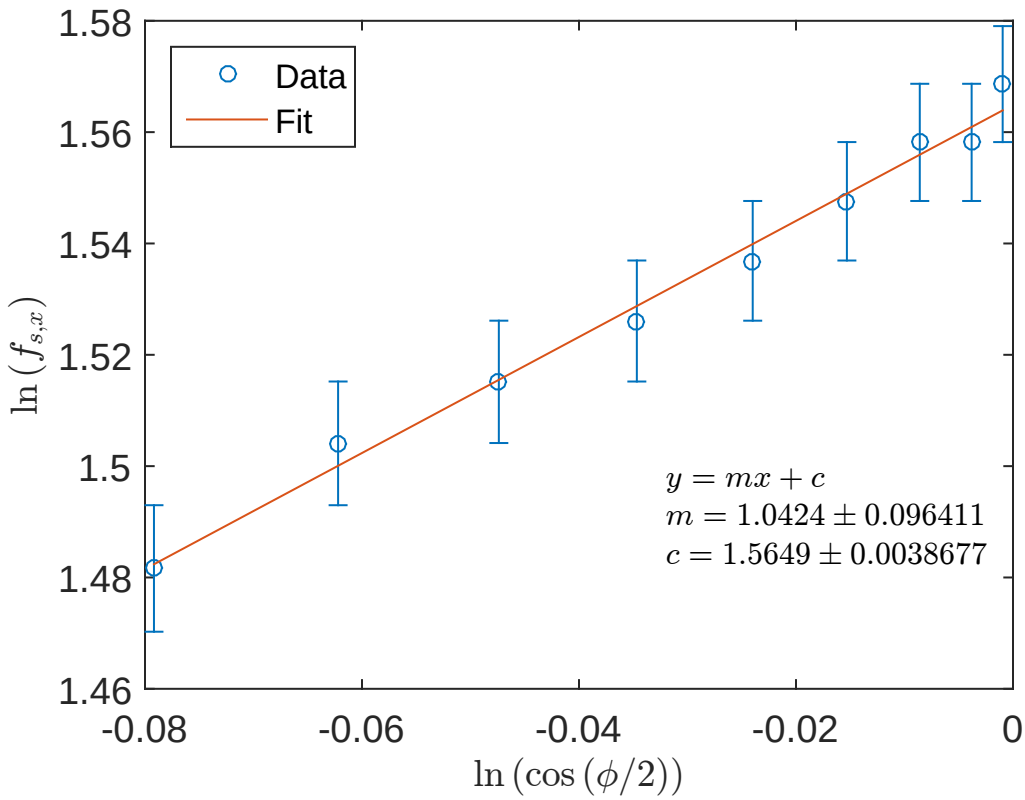

Figure 2.13: $\log - \log$ plot of $f_{s,x}$ against $\cos\left(\frac{\phi}{2}\right)$ from simulations with our blade trap. $f_{s,x} = \frac{\omega_{s,x}}{2\pi}$ is the x-motion secular frequency in MHz. The error bar for each data point is computed from $\frac{\Delta f}{f_{s,x}}$, where $\Delta f = 0.05\,\text{MHz}$ is the frequency resolution in the Fourier space from a simulation trajectory time of $20\,\mu\text{s}$.

For our blade trap, the a and q parameters for the x-motion are derived from Equation 2.114 to be $|a| = 0.002$ and $q = 0.393$, which satisfies $a \ll \frac{q^2}{2}$. This indicates that from the ion trajectory, we should observe that cis-phase shift shifts the secular frequency by a factor of $\cos\left(\frac{\phi}{2}\right)$. Simulations on the blade trap is performed to verify the relation as outlined in Equation 2.113. A $\log - \log$ plot of $\frac{\omega_{s,x}}{2\pi}$ against $\cos\left(\frac{\phi}{2}\right)$ is shown in Figure 2.13. A gradient of 1.0 ± 0.1 is obtained, which is consistent with the prediction. Excess micromotion is also verified to be small ($KE_{emm,x} < 0.02\,\text{mK}$ even at $\phi = 45°$ cis-phase shift), which is consistent with the prediction from line charge approximation in Section 2.3.2.

2.5.3 Trans-phase shift

From line charge approximation in Section 2.3.3, A_{emm} is expected to be proportional to $\sin\left(\frac{\phi}{2}\right)$. From simulations with the blade trap, this relation is verified as shown in Figure 2.14. $\log - \log$ plot of A_{emm} against $\sin\left(\frac{\phi}{2}\right)$ from simulations give a gradient of 0.9989 ± 0.0005, which is very close to the expected value of 1.

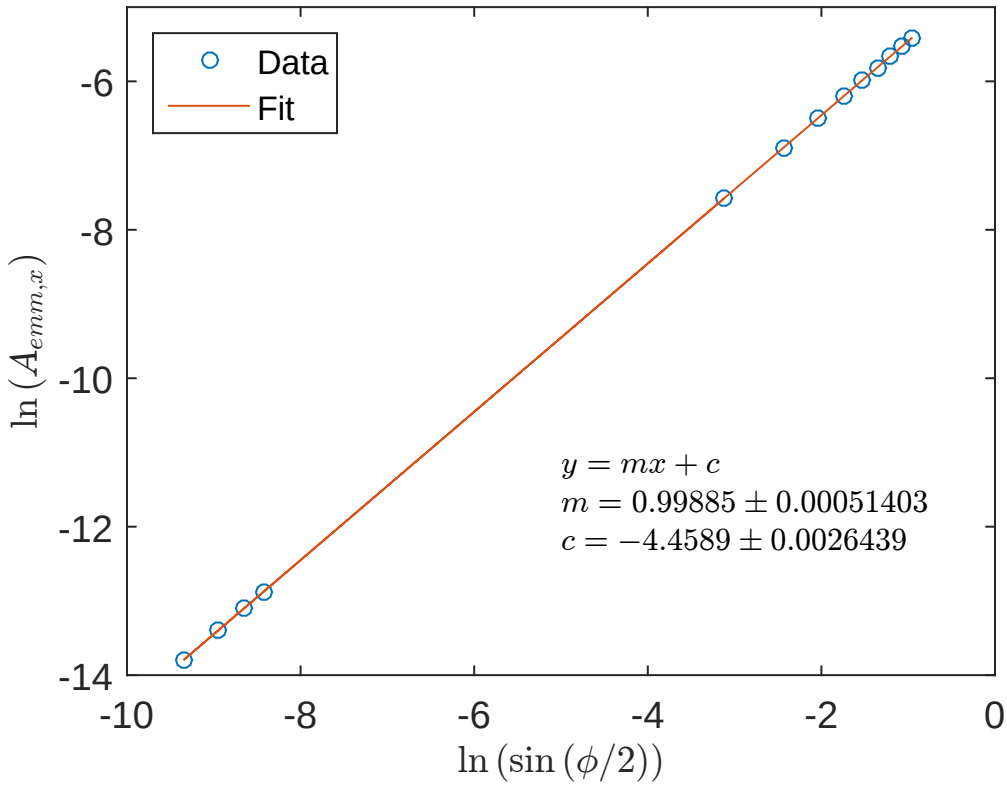

Figure 2.14: $\log - \log$ plot of $A_{emm,x}$ against $\sin\left(\frac{\phi}{2}\right)$ from simulations with our blade trap.

The excess micromotion kinetic energies are also evaluated with and without the DC voltages turned on. This is to verify that this excess micromotion is not due to DC and RF null mismatch, By turning off the DC voltages, every point in space is a DC null point. If the excess micromotion still persists, it implies that it cannot be compensated with DC bias voltages. With $\phi = 10°$ of trans-phase shift, the excess micromotion kinetic energies in the x-direction are $KE_{emm,x} = 400\,\mathrm{K}$ and $KE_{emm,x} = 396\,\mathrm{K}$ with and without DC voltages

turned on respectively. Thus, minimizing trans-phase shift is critical for a linear Paul trap. From the simulations, trans-phase shift has to be $\phi < 0.022°$ for excess micromotion kinetic energy below 2 mK.

2.5.4 Cis-amplitude mismatch

From Section 2.3.4, the transverse confinement is expected to be scaled by a factor of $1 + \frac{\Delta V_0}{2V_0}$ when a cis-amplitude mismatch of ΔV_0 is present. This implies that the secular motion frequency is proportional to $V_0 + \frac{\Delta V_0}{2}$ with cis-amplitude mismatches for $|a| \ll \frac{q^2}{2}$. $\log - \log$ plot of $f_{s,x}$ against $V_0 + \frac{\Delta V_0}{2}$ is obtained from simulations with our blade trap (see Figure 2.15). The gradient obtained of 1.0 ± 0.1 verifies the relation between secular motion frequency and cis-amplitude mismatch. It is also verified that a cis-amplitude mismatch does not cause excess micromotion – $KE_{emm,x} < 0.0004$ mK is still low with $\Delta V_0 = 45$ V of cis-amplitude mismatch.

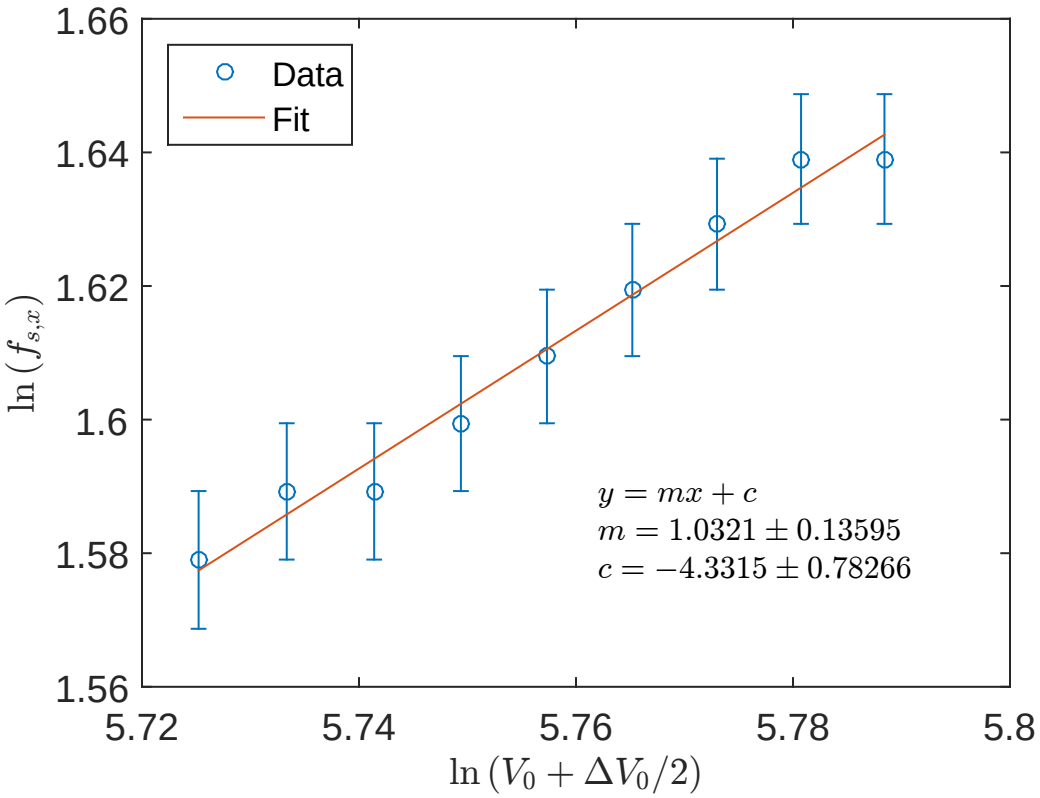

Figure 2.15: $\log - \log$ plot of $f_{s,x}$ against $V_0 + \frac{\Delta V_0}{2}$ from simulations with our blade trap with $V_0 = 304\,\mathrm{V}$. The error bar for each data point is computed from $\frac{\Delta f}{f_{s,x}}$, where $\Delta f = 0.05\,\mathrm{MHz}$ is the frequency resolution in the Fourier space from a simulation trajectory time of $20\,\mu\mathrm{s}$.

2.5.5 Trans-amplitude mismatch

Derivations from line charge approximation in Section 2.3.5 predict that trans-amplitude mismatch results in DC and RF null mismatch, which introduces excess micromotion. However, this can be corrected by applying DC biasing voltages to adjust the DC null line to match with the RF null. I explored using additional electrodes to act as bias electrodes with some early simulations. To ensure that the additional electrodes do not restrict optical access, they are placed behind the blade electrodes. As an extreme case, 1 cm wide plates are placed at 12.6 mm away from the centre of the trap. For this early simulation, the trap parameters for the designed have not yet been finalized, and the trap parameters

$r_0 = 125\,\mu$m, $\Omega_{RF} = 120\,$MHz, $V_0 = 400\,$V, $U_0 = 500\,$V were used for this test.

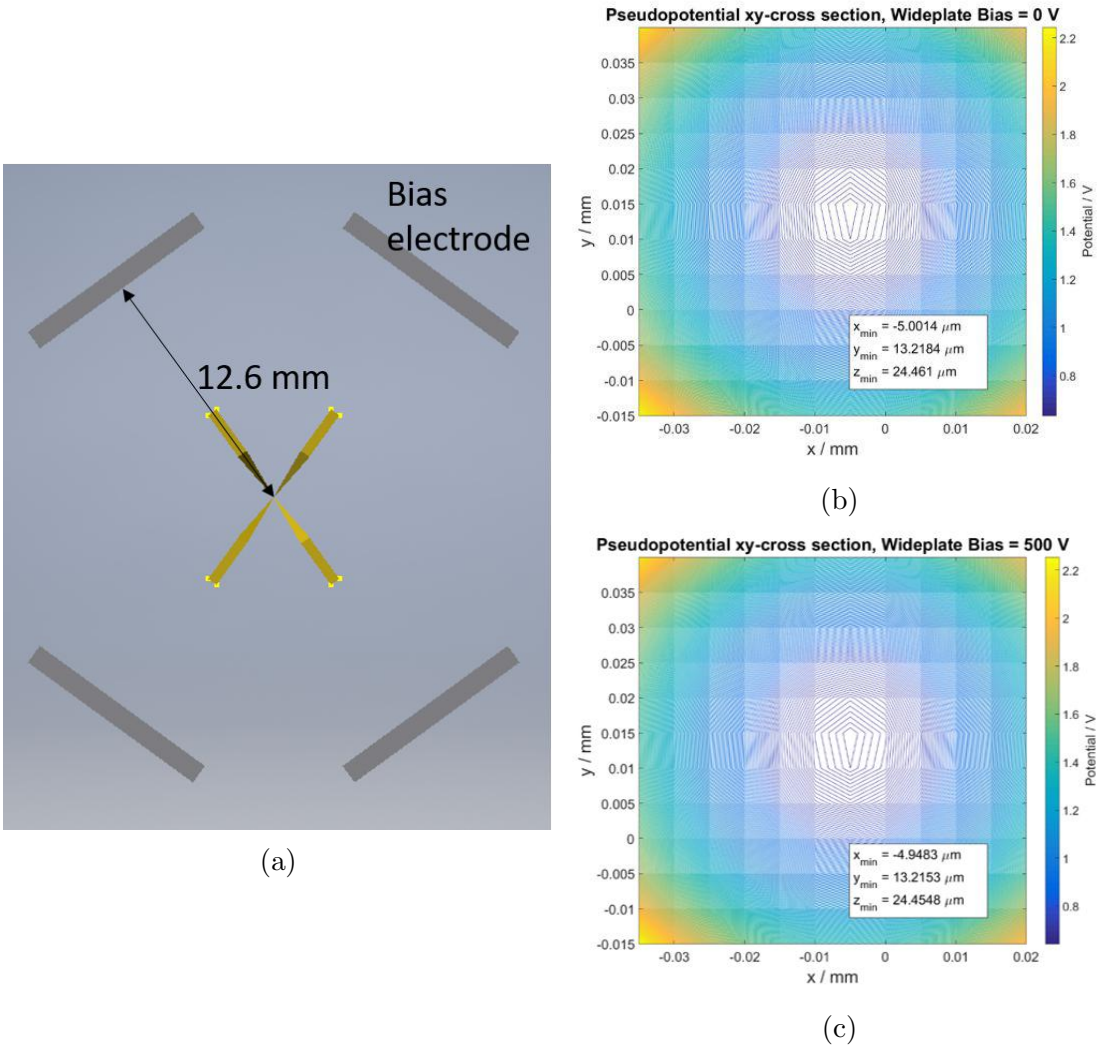

(a)

(b)

(c)

Figure 2.16: (a) Geometry of electrodes used for testing external bias electrodes. (b) Pseudopotential in the xy-plane at the minimum point with 0 V applied to bias electrodes. (c) Pseudopotential in the xy-plane at the minimum point with 500 V applied to one bias electrode. x_{min}, y_{min} and z_{min} denote the coordinate of the minimum point of the pseudopotential.

From this test, the computed pseudopotential minimum barely shifts even with 500 V applied to one of the wide bias electrodes as shown in Figure 2.16. This shows that DC

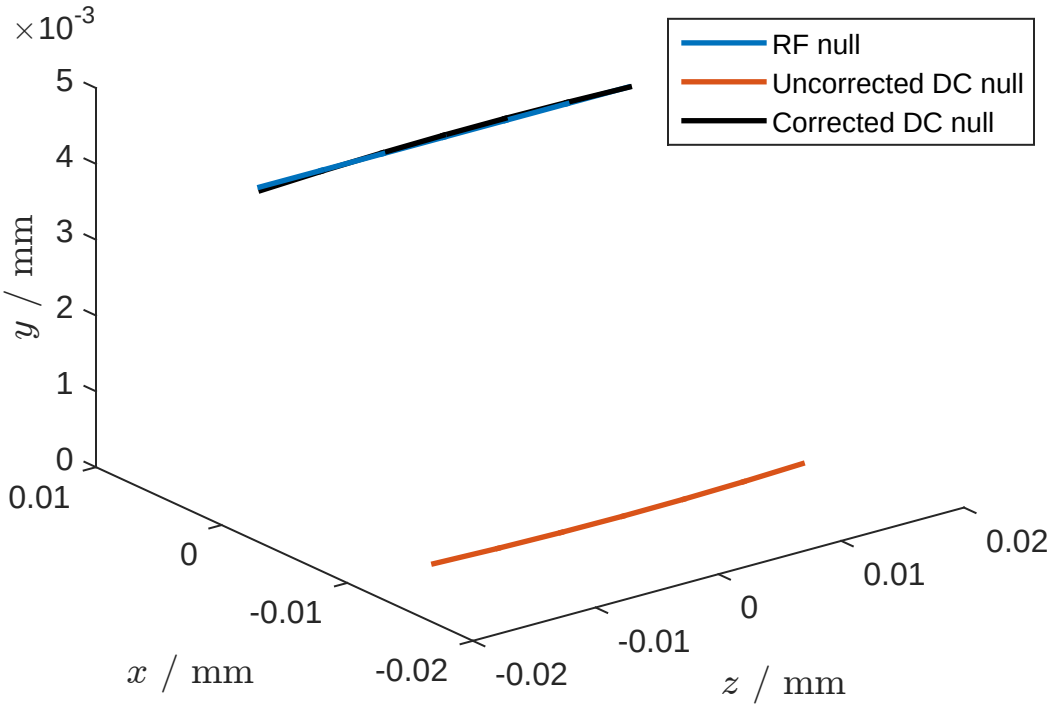

Figure 2.17: 3D plot of RF and DC null lines.

bias has to be applied on the blade segments (see Figure 2.12c) and also highlights another advantage of a blade trap over the four-rod trap, which is good isolation from external electric field. To obtain the DC null and RF null lines, the points with zero electric field in the transverse direction, defined as the xy-plane, for the DC and RF components are computed for each point in the axial direction. The DC null line shifts with varying DC biases on the blade segment. To match the DC null to the RF null, the voltages on the middle 3 segments of each of the blade (12 parameters in total) are allowed to vary freely while nonlinear regression is performed in MATLAB to minimize the residual square of the RF and DC null points in the xy-plane for each point in the axial direction. The output of the parameters for the middle blade segment voltages once the nonlinear regression has converged corresponds to the appropriate voltages to be applied to the middle segments for micromotion compensation.

To test if a trans-amplitude mismatch can be corrected, the aforementioned algorithm is used to correct for DC and RF null mismatch for our blade trap as described in Section 2.4, trap parameters as described in Section 2.5.1 and a trans-amplitude mismatch of $\Delta V_0 = 40\,\mathrm{V}$. Figure 2.17 shows the RF and DC nulls before and after applying DC bias voltages for mismatch correction. It can be seen that the corrected DC null matches much closer with the RF null. The x and y-excess micromotion energies before applying the correcting bias voltages are $KE_{emm,x} = 661\,\mathrm{mK}$ and $KE_{emm,y} = 3.34\,\mathrm{mK}$ respectively. After correction, the x and y-excess micromotion energies are drastically reduced to $KE_{emm,x} = 1.19 \times 10^{-2}\,\mathrm{mK}$ and $KE_{emm,y} = 1.07 \times 10^{-3}\,\mathrm{mK}$. This confirms that trans-amplitude mismatch is a tolerable imperfection as long as the option to apply DC biasing voltages is available.

2.5.6 Geometric misalignment

As mentioned in the introduction, there are more degrees of freedom in assembling a blade trap. Figure 2.18 shows the possible geometric misalignment considered for a blade electrode in our blade trap.

For the axially-symmetric translation of a blade electrode as shown in Figures 2.18a, the tests were done with an unfinalized design of the trap, with parameters $r_0 = 277.5\,\mu\mathrm{m}$, $\Omega_{RF} = 24\,\mathrm{MHz}$, $V_0 = 400\,\mathrm{V}$, $U_0 = 50\,\mathrm{V}$. From the simulations, it is found that geometric misalignment that are axially symmetric only introduce excess micromotion in the transverse direction and not in the axial direction. The transverse excess micromotion can be compensated with bias electrodes to shift the DC null to be aligned with the RF null.

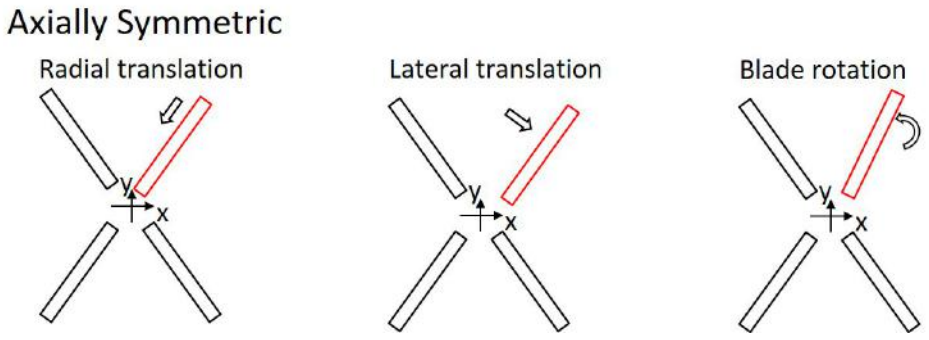

(a)

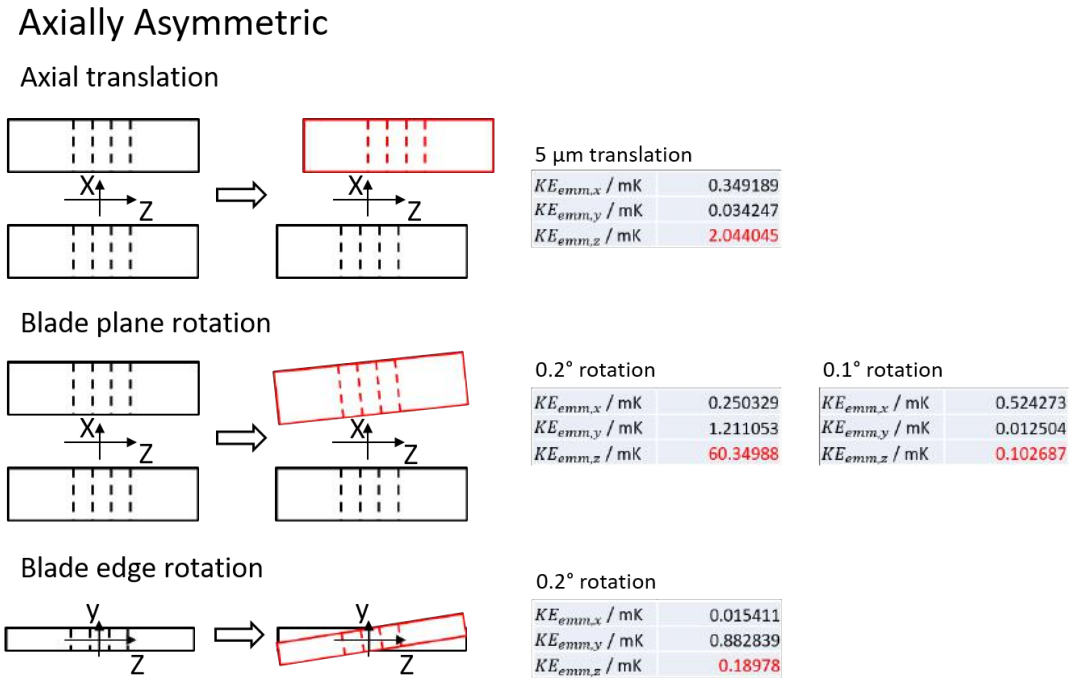

(b)

Figure 2.18: Illustrations of blade electrode misalignment. (a) Axially-symmetric misalignment (b) Axially-asymmetric misalignment with simulated excess micromotion kinetic energy.

The excess micromotion with and without correcting with DC biases when one of the blade electrodes is displaced laterally or radially is shown in Table 2.1. From the table,

		$KE_{emm,x}$/mK	$KE_{emm,y}$/mK	$KE_{emm,z}$/mK
Radial displacement $-30\,\mu$m	Uncorrected	4.64×10^2	5.02×10^3	2.74×10^{-7}
	DC corrected	1.84	4.34×10^{-3}	4.80×10^{-1}
Lateral displacement $25\,\mu$m	Uncorrected	8.92×10^2	2.08×10^3	1.65×10^{-6}
	DC corrected	3.89×10^{-4}	2.23×10^{-4}	3.83×10^{-3}
Blade rotation 1°	Uncorrected	6.27	2.00×10^2	1.07×10^{-1}
	DC corrected	1.88×10^{-2}	7.85×10^{-1}	5.02×10^{-3}

Table 2.1: Kinetic energy of excess micromotion for each motional axis for geometric misalignment that are axially symmetric.

it can be seen that the excess micromotion in the transverse directions are effectively eliminated by correcting with DC biases. For the case of radial displacement, $KE_{emm,y} = 1.84\,\text{mK}$ did not go below sub-mK figures as there is still some DC and RF null mismatch at the minimum point for a single ion. Since the DC and RF null matching algorithm optimizes for the matching of the null line instead of a single null point, the DC and RF null offset at the minimum point is not guaranteed to be optimized.

For geometric misalignment that are not axially symmetric, excess micromotion along the axial direction is introduced. This excess micromotion cannot be compensated with DC biasing as there is no RF null point in the axial direction when there is an axially-asymmetric misalignment. Thus, these alignment are the ones that are critical to attend to. 2 mK is set as the target excess micromotion threshold that we do not want to exceed. The simulations for these critical misalignment are done with the finalized parameters for our blade trap, which are $r_0 = 200\,\mu$m, $\Omega_{RF} = 35\,\text{MHz}$, $V_0 = 304\,\text{V}$, $U_0 = 50\,\text{V}$. Figure 2.18b summarizes the simulation results for each misalignment. For the translation along the trap axis, $5\,\mu$m of displacement is the critical point. For blade plane rotation, the required accuracy is 0.1°. For blade edge rotation, it is found that 0.2° of misalignment is tolerable. Further misalignment of the blade edge rotation is not investigated further as accuracy within 0.2° is easily achievable with a mount for the blade electrodes.

Chapter 3

Voltage Sources for Paul Trap

In Chapter 2, it is shown that an oscillating voltage applied to trap electrodes is required to create a Paul trap. In addition, static voltages are required to provide axial confinement as well as variable voltages for matching RF and DC nulls in order to compensate for excess micromotions. In this chapter, my work on building RF and DC sources for a four-rod trap is presented. Section 3.1 describes the procedures and specifications of an RF resonator built for our four-rod trap while Section 3.2 provides details on a custom-made box and boards designed to provide variable static voltages to a four-rod trap. Section 3.3 describes how the voltage sources are connected to the electrodes in the vacuum chamber.

3.1 Helical RF Resonator

As seen in Chapter 2, high RF voltage amplitudes are required to trap ions at our desired motional secular frequency. An RF resonator allows us to construct a resonant circuit at the desired resonance with a high quality factor (Q-factor) and impedance matching from an RF source to ensure maximal power transfer to the ion trap. This enables high RF voltages at the ion trap [33]. The scheme of applied voltages as described in Chapter 2 pertains to a balanced RF drive, where one terminal of the RF source is 180° out of phase with the other. In contrast, in an unbalanced drive, one terminal will be grounded while the other is oscillating. We chose to build a balanced drive resonator due to the advantages of requiring half of the RF voltage amplitude to achieve the desired trap parameters as well as the system being free from ground noise. For example, an RF voltage amplitude of 200 V is desired for our four-rod trap using a balanced drive. Using an unbalanced drive,

an opposing pair of electrodes are grounded while the other pair has to be driven with a voltage amplitude of 400 V.

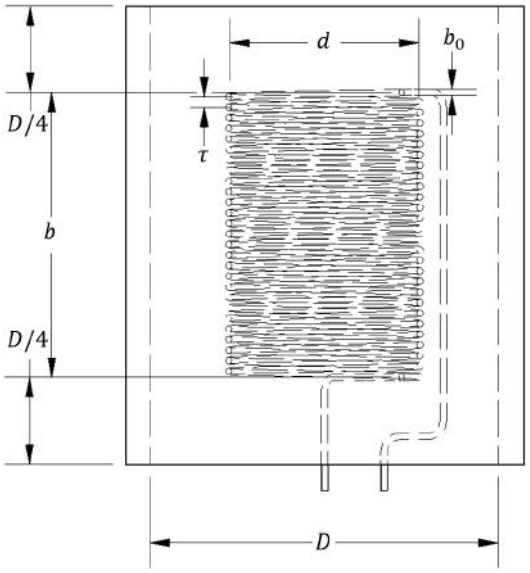

Figure 3.1: Sketch of a balanced drive resonator.

From the simulations in Section 2.5.1, an RF frequency of 20 MHz is required. As a rough guide, we follow the design guide as in Ref. [34] to construct a resonator geometry corresponding to 20 MHz even though it is a guide for an unbalanced drive resonator. The geometry of the resonator is a cylindrical copper with a copper helical coil within it as shown in Figure 3.1. Following the reference, the set of formulae to follow are

$$N = \frac{1900}{f_0 D} \tag{3.1}$$

$$\frac{d}{D} = 0.55 \tag{3.2}$$

$$\tau = \frac{f_0 D^2}{2300} \tag{3.3}$$

$$0.4 < \frac{d_0}{\tau} < 0.6 \quad \text{for } \frac{b}{d} = 1.5 \tag{3.4}$$

where N is the number of windings of the coil, f_0 is the desired resonance frequency in MHz, D is the inner diameter of the copper cylinder in inches, d is the coil diameter in

inches, τ is the pitch of the coil, d_0 is the diameter of the copper wire of the coil, b is the length of copper coil. From commercially available copper cylinders, $D = 3.5$ inches is the largest we could find. With this value of D, the parameters corresponding to $f_0 = 20\,\mathrm{MHz}$ are $N = 27$, $\tau = 2.7\,\mathrm{mm}$. Corresponding to this pitch, we chose American wire gauge (AWG) 14 copper wires, where $d_0 = 1.628\,14\,\mathrm{mm}$, which gives $\frac{d_0}{\tau} \approx 0.6$. To convert the design of an unbalanced drive resonator to a balanced version, instead of grounding one end of the coil to the copper cylinder, it is directed to the exit of a copper cap where it will be connected to the trap electrodes as shown in Figure 3.1.

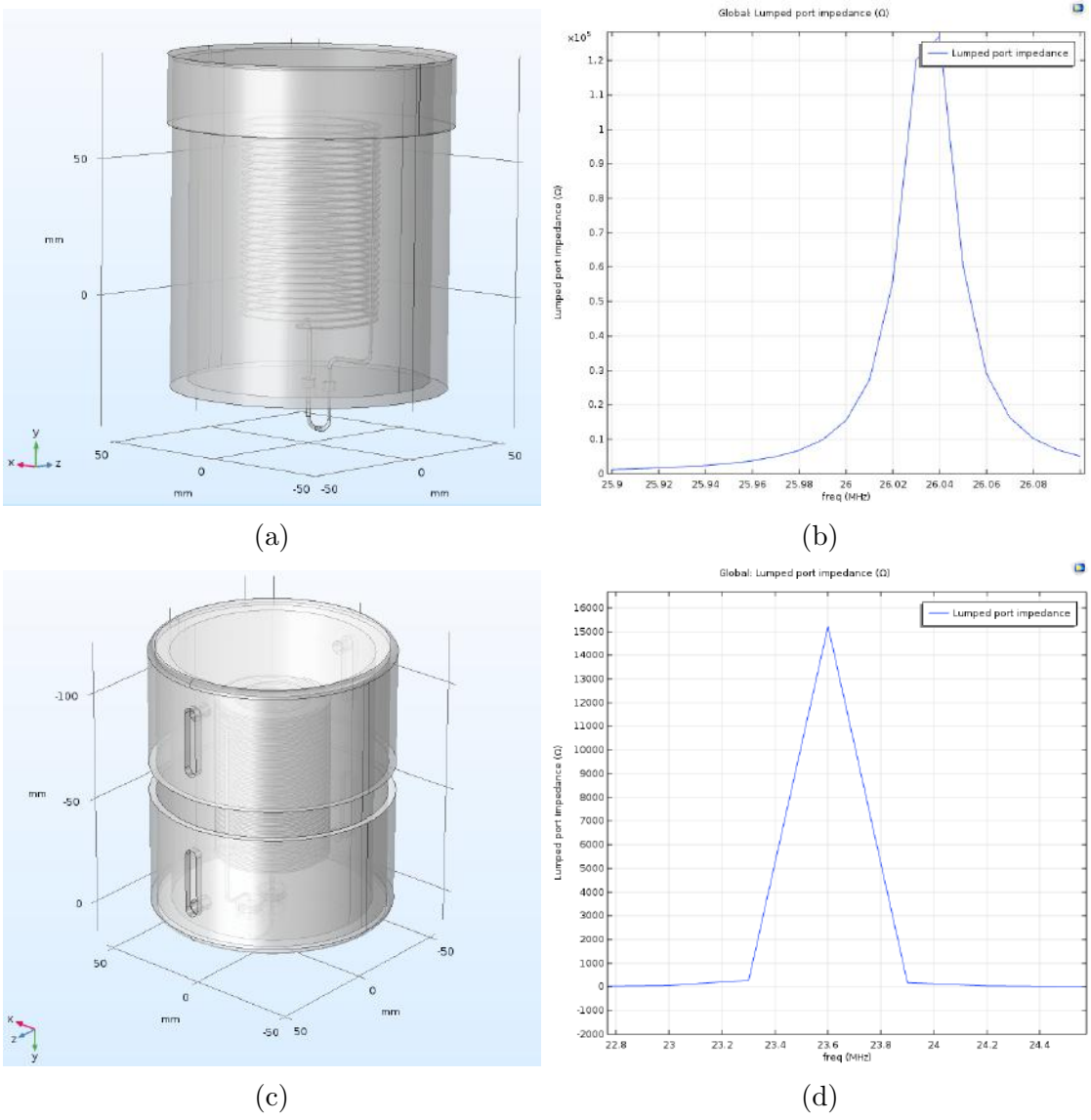

Figure 3.2: Simulations of resonant frequencies for the resonator with $N = 27$ in COMSOL. (a) Rough initial CAD model of the resonator (without PLA core). (b) Frequency scan of the simulations in COMSOL of the model in (a), impedance peaked at $\sim 26\,\text{MHz}$. (c) A more realistic CAD model of the resonator (with PLA core). (d) Frequency scan of the simulations in COMSOL of the model in (c), impedance peaked at $\sim 23.6\,\text{MHz}$.

To verify if these parameters for an unbalanced drive translates to a balanced drive

resonator, simulations using COMSOL are carried out. The geometry of the resonator is first drawn using Inventor, it is then imported into COMSOL and a simulation to determine the resonance frequency is carried out. The simulation is done following the guide provided by COMSOL in Ref. [35]. From the simulation results, a resonant frequency of 26 MHz is obtained, which is not far from the expected resonance of 20 MHz for an unbalanced drive resonator. It is noted that the simulations are done for an unloaded resonator. When connected to the trap, additional capacitance from the trap is expected to further reduce the resonance frequency.

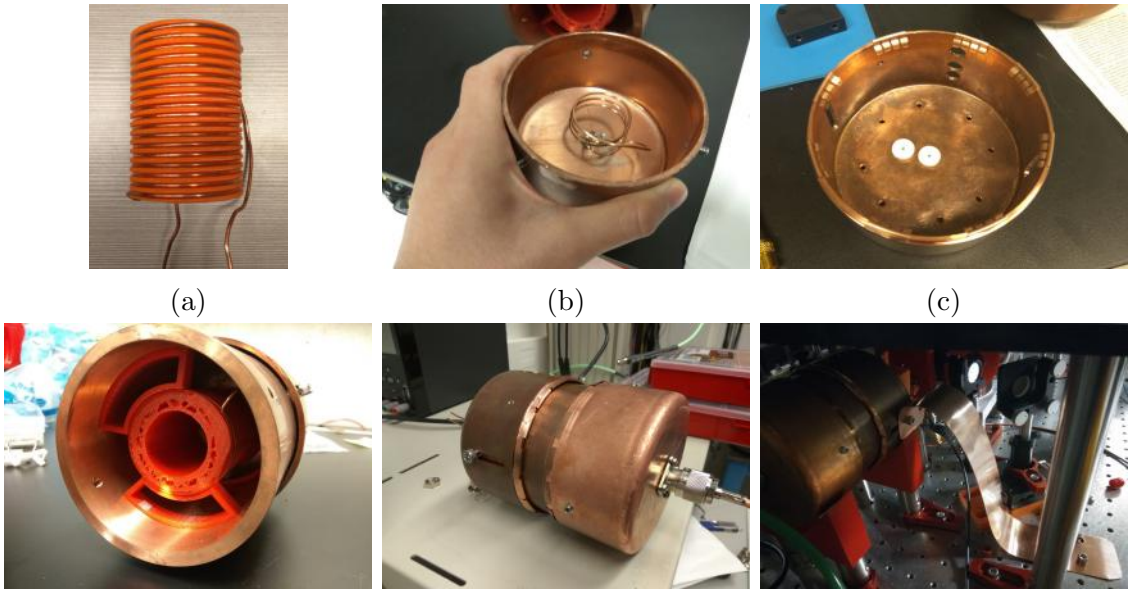

(a) (b) (c)

(d) (e) (f)

Figure 3.3: (a) An example of a core copper coil supported by a PLA plastic core with $N = 18$. (b) Top copper cap with antenna coil. (c) Bottom copper cap with fingerstocks and inserted PLA plastic as electrical insulators to allow the ends of the core copper coil to pass through. (d) Core copper coil supported by PLA plastic pieces inside the resonator. (e) Assembled resonator. (f) Bottom copper cap grounded to the optical table, which is grounded, with a copper tape.

With $d_0 = 1.628\,14$ mm and a small pitch of $\tau = 2.7$ mm, the copper coil is not rigid to stay in place and behaves like a flexible spring. To make a rigid coil, a polyactic acid (PLA) plastic piece with threading corresponding to $\tau = 2.7$ mm is 3D printed and the copper coil is wound around the plastic piece (see Figure 3.3a). The coil with the plastic core is

supported by more 3D printed plastic pieces within the copper cylinder (see Figure 3.3d). The resonant frequency is expected to be shifted due to additional capacitance introduced by the PLA plastic core, as the relative permittivity of PLA is around $\epsilon_r = 3$ in the MHz range[36]. COMSOL simulations with the plastic core taken into account give a decreased resonant frequency of 23.6 MHz as shown in Figure 3.2d. Plastic pieces are also 3D printed to electrically isolate the voltage output ends of the resonator coil from the copper cap as shown in Figure 3.3c. To match the resonator impedance to 50 Ω, Ref. [33] shows that this can be done by tuning the parameters of the antenna coil coupling to the main coil in the resonator. It is found that 3 turns of AWG 14 copper wire wound around a 1 inch Thorlabs lens tube is able to achieve good impedance matching (see Figure 3.3b). The pitch of the antenna coil is adjusted in an ad hoc manner until good impedance matching is achieved. Copper fingerstocks are fitted to the rims of the copper caps to ensure good electrical contact of the copper caps with the copper cylinder.

The unloaded resonator is tested with a vector network analyzer (VNA). The VNA sends a signal to the antenna coil, and it is set to measure the reflected signal back to the VNA. At resonance, the reflected signal is minimal. From the test, a resonance frequency of 21.7 MHz is measured. However, the resonance is found to decrease significantly to 11.5 MHz when connected to the four-rod trap. This is unexpected as the inductance of the main coil from COMSOL simulation is 12 μH. From a RLC circuit model, the relation of the resonant frequency to the inductance and capacitance is

$$\Omega_{RF} = \frac{1}{\sqrt{LC}} \tag{3.5}$$

where L is the inductance and C is the capacitance. Thus, to obtain a resonant frequency of 21.7 MHz, the internal capacitance of the resonator has to be $C = 4.5$ pF. In order to lower the resonant frequency to 11.5 MHz, assuming that the trap is mostly capacitive, the ion trap would have to add 11.5 pF of capacitance in parallel to the circuit. This is inconsistent with our COMSOL simulations as we predicted a trap capacitance of ~ 2.7 pF from the simulations. We did not have the suitable instruments directly to measure such a small capacitance for our trap, and thus we were unable to verify this source of discrepancy. This is an interesting question to be answered in future endeavors.

In order to move ahead with the laboratory build up, a trial and error method is approached. Since replacing the main coil in the resonator is easy, new geometric parameters for the coil corresponding to higher resonance frequencies are built and tested. After some trial and error, it is found that $N = 15$, $\tau = 4.87$ mm and $d_0 = 2.0525$ mm (corresponding to AWG 12 wire) gives a loaded resonant frequency of 21.635 MHz (38 MHz unloaded), which is sufficiently close to the desired RF frequency. The loaded Q-factor is measured

to be $Q = 296$ (see Figure 3.4a). By adjusting the position of the copper cap with the antenna coil, the reflected power can be optimized to $-40\,\mathrm{dB}$ as shown in Figure 3.4b, which indicates good impedance matching.

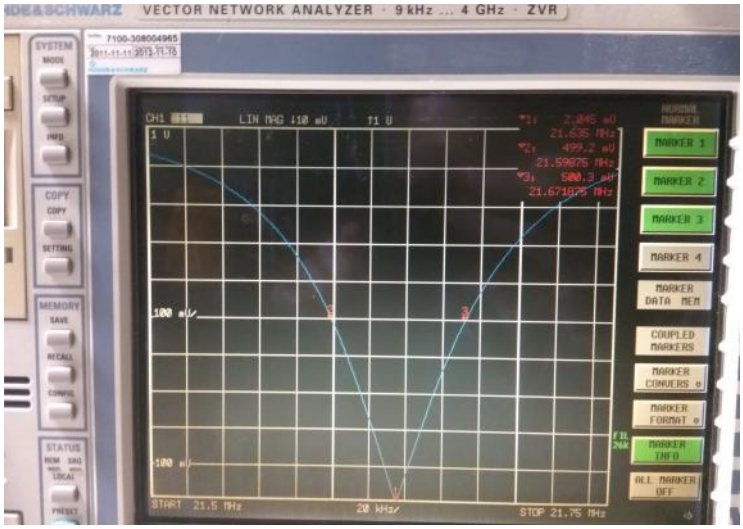

(a)

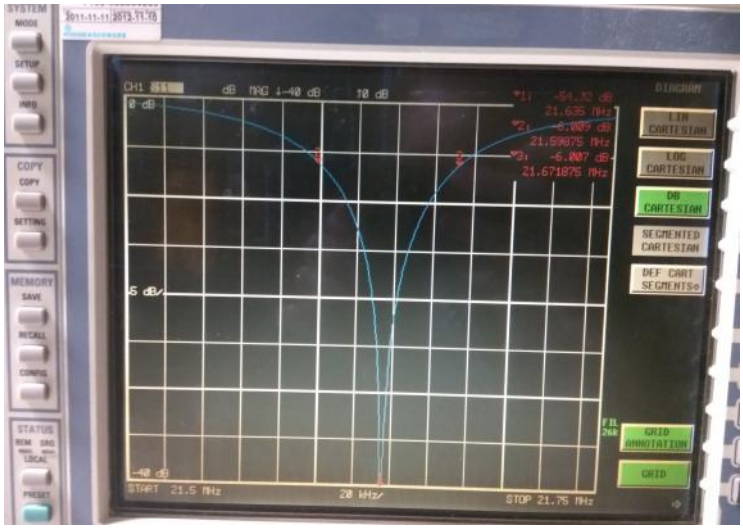

(b)

Figure 3.4: Measurement of reflected signal from the (loaded) resonator as a function of signal frequency using a VNA (Rohde & Schwarz 9 kHz - 4 GHz ZVR). (a) Plot of reflected signal against signal frequency in a linear scale. 3 markers are placed at the point of minimum reflectance and at the half-maximum points to obtain the values to compute the Q-factor. (b) Plot of reflected signal against signal frequency in logarithmic scale (or linear dB scale).

To calculate the required power, P, to be delivered to the resonator to achieve 200 V RF amplitude, the formula from Ref. [33] is followed

$$P = \frac{V_0^2}{2QL\Omega_{RF}} \tag{3.6}$$

where Q is the Q-factor of the resonator, L is the inductance of the system, V_0 and Ω_{RF} are as defined in Chapter 2. From COMSOL simulations, the inductance of the coil of the first resonator (with $N = 27$) is 12 μH. Although this value of inductance is not the one simulated for the resonator that we ultimately use, it should give a rough estimate of the same order of magnitude. With $V_0 = 200$ V, $Q = 296$, $\Omega_{RF} = 2\pi \times 21.635$ MHz and $L = 12\,\mu$H, a power of $P = 41.4$ mW, which corresponds to approximately 16 dBm of power.

For the complete set up to power the trap, an arbitrary waveform generator (Rigol DG4102) is used to generate an oscillating voltage at the desired frequency. It is then amplified by an amplifier (Mini-Circuits ZHL-5W-1+) with a 45 dB gain and a P1 level at 37 dBm, which means we have a lot of room to go above the estimated required power of 16 dBm if needed. The output from the RF amplifier is connected to a directional coupler (Mini-Circuits ZFBDC20-61HP+), where the transmitted port is connected to the resonator. The isolated port with -20 dB attenuation is connected to a spectrum analyzer (Keysight N9937A FieldFox Handheld Microwave Spectrum Analyzer) to monitor the reflected power from the resonator. The frequency of the signal generator is tuned to minimize the reflected power as picked up by the spectrum analyzer to ensure that it is at the resonant frequency of the RF system. It is found that the signal at the spectrum analyzer changes depending on if the device is powered by its own battery or from a power supply when the external parts of the resonator (copper cylinder and caps) are not grounded. Upon contacting the manufacturer of the spectrum analyzer, it is speculated to be a ground loop problem. The issue is solved when one of the copper caps of the resonator is grounded with a copper tape, as shown in Figure 3.3f. The resonance of the RF system is also found to drift in a time scale of hours when first powered on. The exact cause of this drift is unknown. To mitigate this problem, the RF system is always powered on to expedite ion trapping experiments.

3.2 DC Voltage Control Box

For the four-rod trap, 6 DC voltages are required; 2 high voltage sources for the needle electrodes, 4 relatively low voltage sources for the rods. A printed circuit board (PCB) is

custom designed for this purpose. A simplified schematic is shown in Figure 3.5. The full schematics can be found in Figure 3.6.

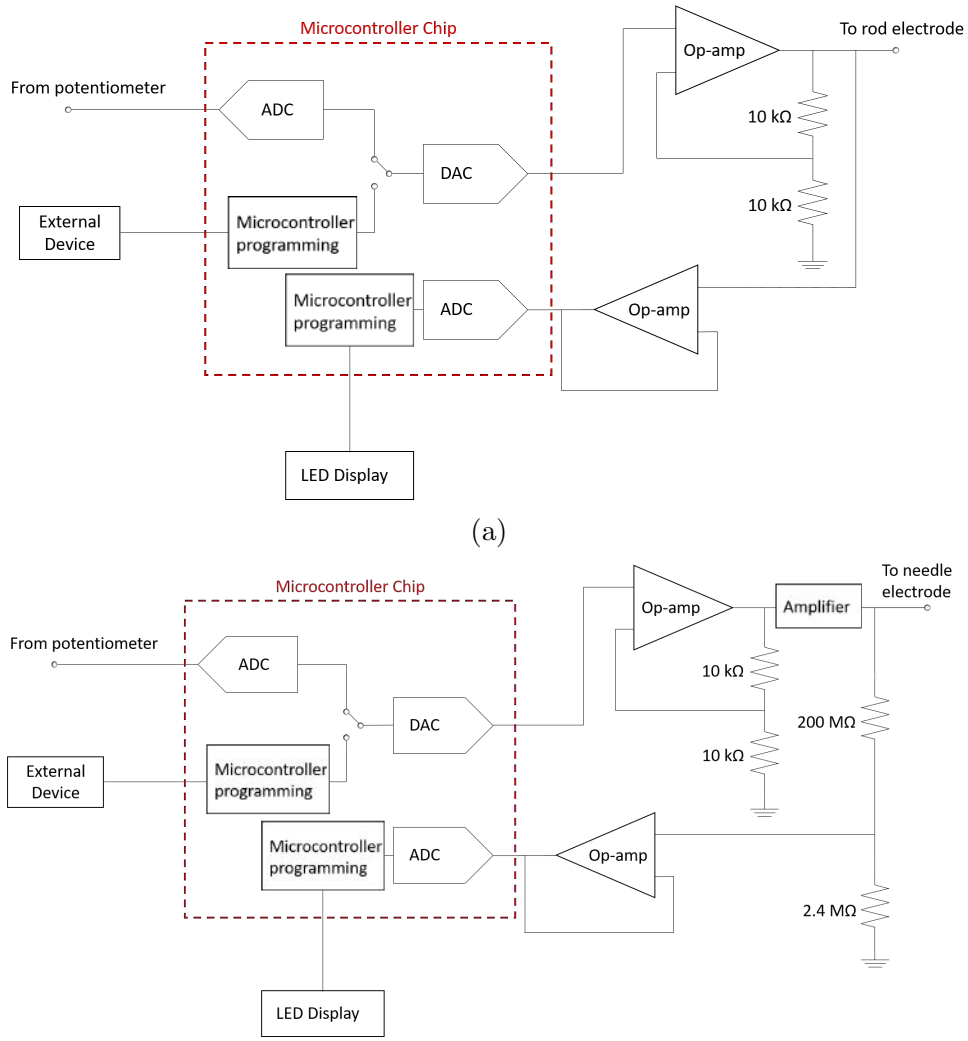

Figure 3.5: Simplified electrical schematics for the DC voltage sources for (a) rod electrodes and (b) needle electrodes.

A microcontroller chip (Atmel ATSAM4N16C) with built-in analog-to-digital converters (ADC) and digital-to-analog converter (DAC) is used for each electrode. The microcontroller chip is powered by 3.3 V and thus the range of the built-in ADC and DAC is

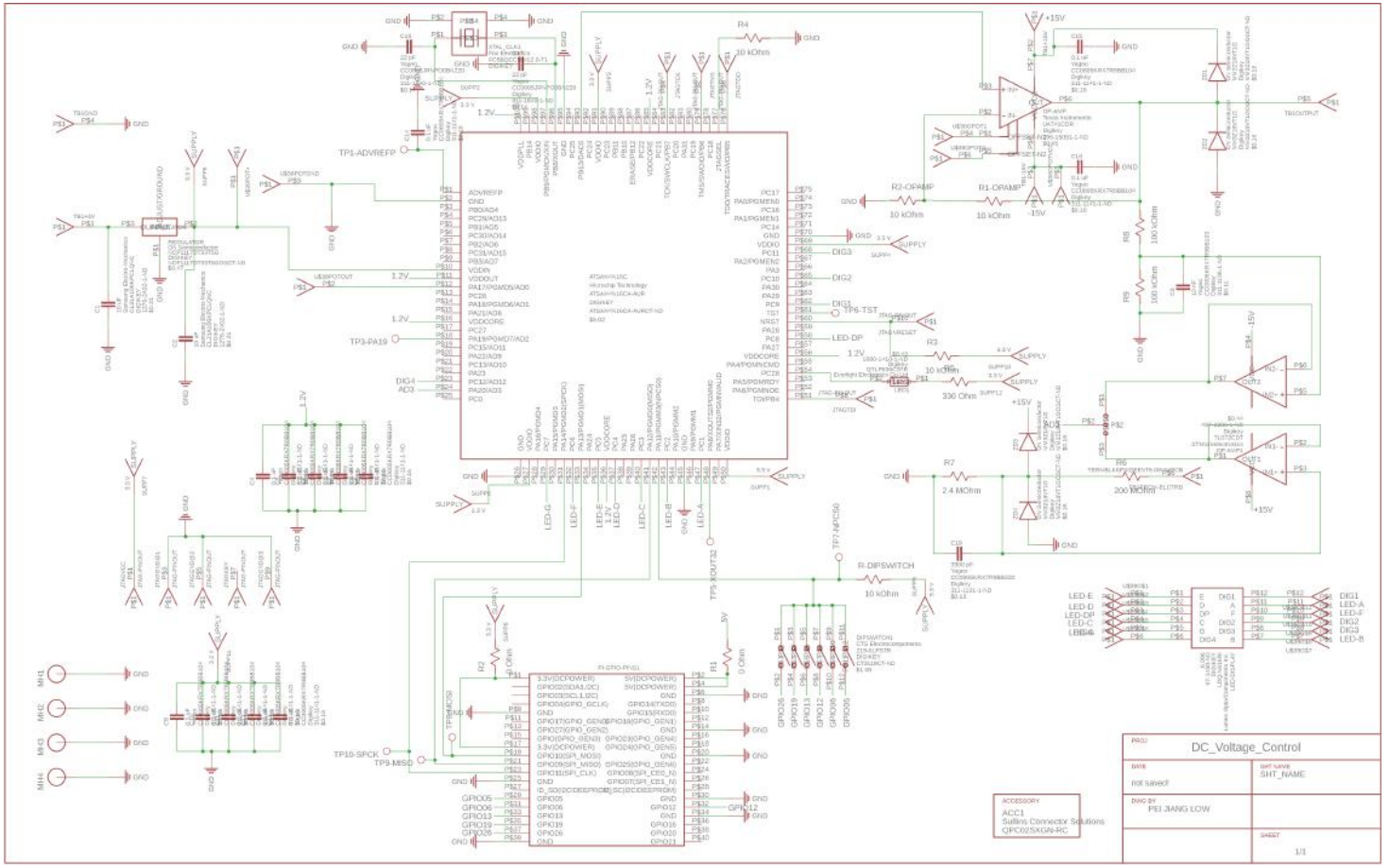

Figure 3.6: Complete schematics of a DC voltage control board.

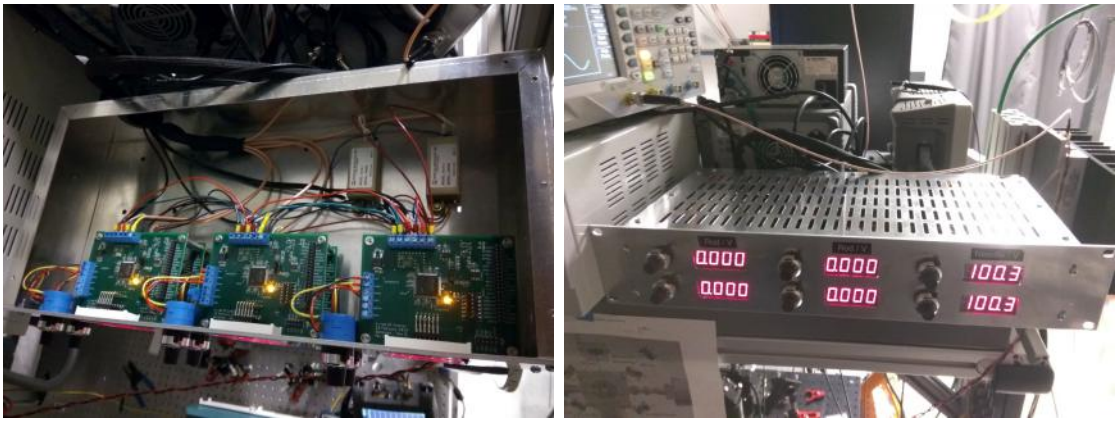

(a) (b)

Figure 3.7: (a) Inside the DC voltage control box, where the circuit boards are housed. (b) Photograph of DC voltage control box in operation.

$0 - 3.3\,\mathrm{V}$, with a resolution of 10 bits. A variable digital input is obtained from either converting the voltage from a potentiometer with built-in ADC or another external device (such as a Raspberry Pi computer). The digital signal is then converted to voltage with the built-in DAC in the chip. The output voltage from the DAC is directed to an operational amplifier (op-amp) for voltage amplification. A convenient amplification factor of 2 is chosen. Thus, the output voltage range from the ap-amp is $0 - 6.6\,\mathrm{V}$. The output voltage from the op-amp is then connected to a rod electrode. The output is also wired back to one of the ADC channels in the microcontroller chip after stepping down the voltage by a factor of 2 with a potential divider for readout. The microchip is programmed to display the output voltage at a LED display corresponding to the reading from the readout ADC. For the needle electrodes, we desire an output voltage that can go up to at least $250\,\mathrm{V}$ from the simulation results in Section 2.5. Thus, an external DC voltage amplifier (Analog Modules Model 521A-1) that takes an input from $0 - 5\,\mathrm{V}$ and amplifies it to $0 - 300\,\mathrm{V}$ is used to further amplify the output voltage of $0 - 6.6\,\mathrm{V}$ from the board. A larger step down is required before the voltage from the needle electrode can be read out by the built-in ADC. To achieve a compromise between the maximum-achievable voltage and voltage step-size resolution, we chose a step down factor of $\frac{2.4}{202.4}$, which allows the board to readout a maximum voltage of $\frac{3.3\times 202.4}{2.4} = 278.3\,\mathrm{V}$. An aluminium box is machined to house the 6 PCBs. The potentiometer for each PCB is equipped with a dial. 4 cables are made to power the components of the box: $+5\,\mathrm{V}$ source to power the microcontroller chip, $+15\,\mathrm{V}$ and $-15\,\mathrm{V}$ to power the operational amplifier, and an additional $+15\,\mathrm{V}$ source to power

the external amplifiers for the needles. 6 output cables corresponding to the output of each of the boards are made from coaxial cables to shield the DC lines from external RF noise.

It is found that the signal at the input ADC from the potentiometer is not stable to within 1 bit, which is ($\sim 3\,\mathrm{mV}$). Fluctuations in the input ADC subsequently causes unwanted fluctuations at the DAC and thus the output voltage as well. Therefore, an infinite impulse response (IIR) filter is programmed into the microcontroller chip as a long-pass filter for the input ADC to mitigate this problem. At the DAC, instead of converting the digital signal directly from the input ADC, a weighted average of past signals is used instead

$$y_n = (1 - a)x_n + ay_{n-1} \tag{3.7}$$

where y_n is the output signal to be converted by DAC, a is the filter parameter, x_n is the new reading from the input ADC, y_{n-1} is the output signal from the previous iteration. We used $a = 0.97$ and the fluctuations are no longer observed.

3.3 Connection to Trap

To connect the voltage sources to the trap electrodes, we designed and purchased a flexible printed circuit (FPC) made from a vacuum compatible material (Pyralux AP). Capacitors ($8.2\,\mathrm{nF}$) and resistors ($10\,\mathrm{M\Omega}$), which form bias tees for the rods, are soldered onto the FPC with vacuum compatible silver solder. It is found that the DC voltages are not sufficiently decoupled from the RF sources with only the bias tees on the FPC from initial tests with the trap. Firstly, the non-zero voltages on the rods changes when the RF source is turned on or off. The rod voltages are also found to have cross-talk when RF is turned on. This issue is resolved by making a stronger bias tee by attaching $1\,\mathrm{mH}$ inductors to the output cables of the DC voltage control PCBs for the rods. For good measures to isolate RF coupling to the needle electrodes, pi-filters (each with capacitance values of $5\,\mathrm{nF}$ and $10\,\mathrm{nF}$) are also attached to the cables for the needle electrodes. The issues have been resolved after these changes.

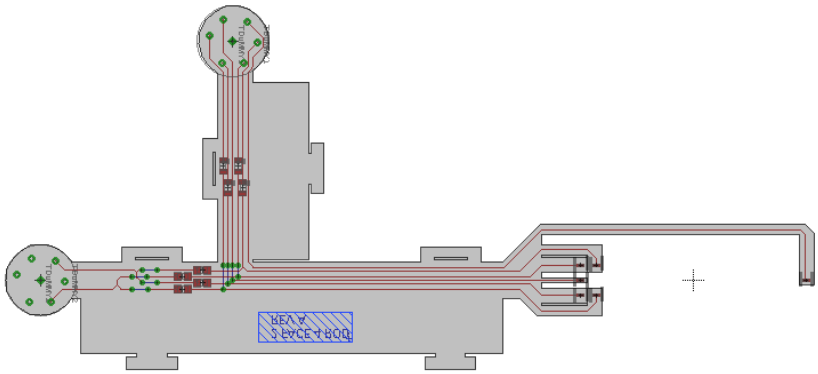

(a)

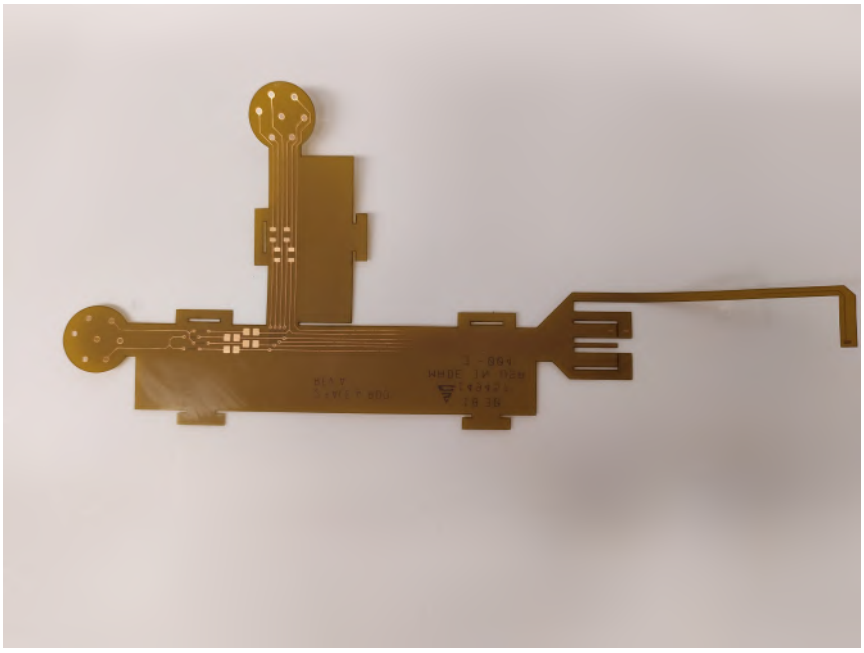

(b)

Figure 3.8: (a) Schematics for FPC. (b) Photograph of FPC.

With the trap voltage sources, we have managed to trap ions in our Paul trap.

Chapter 4

Imaging System

It is obvious that ions have to be imaged for trapped ion experiments. An imaging system is designed for this purpose. For our first trap, the four-rod trap, a conveniently available imaging objective from Thorlabs is chosen (LMU-5X-NUV). Although the numerical aperture (NA) is not great, $NA = 0.13$, it has a suitable working distance of 37.5 mm for our vacuum chamber. A spatial filter design is used to filter out background light not coming from the ions. A pair of plano-convex lenses with a focal length of $f = 100$ mm are used to construct a spatial filter system. The first lens focuses the collimated beam from the objective lens to an image plane, where a variable aperture (Thorlabs SM1D25) which can go down to an aperture diameter of 0.8 mm is placed to spatially filter background light. Another plano-convex lens is then used to recollimate the beam. The recollimated beam is then sent through an optical bandpass filter (FF01-488/10-25, 488/10 nm BrightLine single-band bandpass filter) in order to filter out unwanted wavelengths (not 493 nm from the ions). A motorized flip mirror is then used to choose to direct the collimated beam to either a photomultiplier tube (PMT) or a camera. A plano-convex lens of focal length $f = 125$ mm is then used to focus the beam to a camera/PMT to form a focused image. (see Figure 4.1a)

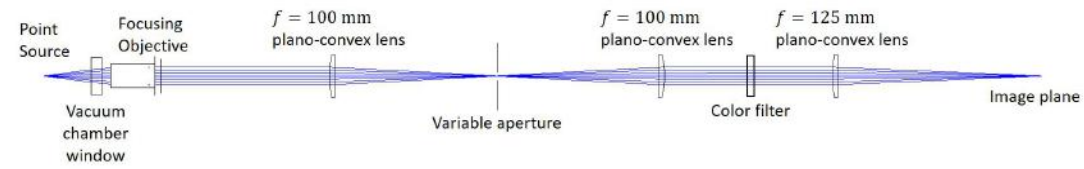

(a)

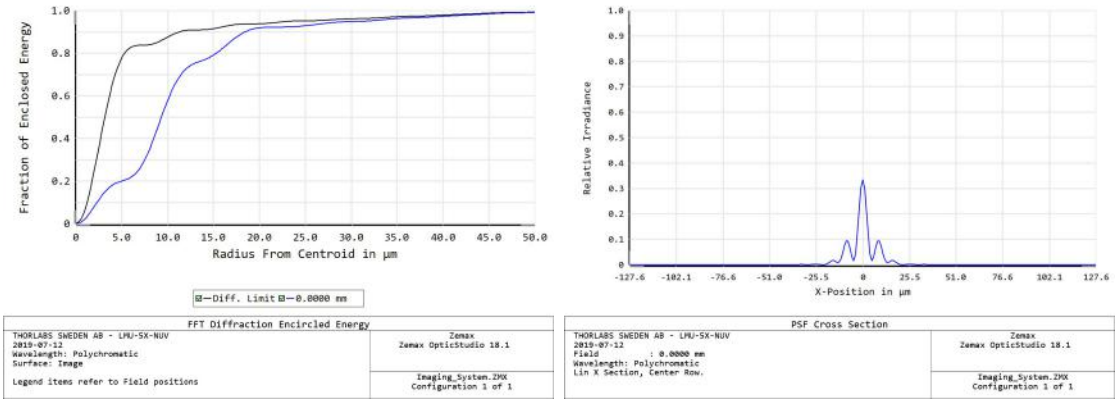

(b) (c)

Figure 4.1: (a) Schematic drawing of the relevant optical components for the imaging system. (b) Fraction of enclosed energy as a function of radius from centroid at the image plane. The black curve denotes the diffraction limit where no optical abberation is present. The blue curve is the data obtained from the simulations. (c) Point spread function (PSF) of a point source at the image plane.

Since the effective focal length of the objective is 40 mm, the magnification factor is $\frac{125}{40} = 3.125$. This magnification factor is chosen to strike a balance between sufficient magnification to resolve the distance between ions and enough photon counts per pixel on the camera for a good signal-to-noise ratio. The camera used for the imaging system (BFLY-PGE-05S2M-CS) has pixel sizes of 6 μm. From optical simulations using the Zemax software (see Figure 4.1b), 50% of the light is encircled within a diameter of approximately 18 μm at the image plane, which corresponds to 3 pixels across. Assuming that 50% of the collected photon counts are spread evenly to a square of 9 pixels, the photon count rate per pixel, W, is

$$W = \frac{1}{18} R_{SE,493} \left(\frac{1}{2} \left(1 - \sqrt{1 - NA^2} \right) \right) QE \tag{4.1}$$

where $R_{SE,493}$ is the scattering rate of the ion emitting photons of wavelength 493 nm, $\frac{1}{2}\left(1 - \sqrt{1 - NA^2}\right)$ is the portion of light collected from a point source for a given NA,

QE is the quantum efficiency of the camera, which is approximately 75% for the camera at hand. From calculations based on Ref. [37] done by an undergraduate student in the team, Nigel Andersen, $R_{SE,493} \approx 2.2\,\text{MHz}$. This gives $W = 0.53\,\text{photons/ms}$. To get above the Absolute Sensitivity Threshold of 13.19 of the camera, which is defined as the number of photons required to have signal equal to noise [38], at least 26 ms of integration time should be used. It is noted that this is a conservative estimate as the assumption that the photons are spread evenly across all 9 pixels is generally not true - a typical point spread function of a focused beam has a peak intensity at the centre and thus the centre pixel of the 9 would be brighter than the rest(see Figure 4.1c).

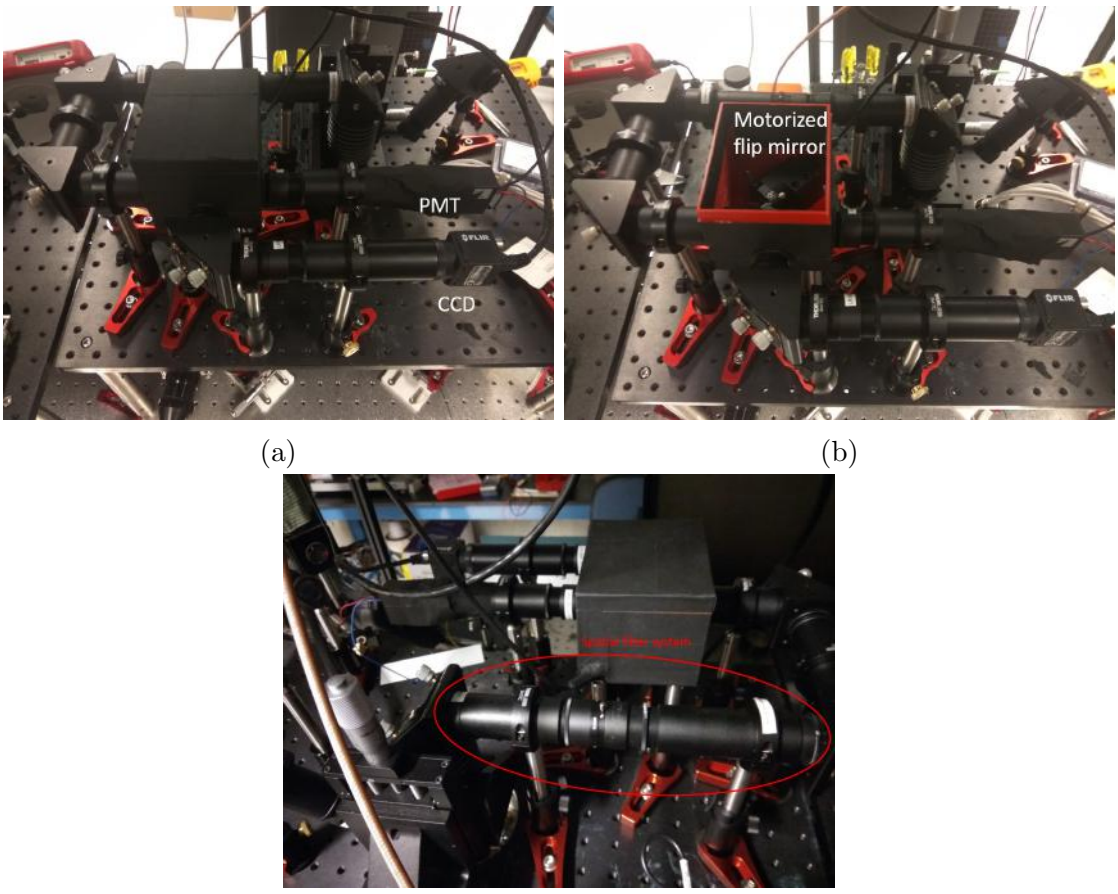

(a) (b)

(c)

Figure 4.2: (a) Complete setup of the imaging system. (b) Motorized flip mirror mounted in a 3D-printed box. (c) Spatial filter system in a Thorlabs lens tube setup.

To isolate the imaging system as best as possible from background light, the setup is built using lens tube system from Thorlabs. The motorized flip mirror is housed in a 3D-printed box, which is covered with black masking tapes from Thorlabs (T743-2.0) to ensure good opacity. The complete system is shown in Figure 4.2a. By testing the imaging system with a Thorlabs 1951 USAF resolution test target, we can still barely distinguish the smallest line spacing visually, which is approximately 4.4 μm apart(see Figure 4.3a. With this imaging system, we have managed to image barium ions that are approximately 7 μm apart as seen in Figure 4.3b.

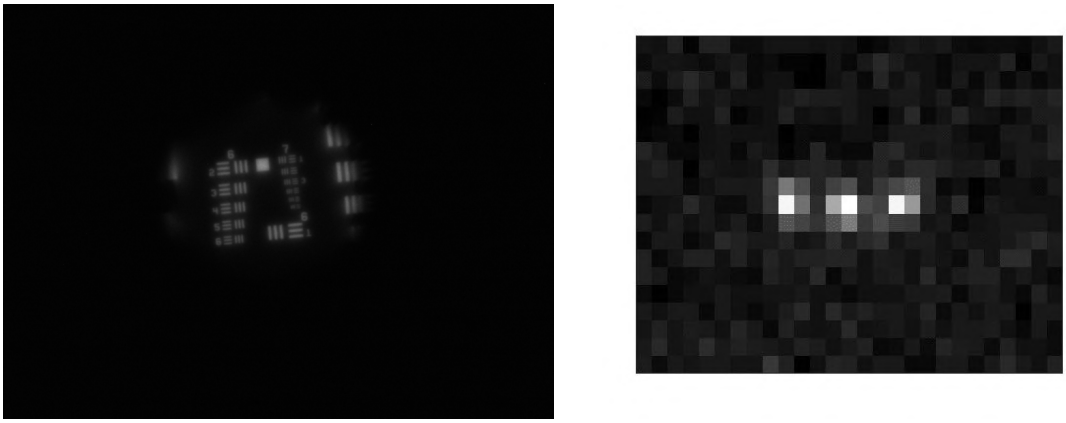

(a) (b)

Figure 4.3: (a) Image of Thorlabs 1951 USAF resolution test target obtained with the imaging system. (b) Image of 3 trapped barium ions in our four-rod trap, spaced $\sim 7\,\mu$m apart. Each pixel corresponds to a size of 1.92 μm. An exposure time of 0.5 s is used.

Chapter 5

Single Qudit Gate

As elucidated in Chapter 1, quantum computing with qudits provides access to a larger Hilbert space, which grants computational advantages over qubit computing in theory [2, 3, 4]. To realize qudit-based quantum computing, it is obvious that protocols for implementing qudit gates have to be developed. In this chapter, a method to implement a set of single qudit gates which forms a universal single qudit gate set is presented. The known sources of error for single qudit gates are also discussed. The practicality of realizing single qudit gates with trapped $^{137}Ba^{+}$ ion is then assessed by quantifying the expected errors from the error sources. This chapter and Chapter 6 are part of the work contributing to the paper that our group worked on [39].

5.1 Single Qudit Gate Decomposition

It has been shown that any single qudit unitary can be decomposed into a sequence of two-level transitions as long as the available transitions form a connected graph of the encoded states [40].

$$\hat{U} = \hat{V}_K \hat{V}_{K-1} \dots \hat{V}_1 \tag{5.1}$$

where $\hat{V}_i$ is the unitary operator generated by the i^{th} two-level transition between some state $|l\rangle$ and $|l+1\rangle$, which is of the form

$$\hat{V} = \exp\left(i\theta\left(e^{i\phi}|l+1\rangle\langle l| + e^{-i\phi}|l\rangle\langle l+1|\right)\right) \tag{5.2}$$

where θ is the gate phase which physically depends on the Rabi frequency and gate time applied to the transition, ϕ is the spin phase which physically depends on the phase of the

perturbation driving the transition. It is shown in Ref. [40] that at most $\frac{d(d-1)}{2}$ transitions are required to decompose an arbitrary d-dimensional qudit unitary to a diagonal matrix, and an additional $2d-1$ transitions at most to fully decompose the unitary. In this thesis, focus is given to prime dimensional qudits, and qudit gates pertaining to 3 and 5-level qudits are constructed. With this decomposition technique, the transition sequences for the generalized version of Pauli operators and $\pi/8$ gate, which form the universal gate set for qudits [41], are formulated. In addition, quantum Fourier transform (QFT) for qudits is also formulated. The generalized Pauli x, y and z operators are denoted as $\hat{X}$, $\hat{Y}$ and $\hat{Z}$ respectively. They are defined as follows: $\hat{X}|l\rangle = |l+1 \bmod d\rangle$, $\hat{Z}|l\rangle = e^{i\frac{2\pi l}{d}}|l\rangle$, $\hat{Y} = i\hat{X}\hat{Z}$. The generalized $\pi/8$ gate is denoted as $\hat{T}$. Following Ref. [41], the definition of $\hat{T}$ for $d = 3$ is

$$\hat{T} = \begin{pmatrix} 1 & 0 & 0 \\ 0 & e^{i\frac{2\pi}{9}} & 0 \\ 0 & 0 & e^{-i\frac{2\pi}{9}} \end{pmatrix} \tag{5.3}$$

For $d = 5$, $\hat{T}$ is

$$\hat{T} = \begin{pmatrix} 1 & 0 & 0 & 0 & 0 \\ 0 & e^{-i\frac{4\pi}{5}} & 0 & 0 & 0 \\ 0 & 0 & e^{-i\frac{2\pi}{5}} & 0 & 0 \\ 0 & 0 & 0 & e^{i\frac{4\pi}{5}} & 0 \\ 0 & 0 & 0 & 0 & e^{i\frac{2\pi}{5}} \end{pmatrix} \tag{5.4}$$

The quantum Fourier transform gate is denoted as $Q\hat{F}T$. QFT acting on a single qudit is defined as $Q\hat{F}T|j\rangle = \frac{1}{\sqrt{d}}\sum_l e^{i\frac{2\pi kl}{d}}|l\rangle$. The two-level transition sequences with the gate and spin phases required to construct these gates are documented in Tables 5.1 and 5.2.

Unitary	Pulse	Transition	Gate phase, θ	Spin phase, ϕ
$\hat{X}$	1	$\|0\rangle \leftrightarrow \|1\rangle$	π	0
	2	$\|1\rangle \leftrightarrow \|2\rangle$	$\pi/2$	$\pi/2$
	3	$\|0\rangle \leftrightarrow \|1\rangle$	$\pi/2$	$\pi/2$
$\hat{Y}$	1	$\|0\rangle \leftrightarrow \|1\rangle$	$\pi/2$	$\pi/2$
	2	$\|0\rangle \leftrightarrow \|1\rangle$	$\pi/2$	$7\pi/6$
	3	$\|1\rangle \leftrightarrow \|2\rangle$	$\pi/2$	$\pi/2$
	4	$\|0\rangle \leftrightarrow \|1\rangle$	$\pi/2$	$\pi/2$
$\hat{Z}$	1	$\|1\rangle \leftrightarrow \|2\rangle$	$\pi/2$	$\pi/2$
	2	$\|1\rangle \leftrightarrow \|2\rangle$	$\pi/2$	$\pi/6$
$Q\hat{F}T$	1	$\|0\rangle \leftrightarrow \|1\rangle$	$\pi/2$	$\pi/2$
	2	$\|0\rangle \leftrightarrow \|1\rangle$	$\pi/2$	$3\pi/2$
	3	$\|0\rangle \leftrightarrow \|1\rangle$	$\pi/4$	$5\pi/6$
	4	$\|1\rangle \leftrightarrow \|2\rangle$	$\pi/2$	$\pi/2$
	5	$\|1\rangle \leftrightarrow \|2\rangle$	$\pi/2$	$2\pi/3$
	6	$\|1\rangle \leftrightarrow \|2\rangle$	$\arctan\sqrt{2}$	$7\pi/6$
	7	$\|0\rangle \leftrightarrow \|1\rangle$	$\pi/4$	$7\pi/6$
$\hat{T}$	1	$\|1\rangle \leftrightarrow \|2\rangle$	$\pi/2$	$\pi/2$
	2	$\|1\rangle \leftrightarrow \|2\rangle$	$\pi/2$	$31\pi/18$

Table 5.1: Unitary decomposition for various 3-dimensional unitary gates of interest.

Unitary	Pulse	Transition	Gate phase, θ	Phase, ϕ
$\hat{X}$	1	$\|0\rangle \leftrightarrow \|1\rangle$	π	0
	2	$\|2\rangle \leftrightarrow \|3\rangle$	π	0
	3	$\|3\rangle \leftrightarrow \|4\rangle$	$\pi/2$	$\pi/2$
	4	$\|2\rangle \leftrightarrow \|3\rangle$	$\pi/2$	$\pi/2$
	5	$\|1\rangle \leftrightarrow \|2\rangle$	$\pi/2$	$\pi/2$
	6	$\|0\rangle \leftrightarrow \|1\rangle$	$\pi/2$	$\pi/2$
$\hat{Y}$	1	$\|0\rangle \leftrightarrow \|1\rangle$	$\pi/2$	$\pi/2$
	2	$\|0\rangle \leftrightarrow \|1\rangle$	$\pi/2$	$9\pi/10$
	3	$\|1\rangle \leftrightarrow \|2\rangle$	$\pi/2$	$\pi/2$
	4	$\|1\rangle \leftrightarrow \|2\rangle$	$\pi/2$	$7\pi/10$
	5	$\|2\rangle \leftrightarrow \|3\rangle$	$\pi/2$	$\pi/2$
	6	$\|2\rangle \leftrightarrow \|3\rangle$	$\pi/2$	$9\pi/10$
	7	$\|3\rangle \leftrightarrow \|4\rangle$	$\pi/2$	$\pi/2$
	8	$\|2\rangle \leftrightarrow \|3\rangle$	$\pi/2$	$\pi/2$

	9	$\|1\rangle \leftrightarrow \|2\rangle$	$\pi/2$	$\pi/2$
	10	$\|0\rangle \leftrightarrow \|1\rangle$	$\pi/2$	$\pi/2$
$\hat{Z}$	1	$\|1\rangle \leftrightarrow \|2\rangle$	$\pi/2$	$\pi/2$
	2	$\|1\rangle \leftrightarrow \|2\rangle$	$\pi/2$	$19\pi/10$
	3	$\|2\rangle \leftrightarrow \|3\rangle$	$\pi/2$	$\pi/2$
	4	$\|2\rangle \leftrightarrow \|3\rangle$	$\pi/2$	$7\pi/10$
	5	$\|3\rangle \leftrightarrow \|4\rangle$	$\pi/2$	$\pi/2$
	6	$\|3\rangle \leftrightarrow \|4\rangle$	$\pi/2$	$19\pi/10$
$Q\hat{F}T$	1	$\|0\rangle \leftrightarrow \|1\rangle$	$\pi/2$	$\pi/2$
	2	$\|0\rangle \leftrightarrow \|1\rangle$	$\pi/2$	3.30265
	3	$\|0\rangle \leftrightarrow \|1\rangle$	$\pi/4$	0.63627
	4	$\|1\rangle \leftrightarrow \|2\rangle$	$\pi/2$	$\pi/2$
	5	$\|1\rangle \leftrightarrow \|2\rangle$	$\pi/2$	6.18626
	6	$\|1\rangle \leftrightarrow \|2\rangle$	0.95532	1.53005
	7	$\|0\rangle \leftrightarrow \|1\rangle$	0.60641	4.57966
	8	$\|2\rangle \leftrightarrow \|3\rangle$	$\pi/2$	$\pi/2$
	9	$\|2\rangle \leftrightarrow \|3\rangle$	$\pi/2$	$\pi/2$
	10	$\|2\rangle \leftrightarrow \|3\rangle$	$\pi/3$	1.981884
	11	$\|1\rangle \leftrightarrow \|2\rangle$	0.85289	3.74954
	12	$\|0\rangle \leftrightarrow \|1\rangle$	0.60641	3.69336
	13	$\|3\rangle \leftrightarrow \|4\rangle$	$\pi/2$	$\pi/2$
	14	$\|3\rangle \leftrightarrow \|4\rangle$	$\pi/2$	$9\pi/10$
	15	$\|3\rangle \leftrightarrow \|4\rangle$	1.10714	$9\pi/10$
	16	$\|2\rangle \leftrightarrow \|3\rangle$	$\pi/3$	$9\pi/10$
	17	$\|1\rangle \leftrightarrow \|2\rangle$	0.95532	$9\pi/10$
	18	$\|0\rangle \leftrightarrow \|1\rangle$	$\pi/4$	$9\pi/10$
$\hat{T}$	1	$\|1\rangle \leftrightarrow \|2\rangle$	$\pi/2$	$\pi/2$
	2	$\|1\rangle \leftrightarrow \|2\rangle$	$\pi/2$	$7\pi/10$
	3	$\|2\rangle \leftrightarrow \|3\rangle$	$\pi/2$	$\pi/2$
	4	$\|2\rangle \leftrightarrow \|3\rangle$	$\pi/2$	$3\pi/10$
	5	$\|3\rangle \leftrightarrow \|4\rangle$	$\pi/2$	$\pi/2$
	6	$\|3\rangle \leftrightarrow \|4\rangle$	$\pi/2$	$11\pi/10$

Table 5.2: Unitary decomposition for various five dimensional unitary gates of interest. The Quantum Fourier Transform was found numerically.

5.2 Practical Realization of Single Qudit Gate and Error Sources

For trapped ions with computational states encoded in hyperfine energy states, two-level transitions are typically driven directly with microwaves or through Raman transitions using laser beams within or close-to the visible spectrum. This is the case for the ion species in our considerations, which is $^{137}Ba^{+}$. To encode multiple qudit states in $6S_{1/2}$ hyperfine levels of $^{137}Ba^{+}$, a magnetic field is applied to break the degeneracy in each hyperfine level with Zeeman splitting. This gives 8 non-degenerate energy states. Figure 5.1 shows encoding schemes for 3 and 5-level $^{137}Ba^{+}$ qudits. The hyperfine energy splitting for $F = 1$ and $F = 2$ is approximately 8 GHz [42]. Assuming a magnetic field of 0.47 mT is applied, the Zeeman splitting is $\Delta_z = 3.29$ MHz. For the subsequent sections on error calculations and also in Chapter 6, the aforementioned encoding schemes and parameters are assumed.

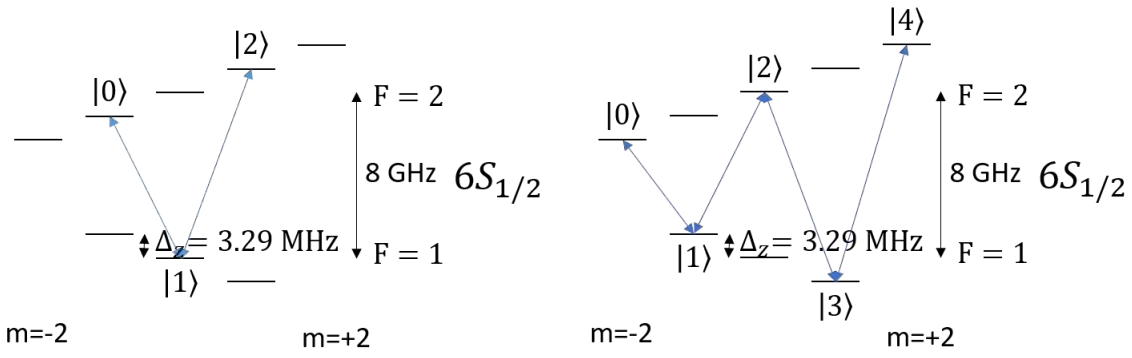

Figure 5.1: Encoding schemes of qudit states in $^{137}Ba^{+}$ for (a) 3-level qudit and (b) 5-level qudit. The blue arrows indicate 2-level transitions which form a connected graph of all the qudit states.

In order to assess the practicality of a trapped ion qudit system, the expected errors for the constructed gate set should be evaluated. The errors under considerations for the single qudit gates are

1. Magnetic field noise.
2. Off-resonant coupling.
3. Photon scattering.

Other error sources pertaining to hardware control imperfections are excluded as they can arguably be improved as technology advances, thus not posing a fundamental limit to the fidelities of the single qudit gates.

5.2.1 Magnetic Field Noise

Magnetic field is applied to a trapped ion quantum computing system in order to establish an angular momentum axis and to break the degeneracy of the hyperfine levels of an ion. Fluctuations in the magnetic field introduces decoherence to a qudit state, and introduces errors into the single qudit gates. With a magnetic field deviation of ΔB, The Hamiltonian when a single qudit gate is applied is

$$\hat{H} = \hat{H}_{ideal} + \hat{H}_{noise} \tag{5.5}$$

where $\hat{H}_{ideal}$ is the ideal Hamiltonian for the single qudit gate and

$$\hat{H}_{noise} = \sum_k \mu_B g_{F,k} m_k \Delta B |k\rangle\langle k| \tag{5.6}$$

where μ_B is the Bohr magneton, $g_{F,k}$ is the hyperfine g-factor, m_k is the projection of the angular momentum along the direction of the magnetic field. The subscript k denote the energy state $|k\rangle$, which may or may not be an encoded state. $^{137}Ba^+$ has a nuclear spin of $I = \frac{3}{2}$. Thus, the hyperfine g-factor in the $6S_{1/2}$ state is $g_F = -\frac{1}{2}$ for $F = 1$ and $g_F = \frac{1}{2}$ for $F = 2$ [43]. The magnetic field noise, $\Delta B(t)$, can be modelled as a stationary Gaussian process with an exponentially decreasing correlation with an inverse correlation time of γ [44]:

$$\langle \Delta B(0) \Delta B(t) \rangle = \langle \Delta B^2 \rangle e^{-\gamma t} \tag{5.7}$$

To quantify the error due to magnetic field noise, the time-evolution of a quantum state under the Hamiltonian in the presence of noise is obtained by numerically solving Schrödinger's equation

$$\frac{d}{dt}|\psi\rangle = -i\hat{H}|\psi\rangle \tag{5.8}$$

The output state obtained is then compared with the ideal output state to compute the gate fidelity

$$F = |\langle\psi_{ideal}|\psi(t_{gate})\rangle|^2 \tag{5.9}$$

where $|\psi_{ideal}\rangle$ is the ideal output state, t_{gate} is the gate time and $|\psi(t_{gate})\rangle$ is the output state at the end of the gate time. The deviation from the perfect fidelity of $F = 1$ is defined as the error. From Ref. [45], magnetic field fluctuations of $\sqrt{\langle\Delta B^2\rangle} = 2.7\,\mathrm{pT}$ is achievable in experiments, which will be the figure used for the error calculations in this thesis.

5.2.2 Off Resonant Coupling

When a perturbation is applied to drive a two-level transition, other states off-resonant to the applied perturbation can be driven with small amplitudes too, provided that these off-resonant transitions are allowed by selection rules. This can be largely mitigated by having a polarized perturbation so that off-resonant transitions are forbidden by selection rules. However, polarization control is hard to come by from commonly available microwave sources. In contrast, it is easy to implement polarization control for Raman beams with optical waveplates and off-resonant coupling can be avoided. Thus, this error is more relevant to the case where transitions are driven with microwave sources.

When off-resonant coupling is present, the Hamiltonian for the system is

$$\hat{H} = \hat{H}_{ideal} + \hat{H}_{OR} \tag{5.10}$$

where $\hat{H}_{OR}$ is the component of the Hamiltonian due to off-resonant coupling. It has the form

$$\begin{aligned}\hat{H}_{OR} &= -\frac{\Omega_l}{2}\left[|l\rangle\langle l+1| + |l+1\rangle\langle l|\right] \\ &\quad + \sum_k \sum_{k'\neq k} \frac{\Omega_{k,k'}}{2} \exp\left(i\left(\omega_k - \omega_{k'}\right)t - i\,\mathrm{sgn}\left(\omega_k - \omega_{k'}\right)\omega_l t\right)|k\rangle\langle k'| \\ &= -\hat{H}_{ideal} + \sum_k \sum_{k'\neq k} \frac{\Omega_{k,k'}}{2} \exp\left(i\left(\omega_k - \omega_{k'}\right)t - i\,\mathrm{sgn}\left(\omega_k - \omega_{k'}\right)\omega_l t\right)|k\rangle\langle k'|\end{aligned} \tag{5.11}$$

where $|l\rangle$ and $|l+1\rangle$ are the encoded states where resonant transition is desired, Ω_l is the Rabi frequency for the desired transition, ω_l is the transition frequency between $|l\rangle$ and

$|l+1\rangle$, $\Omega_{k,k'}$ is the Rabi frequency for the transition between the states $|k\rangle$ and $|k'\rangle$, $\hbar\omega_k$ is the energy for the $|k\rangle$ state, $\mathrm{sgn}\,(x)$ is the sign function

$$\mathrm{sgn}\,(x) = \begin{cases} -1 & \text{if } x < 0 \\ 0 & \text{if } x = 0 \\ 1 & \text{if } x > 0 \end{cases} \tag{5.12}$$

Numerical simulations is performed to obtain the output state from this Hamiltonian assuming an unpolarized source with equal magnitude for each polarization. The error due to off-resonant coupling is then quantified from the output state fidelity.

5.2.3 Photon Scattering

An error that is intrinsically present when optical Raman transitions are used is the error due to spontaneous emission, or photon scattering. This error is only relevant to transition with Raman beams as it stems from off-resonantly populating an excited $6P$ state. A spontaneous emission event can decohere a quantum state. Different types of scattering events is also found to introduce different extents of decoherence [46]. In this study, for simplicity and as an upper estimate of the error from photon scattering, any scattering event is assumed to completely decohere the quantum system. The total spontaneous emission rate is given by [47]

$$R_{SE} = \sum_i \gamma_i P_i \tag{5.13}$$

where γ_n is the decay rate in the excited state $|i\rangle$ and P_i is the probability that the $|i\rangle$ state is populated. For barium ions, the $|i\rangle$ states are the $6P_{1/2}$ and $6P_{3/2}$ states. For the 3-level system with the encoding scheme as shown in Figure 5.1a, the scattering rate for a

qudit in state $|l\rangle$ can be derived to be (see Appendix B)

$$
\begin{aligned}
R_{SE,0} &= \frac{|\langle 6P, L=1||\hat{d}||6S, L=0\rangle|^2}{4\hbar^2} \\
&\times \Big[\frac{\gamma_{1/2}}{\Delta_{1/2}^2}\Big(\frac{1}{6}\sum_j (r_{-,j}\xi_{r,j})^2 + \frac{1}{2}\sum_l (r_{+,l}\xi_{r,l})^2 + \frac{1}{3}\sum_k (b_{0,k}\xi_{b,k})^2\Big) \\
&+ \frac{\gamma_{3/2}}{\Delta_{3/2}^2}\Big(\frac{5}{6}\sum_j (r_{-,j}\xi_{r,j})^2 + \frac{1}{2}\sum_l (r_{+,l}\xi_{r,l})^2 + \frac{2}{3}\sum_k (b_{0,k}\xi_{b,k})^2\Big)\Big] \\
R_{SE,1} &= \frac{|\langle 6P, L=1||\hat{d}||6S, L=0\rangle|^2}{4\hbar^2} \\
&\times \Big[\frac{\gamma_{1/2}}{\Delta_{1/2}^2}\Big(\frac{1}{3}\sum_j (r_{+,j}\xi_{r,j})^2 + \frac{1}{3}\sum_l (r_{-,l}\xi_{r,l})^2 + \frac{1}{3}\sum_k (b_{0,k}\xi_{b,k})^2\Big) \\
&+ \frac{\gamma_{3/2}}{\Delta_{3/2}^2}\Big(\frac{2}{3}\sum_j (r_{+,j}\xi_{r,j})^2 + \frac{2}{3}\sum_l (r_{-,l}\xi_{r,l})^2 + \frac{2}{3}\sum_k (b_{0,k}\xi_{b,k})^2\Big)\Big] \\
R_{SE,2} &= \frac{|\langle 6P, L=1||\hat{d}||6S, L=0\rangle|^2}{4\hbar^2} \\
&\times \Big[\frac{\gamma_{1/2}}{\Delta_{1/2}^2}\Big(\frac{1}{2}\sum_j (r_{-,j}\xi_{r,j})^2 + \frac{1}{6}\sum_l (r_{+,l}\xi_{r,l})^2 + \frac{1}{3}\sum_k (b_{0,k}\xi_{b,k})^2\Big) \\
&+ \frac{\gamma_{3/2}}{\Delta_{3/2}^2}\Big(\frac{1}{2}\sum_j (r_{-,j}\xi_{r,j})^2 + \frac{5}{6}\sum_l (r_{+,l}\xi_{r,l})^2 + \frac{2}{3}\sum_k (b_{0,k}\xi_{b,k})^2\Big)\Big]
\end{aligned}
\tag{5.14}
$$

where $\Delta_{1/2}$ and $\Delta_{3/2}$ are the laser detuning frequencies of the Raman beams from the $6P_{1/2}$ and $6P_{3/2}$ levels respectively, $\gamma_{1/2} = 1.263 \times 10^8\,\mathrm{s}^{-1}$ is the decay rate from the $6P_{1/2}$ state, $\gamma_{3/2} = 1.582 \times 10^8\,\mathrm{s}^{-1}$ is the decay rate from the $6P_{3/2}$ state [48], $\langle 6P, L=1||\hat{d}||6S, L=0\rangle$ is the reduced dipole transition matrix element in terms of the orbital angular momentum L, ξ_r and ξ_b are the electric field amplitudes of the red and blue Raman beams respectively, r_i and b_i are the components of the red and blue electric fields of the Raman beams polarized in the i direction respectively, i.e.

$$
\begin{aligned}
\vec{\xi_r} &= \xi_r\,(r_+\hat{\epsilon}_+ + r_0\hat{\epsilon}_0 + r_-\hat{\epsilon}_-) \\
\vec{\xi_b} &= \xi_b\,(b_+\hat{\epsilon}_+ + b_0\hat{\epsilon}_0 + b_-\hat{\epsilon}_-)
\end{aligned}
\tag{5.15}
$$

where $\hat{\epsilon}_0$, $\hat{\epsilon}_-$ and $\hat{\epsilon}_+$ denote π, σ^- and σ^+-polarizations respectively. To obtain the scattering rate in terms of the transition Rabi frequency, the relation between Rabi frequency and electric field has to be derived. For the 3-level qudit, they are derived to be (see Appendix

A)

$$\begin{aligned}\Omega_0 &= \frac{1}{2\sqrt{12}\hbar^2}\left(b_0 r_+ + b_- r_0\right)\left(-\frac{1}{\Delta_{1/2}} + \frac{1}{\Delta_{3/2}}\right)|\langle 6P, L=1||\hat{d}||6S, L=0\rangle|^2\xi_r\xi_b \\ \Omega_1 &= \frac{1}{2\sqrt{12}\hbar^2}\left(b_0 r_- + b_+ r_0\right)\left(\frac{1}{\Delta_{1/2}} - \frac{1}{\Delta_{3/2}}\right)|\langle 6P, L=1||\hat{d}||6S, L=0\rangle|^2\xi_r\xi_b\end{aligned} \tag{5.16}$$

where Ω_l is the Rabi frequency for the transition $|l\rangle \leftrightarrow |l+1\rangle$. For pure polarizations, our scheme assumes $|b_0| = 1$ for any of the two-level transitions and the red Raman beam is either σ^+ or σ^- polarized depending on the transition to be driven. Assuming $\xi_r = \xi_b = \bar{\xi}$, Equation 5.16 can be rewritten in the form

$$\bar{\xi}^2 = \frac{2\sqrt{12}\hbar^2\Omega_{0/1}}{|\langle 6P, L=1||\hat{d}||6S, L=0\rangle|^2}\left(\frac{\Delta_{1/2}\Delta_{3/2}}{\Delta_{1/2}-\Delta_{3/2}}\right) \tag{5.17}$$

To obtain a single parameter to characterize the error due to photon scattering, the encoded state that gives the largest scattering rate from Equation 5.14 is chosen. For Ba^+ ion, Assuming the Raman transitions are driven with 532 nm light, the detuning from the $6P_{1/2}$ and $6P_{3/2}$ states give $\Delta_{1/2} = -44.08\,\text{THz}$ and $\Delta_{3/2} = -94.78\,\text{THz}$. With these parameters, the largest scattering rate is $R_{SE,0}$ with $|r_+| = 1$ or $R_{SE,2}$ with $|r_-| = 1$. Expressing $R_{SE,0}$ with $|b_0| = |r_+| = 1$ and $r_- = 0$ in terms of the Rabi frequency gives

$$R_{SE,0} = \frac{\Omega_0}{\sqrt{12}}\left[5\frac{\gamma_{1/2}}{\Delta_{1/2}^2} + 7\frac{\gamma_{3/2}}{\Delta_{3/2}^2}\right]\left(\frac{\Delta_{1/2}\Delta_{3/2}}{\Delta_{1/2}-\Delta_{3/2}}\right) \tag{5.18}$$

The scattering probability is

$$P_{SE} = R_{SE}t_{gate} \tag{5.19}$$

Thus, assuming the same Rabi frequency, the error will be the largest for the gate with the longest gate time. Assuming a Rabi frequency of 10 kHz for all transitions, the gate with the longest gate time is QFT, where $t_{gate} = 280.4\,\mu\text{s}$ for $d = 3$. With the assumption that a qudit state completely decoheres upon a scattering event, the error due to photon scattering in a single qudit gate is equivalent to P_{SE}.

The same approach is used to compute the error for $d = 5$. The scattering rate for each

encoded state as shown in Figure 5.1b is

$$
\begin{aligned}
R_{SE,0} &= \frac{|\langle 6P, L=1||\hat{d}||6S, L=0\rangle|^2}{4\hbar^2}\Big[\frac{\gamma_{1/2}}{\Delta_{1/2}^2}\Big(\frac{2}{3}\sum_j (r_{+,j}E_{r,j})^2 + \frac{1}{3}\sum_k (b_{0,k}E_{b,k})^2\Big) \\
&\quad + \frac{\gamma_{3/2}}{\Delta_{3/2}^2}\Big(\frac{1}{3}\sum_j (r_{+,j}E_{r,j})^2 + \sum_l (r_{-,l}E_{r,l})^2 + \frac{2}{3}\sum_k (b_{0,k}E_{b,k})^2\Big)\Big] \\
R_{SE,1} &= \frac{|\langle 6P, L=1||\hat{d}||6S, L=0\rangle|^2}{4\hbar^2} \\
&\quad \times \Big[\frac{\gamma_{1/2}}{\Delta_{1/2}^2}\Big(\frac{1}{6}\sum_j (r_{+,j}E_{r,j})^2 + \frac{1}{2}\sum_l (r_{-,l}E_{r,l})^2 + \frac{1}{3}\sum_k (b_{0,k}E_{b,k})^2\Big) \\
&\quad + \frac{\gamma_{3/2}}{\Delta_{3/2}^2}\Big(\frac{5}{6}\sum_j (r_{+,j}E_{r,j})^2 + \frac{1}{2}\sum_l (r_{-,l}E_{r,l})^2 + \frac{2}{3}\sum_k (b_{0,k}E_{b,k})^2\Big)\Big] \\
R_{SE,2} &= \frac{|\langle 6P, L=1||\hat{d}||6S, L=0\rangle|^2}{4\hbar^2} \\
&\quad \times \Big[\frac{\gamma_{1/2}}{\Delta_{1/2}^2}\Big(\frac{1}{3}\sum_j (r_{+,j}E_{r,j})^2 + \frac{1}{3}\sum_l (r_{-,l}E_{r,l})^2 + \frac{1}{3}\sum_k (b_{0,k}E_{b,k})^2\Big) \\
&\quad + \frac{\gamma_{3/2}}{\Delta_{3/2}^2}\Big(\frac{2}{3}\sum_j (r_{+,j}E_{r,j})^2 + \frac{2}{3}\sum_l (r_{-,l}E_{r,l})^2 + \frac{2}{3}\sum_k (b_{0,k}E_{b,k})^2\Big)\Big] \\
R_{SE,3} &= \frac{|\langle 6P, L=1||\hat{d}||6S, L=0\rangle|^2}{4\hbar^2} \\
&\quad \times \Big[\frac{\gamma_{1/2}}{\Delta_{1/2}^2}\Big(\frac{1}{2}\sum_j (r_{+,j}E_{r,j})^2 + \frac{1}{6}\sum_l (r_{-,l}E_{r,l})^2 + \frac{1}{3}\sum_k (b_{0,k}E_{b,k})^2\Big) \\
&\quad + \frac{\gamma_{3/2}}{\Delta_{3/2}^2}\Big(\frac{1}{2}\sum_j (r_{+,j}E_{r,j})^2 + \frac{5}{6}\sum_l (r_{-,l}E_{r,l})^2 + \frac{2}{3}\sum_k (b_{0,k}E_{b,k})^2\Big)\Big] \\
R_{SE,4} &= \frac{|\langle 6P, L=1||\hat{d}||6S, L=0\rangle|^2}{4\hbar^2}\Big[\frac{\gamma_{1/2}}{\Delta_{1/2}^2}\Big(\frac{2}{3}\sum_l (r_{-,l}E_{r,l})^2 + \frac{1}{3}\sum_k (b_{0,k}E_{b,k})^2\Big) \\
&\quad + \frac{\gamma_{3/2}}{\Delta_{3/2}^2}\Big(\sum_j (r_{+,j}E_{r,j})^2 + \frac{1}{3}\sum_l (r_{-,l}E_{r,l})^2 + \frac{2}{3}\sum_k (b_{0,k}E_{b,k})^2\Big)\Big]
\end{aligned}
\tag{5.20}
$$

and the relation between Rabi frequency and electric field amplitude for each transition is

$$\begin{aligned}
\Omega_0 &= \frac{1}{2\hbar^2}\frac{1}{\sqrt{6}}(r_0 b_- + r_+ b_0)(-\frac{1}{\Delta_{1/2}} + \frac{1}{\Delta_{3/2}})|\langle\, 6P, L=1||\hat{d}||\, 6S, L=0\rangle|^2\xi_r\xi_b \\
\Omega_1 &= \frac{1}{2\hbar^2}\frac{1}{6}(b_0 r_- + b_+ r_0)(\frac{1}{\Delta_{1/2}} - \frac{1}{\Delta_{3/2}})|\langle\, 6P, L=1||\hat{d}||\, 6S, L=0\rangle|^2\xi_r\xi_b \\
\Omega_2 &= \frac{1}{2\hbar^2}\frac{1}{6}(r_0 b_- + r_+ b_0)(-\frac{1}{\Delta_{1/2}} + \frac{1}{\Delta_{3/2}})|\langle\, 6P, L=1||\hat{d}||\, 6S, L=0\rangle|^2\xi_r\xi_b \\
\Omega_3 &= \frac{1}{2\hbar^2}\frac{1}{\sqrt{6}}(b_0 r_- + b_+ r_0)(\frac{1}{\Delta_{1/2}} - \frac{1}{\Delta_{3/2}})|\langle\, 6P, L=1||\hat{d}||\, 6S, L=0\rangle|^2\xi_r\xi_b
\end{aligned} \tag{5.21}$$

With the aforementioned assumptions and parameters, the largest scattering rate is $R_{SE,1}$ when the transition $|1\rangle \leftrightarrow |2\rangle$ is being driven with $|b_0| = |r_-| = 1$ and $r_+ = 0$, giving

$$R_{SE,1} = \frac{\Omega_1}{2}\left[5\frac{\gamma_{1/2}}{\Delta_{1/2}^2} + 7\frac{\gamma_{3/2}}{\Delta_{3/2}^2}\right]\left(\frac{\Delta_{1/2}\Delta_{3/2}}{\Delta_{1/2} - \Delta_{3/2}}\right) \tag{5.22}$$

The gate with the longest gate time for $d = 5$ is also QFT, with $t_{gate} = 678.5\,\mu$s.

5.3 Error Calculations and Simulation Results

Simulations are performed for $^{137}Ba^+$ ion, with 8 hyperfine energy states as shown in Figure 5.1. The Scrhödinger's equation as shown in Equation 5.23 is used to evaluate the evolution of a state under a certain Hamiltonian.

$$\frac{d}{dt}|\psi\rangle = -i\hat{H}(t)|\psi\rangle \tag{5.23}$$

Since it is an ordinary differential equation (ODE), it can be approximated numerically with ODE solvers in numerical softwares and toolboxes. The MATLAB function ode113 is used to numerically evaluate the time-evolution of an input state. To evaluate the errors due to magnetic field noise and off-resonant coupling, the following Hamiltonian is used

$$\hat{H} = \hat{H}_{ideal} + \hat{H}_{noise} + \hat{H}_{OR} \tag{5.24}$$

where $\hat{H}_{noise}$ and $\hat{H}_{OR}$ are as defined in Equations 5.6 and 5.11 respectively.

It is found to be too computationally intensive to simulate both off-resonant and magnetic field noise error simultaneously with a time-varying noise. Thus, the deviation in

Error source	$d = 3$	$d = 5$
Magnetic field noise	$(1.16 \pm 0.09) \times 10^{-9}$	$(2.8 \pm 0.2) \times 10^{-9}$
Off-resonant coupling	$(1.12 \pm 0.01) \times 10^{-4}$	$(1.35 \pm 0.02) \times 10^{-3}$
Photon scattering	1.88×10^{-4}	7.87×10^{-4}

Table 5.3: Errors of single qudit $Q\hat{F}T$ gate for each error source considered in this study.

magnetic field is set at a constant offset at the standard deviation of 2.7 pT as an estimation for simulations with both errors taken into account. For this set of simulations, the fidelities with a sample size of 500 are computed for each gate, where each input state is a randomized superposition of the encoded states with random phases. The average fidelities and thus average errors are then computed from the sample. No discernible difference in the average fidelity obtained is observed whether a magnetic field offset is present as the error is dominated by off-resonant coupling. For the simulations with only magnetic field noise present, it is computationally feasible for us to carry out simulations with a time-varying noise. Thus, time series of stochastic magnetic field noise are generated using Ornstein–Uhlenbeck function with a mean of 0, inverse correlation time $\gamma = 0.5\,\mathrm{ms}^{-1}$ [44], and volatility $\sigma = \sqrt{2\gamma\langle\Delta B^2\rangle}$. $\hat{H}_{noise}$ is then computed and $\hat{H} = \hat{H}_{ideal} + \hat{H}_{noise}$ is used to evolve the qudit state with Schrödinger's equation. Fidelities from a sample size of 300 with initial qudit state randomized in the aforementioned manner are computed for each gate. The average fidelities are then computed from the samples. The photon scattering probability P_{SE} is also calculated with Equation 5.19 with the parameters as stated in Section 5.2.3. The error for each error source is tabulated in Table 5.3.

From Table 5.3, it can be seen that error from magnetic field noise is negligible as compared to other error sources. Although the error from photon scattering may seem comparable to error from off-resonant coupling with an unpolarized source in Table 5.3, it is noted that the calculations for photon scattering error is a very crude overestimation as Rayleigh scattering is assumed to cause decoherence too, even though they do not in reality. Nevertheless, the purpose of this study is to assess the practicality of a qudit system, and it can be noted from Table 5.3 that at fidelities of at least 99.98% and 99.8% can be achieved with $d = 3$ and $d = 5$ respectively, which is above the fault tolerant threshold of 99.25%.

Chapter 6

Qudit Mølmer-Sørensen Gate

To form a universal gate set, an entangling gate is required [49]. For trapped ion qubits, the Mølmer-Sørensen gate is commonly used for qubit-qubit entanglement [15, 50, 51]. Ions trapped in an ion chain share common motional modes due to Coulomb force interactions between the ions. Mølmer-Sørensen gate utilizes the common motional modes to mediate entanglement between ions [28].

6.1 Theoretical Derivation

For our qudit system, we choose to generalize Mølmer-Sørensen gate from a qubit entangling gate to a qudit entangling gate. The ideal Hamiltonian for Mølmer-Sørensen gate is of the form [28]

$$\hat{H} = \hbar\eta\Omega(\hat{a}^\dagger e^{i(\omega_M-\mu)t} + \hat{a}e^{-i(\omega_M-\mu)t})\sum_{n=1}^{N}\frac{\hat{\sigma}_{x,n}}{2} \tag{6.1}$$

We treat the operator $\frac{\hat{\sigma}_x}{2}$ to be similar to a spin-half system. The generalization to the qudit version is made by generalizing the "spin" operator to an arbitrary spin system. A d-level qudit would be in a spin-s system, where

$$s = \frac{d-1}{2} \tag{6.2}$$

Making this generalization, the ideal Mølmer-Sørensen gate for the qudit version is

$$\hat{H} = \hbar\eta\Omega(\hat{a}^\dagger e^{i(\omega_M-\mu)t} + \hat{a}e^{-i(\omega_M-\mu)t})\sum_{n=1}^{N}\hat{S}_{x,n} \tag{6.3}$$

where

$$\begin{aligned}
\hat{S}_x &= \frac{\hat{S}_+ + \hat{S}_-}{2} \\
\hat{S}_+ &= \sum_{l'=-s}^{s-1} \sqrt{s(s+1) - l'(l'+1)} |l'+s+1\rangle\langle l'+s| \\
\hat{S}_- &= \sum_{l'=-s}^{s-1} \sqrt{s(s+1) - l'(l'+1)} |l'+s\rangle\langle l'+s+1|
\end{aligned} \tag{6.4}$$

To arrive at the ideal Hamiltonian in Equation 6.3, we start with N number of ions trapped in a chain. The static Hamiltonian is

$$\begin{aligned}
\hat{H}_0 &= \hat{H}_{0,M} + \hat{H}_{0,S} \\
\hat{H}_{0,M} &= \sum_{m=1}^{N} \hbar\omega_m (\hat{a}_m^\dagger \hat{a}_m + \frac{1}{2}) \\
\hat{H}_{0,S} &= \sum_{n=1}^{N} \sum_{l=0}^{d-1} E_{l,n} |l\rangle\langle l|_n,
\end{aligned} \tag{6.5}$$

where $\hat{H}_{0,M}$ describes the Hamiltonian of the motional state, $\hat{H}_{0,S}$ describes the Hamiltonian of the internal energy states, and E_l is the energy of state $|l\rangle$, and $l = l' + s$. For each transition level between $|l\rangle$ and $|l+1\rangle$, a laser perturbation with frequency $\omega_{L,l}$ is applied. Assuming that each of this laser perturbation, $\omega_{L,l}$, is only close to resonance to the specific transition from $|l\rangle$ and $|l+1\rangle$ and far off-resonant to (or forbidden by selection rules for) transitions to the other levels. The interaction Hamiltonian introduced by this laser perturbation can then be approximated to be

$$\hat{H}_{int} = \sum_{n=1}^{N} \sum_{l=0}^{d-1} \hbar\Omega_{l,n} \cos\left(k\hat{x}_n - \omega_{L,l}t + \phi_l\right) \left(|l+1\rangle\langle l|_n + |l\rangle\langle l+1|_n\right) \tag{6.6}$$

where $\hat{x}$ is the position of an ion along the motion of the phonon mode being used for entanglement, k is the wavevector of the laser perturbation along $\hat{x}$, ϕ is the initial laser phase. The total Hamiltonian is then

$$\hat{H} = \hat{H}_{0,M} + \hat{H}_{0,S} + \hat{H}_{int} \tag{6.7}$$

Assigning odd qudit levels to lower energy levels and even qudit levels to higher ones in a zigzag pattern as shown in Figure 6.1, we define

$$E_{l+1} - E_l = -(-1)^l \hbar \omega_l. \tag{6.8}$$

By going into the interaction picture with respect to $\hat{H}_0$, the effective Hamiltonian is

$$\begin{aligned}
\hat{H} &= \exp\left(i\frac{\hat{H}_0}{\hbar}t\right)\hat{H}_{int}\exp\left(-i\frac{\hat{H}_0}{\hbar}t\right) \\
&= \sum_{n=1}^{N}\sum_{l=0}^{d-1}\hbar\Omega_{l,n}\cos\left(ke^{i\frac{\hat{H}_{0,M}}{\hbar}t}\hat{x}_n e^{-i\frac{\hat{H}_{0,M}}{\hbar}t} - \omega_{L,l}t + \phi_l\right) \\
&\times\left(e^{i\frac{\hat{H}_{0,S}}{\hbar}t}|l+1\rangle\langle l|_n e^{-i\frac{\hat{H}_{0,S}}{\hbar}t} + e^{i\frac{\hat{H}_{0,S}}{\hbar}t}|l\rangle\langle l+1|_n e^{-i\frac{\hat{H}_{0,S}}{\hbar}t}\right) \\
&= \sum_{n=1}^{N}\sum_{l=0}^{d-1}\hbar\Omega_{l,n}\cos\left(k\hat{x}'_n - \omega_{L,l}t + \phi_l\right) \\
&\times\left(e^{-i(-1)^l\omega_l t}|l+1\rangle\langle l|_n + e^{i(-1)^l\omega_l t}|l\rangle\langle l+1|_n\right)
\end{aligned} \tag{6.9}$$

where we have defined $\hat{x}'_n = e^{i\frac{\hat{H}_{0,M}}{\hbar}t}\hat{x}_n e^{-i\frac{\hat{H}_{0,M}}{\hbar}t}$ to be the position operator in the interaction picture.

To arrive at the desired Hamiltonian, 2 of such perturbations are applied to each $|l\rangle$ to $|l+1\rangle$ transition. One of them is blue detuned from the $|l\rangle$ to $|l+1\rangle$ resonance by μ while the other is red detuned by the same amount, as shown in Equation 6.10.

$$\begin{aligned}
\omega_{L,l} &= \omega_l + \mu \text{ (blue-detuned)} \\
\omega_{L,l} &= \omega_l - \mu \text{ (red-detuned)}
\end{aligned} \tag{6.10}$$

Consider the component of the Hamiltonian from the blue-detuned perturbation. Sub-

stituting the blue detuned frequencies in Equation 6.10 to Equation 6.9 gives

$$\begin{aligned}
\hat{H}_b &= \sum_{n=1}^{N}\sum_{l=0}^{d-1} \hbar\Omega_{l,n}\cos\left(k\hat{x}'_n - \omega_l t - \mu t + \phi_l\right) \\
&\times \left(e^{-i(-1)^l\omega_l t}|l+1\rangle\langle l|_n + e^{i(-1)^l\omega_l t}|l\rangle\langle l+1|_n\right) \\
&= \sum_{n=1}^{N}\sum_{l=0}^{d-1} \frac{\hbar\Omega_{l,n}}{2}\left(e^{i(k\hat{x}'_n-\omega_l t-\mu t+\phi_l)} + e^{-i(k\hat{x}'_n-\omega_l t-\mu t+\phi_l)}\right) \\
&\times \left(e^{-i(-1)^l\omega_l t}|l+1\rangle\langle l|_n + e^{i(-1)^l\omega_l t}|l\rangle\langle l+1|_n\right) \\
&= \sum_{n=1}^{N}\sum_{l=0}^{d-1} \frac{\hbar\Omega_{l,n}}{2}\Big[\left(e^{-i(-1)^l\left(k\hat{x}'_n-\mu t+\phi_{b,l}\right)} + e^{i(-1)^l\left(k\hat{x}'_n-2\omega_l t-\mu t+\phi_{b,l}\right)}\right)|l+1\rangle\langle l|_n \\
&+ \left(e^{i(-1)^l\left(k\hat{x}'_n-\mu t+\phi_{b,l}\right)} + e^{-i(-1)^l\left(k\hat{x}'_n-2\omega_l t-\mu t+\phi_{b,l}\right)}\right)|l\rangle\langle l+1|_n\Big]
\end{aligned} \tag{6.11}$$

Making a rotating wave approximation (RWA), where the terms with fast rotating terms $e^{\pm i(2\omega_l+\mu)t}$ can be neglected provided that $\Omega_{l,n} \ll \omega_l$. With this approximation, Equation 6.11 is transformed to

$$\hat{H}_b \approx \sum_{n=1}^{N}\sum_{l=0}^{d-1} \frac{\hbar\Omega_{l,n}}{2}\left[e^{-i(-1)^l\left(k\hat{x}'_n-\mu t+\phi_{b,l}\right)}|l+1\rangle\langle l|_n + e^{i(-1)^l\left(k\hat{x}'_n-\mu t+\phi_{b,l}\right)}|l\rangle\langle l+1|_n\right] \tag{6.12}$$

For the component of the Hamiltonian from the red-detuned perturbations, it is the same form in Equation 6.12, but with μ replaced by $-\mu$.

$$\hat{H}_r \approx \sum_{n=1}^{N}\sum_{l=0}^{d-1} \frac{\hbar\Omega_{l,n}}{2}\left[e^{-i(-1)^l\left(k\hat{x}'_n+\mu t+\phi_{r,l}\right)}|l+1\rangle\langle l|_n + e^{i(-1)^l\left(k\hat{x}'_n+\mu t+\phi_{r,l}\right)}|l\rangle\langle l+1|_n\right] \tag{6.13}$$

The resultant Hamiltonian is the summation of $\hat{H}_b$ and $\hat{H}_r$.

$$\begin{aligned}
\hat{H} &= \hat{H}_b + \hat{H}_r \\
&\approx \sum_{n=1}^{N}\sum_{l=0}^{d-1} \frac{\hbar\Omega_{l,n}}{2}\Big[\left(e^{-i(-1)^l\left(k\hat{x}'_n-\mu t+\phi_{b,l}\right)} + e^{-i(-1)^l\left(k\hat{x}'_n+\mu t+\phi_{r,l}\right)}\right)|l+1\rangle\langle l|_n \\
&+ \left(e^{i(-1)^l\left(k\hat{x}'_n-\mu t+\phi_{b,l}\right)} + e^{i(-1)^l\left(k\hat{x}'_n+\mu t+\phi_{r,l}\right)}\right)|l\rangle\langle l+1|_n\Big] \\
&= \sum_{n=1}^{N}\sum_{l=0}^{d-1} \frac{\hbar\Omega_{l,n}}{2} \\
&\times \Big[e^{-i(-1)^l\left(k\hat{x}'_n+\frac{\phi_{r,l}+\phi_{b,l}}{2}\right)}\left(e^{-i(-1)^l\left(-\mu t-\frac{\phi_{r,l}-\phi_{b,l}}{2}\right)} + e^{-i(-1)^l\left(\mu t+\frac{\phi_{r,l}-\phi_{b,l}}{2}\right)}\right)|l+1\rangle\langle l|_n \\
&+ e^{i(-1)^l\left(k\hat{x}'_n-\frac{\phi_{r,l}+\phi_{b,l}}{2}\right)}\left(e^{-i(-1)^l\left(\mu t+\frac{\phi_{r,l}-\phi_{b,l}}{2}\right)} + e^{-i(-1)^l\left(-\mu t-\frac{\phi_{r,l}-\phi_{b,l}}{2}\right)}\right)|l\rangle\langle l+1|_n\Big] \\
&= \sum_{n=1}^{N}\sum_{l=0}^{d-1} \hbar\Omega_{l,n}\cos\left(\mu t+\phi_{M,l}\right)\Big[e^{-i(-1)^l k\hat{x}'_n}e^{-i(-1)^l\phi'_{S,l}}|l+1\rangle\langle l|_n \\
&+ e^{i(-1)^l k\hat{x}'_n}e^{i(-1)^l\phi'_{S,l}}|l\rangle\langle l+1|_n\Big]
\end{aligned} \tag{6.14}$$

where we have defined

$$\begin{aligned}
\phi_{M,l} &= \frac{\phi_{r,l}-\phi_{b,l}}{2} \\
\phi'_{S,l} &= \frac{\phi_{r,l}+\phi_{b,l}}{2}
\end{aligned} \tag{6.15}$$

For small $k\hat{x}'$, the Lamb-Dicke approximation can be applied, which gives

$$e^{\pm i(-1)^l k\hat{x}'} \approx 1 \pm i(-1)^l k\hat{x}' \tag{6.16}$$

An ion chain with N ions has N normal modes [52]. Thus, the position of an ion can be expressed in terms of the summation of each of the normal mode.

$$\begin{aligned}
k\hat{x}_n &= k\sum_{m=1}^{N} b_n^{(m)}\hat{X}_m \\
&= \sum_{m=1}^{N}\eta_{m,n}\left(\hat{a}_m^\dagger + \hat{a}_m\right)
\end{aligned} \tag{6.17}$$

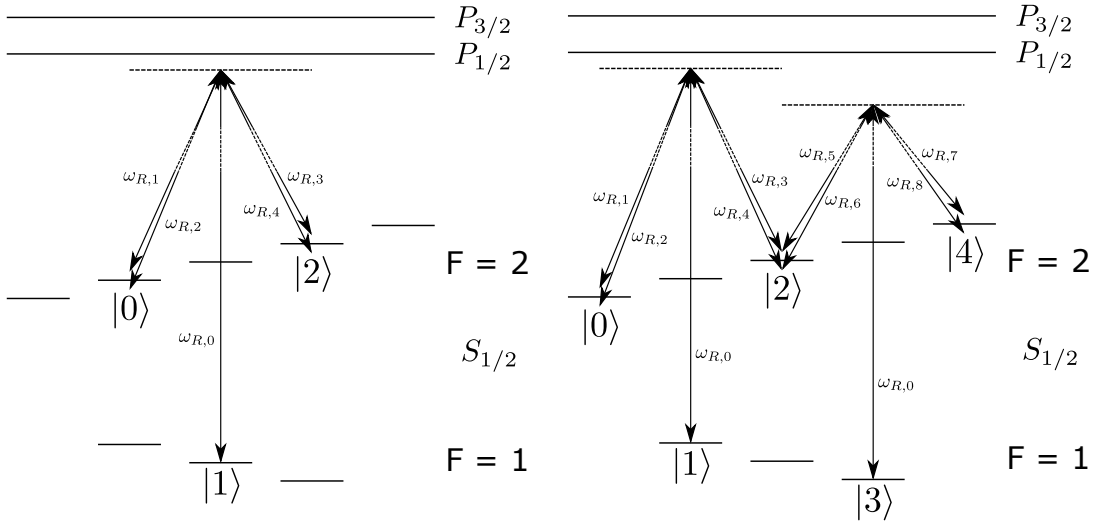

Figure 6.1: Schematics of energy level structure of $^{137}Ba^{+}$ with Zeeman splitting of the hyperfine levels and laser perturbations applied for (a) 3-level qudit and (b) 5-level qudit entangling gate. $\omega_{R,n}$ denotes the n^{th} laser frequency applied for the entangling gate.

where $b_n^{(m)}$ is an element in the transformation matrix of the n^{th} ion with the m^{th} normal mode, $\hat{X}_m$ is the displacement operator for the m^{th} mode, $\eta_{m,n}$ is the Lamb-Dicke parameter of the n^{th} ion for the m^{th} mode, $\hat{a}_m^\dagger$ and $\hat{a}_m$ are the raising and lowering operator of the m^{th} normal mode respectively. In the interaction picture,

$$\begin{aligned} k\hat{x}'_n &= \sum_{m=1}^{N} \eta_{m,n} \left(e^{i\frac{\hat{H}_{0,M}}{\hbar}t} \hat{a}_m^\dagger e^{-i\frac{\hat{H}_{0,M}}{\hbar}t} + e^{i\frac{\hat{H}_{0,M}}{\hbar}t} \hat{a}_m e^{-i\frac{\hat{H}_{0,M}}{\hbar}t} \right) \\ &= \sum_{m=1}^{N} \eta_{m,n} \left(e^{i\omega_m t} \hat{a}_m^\dagger + e^{-i\omega_m t} \hat{a}_m \right) \end{aligned} \tag{6.18}$$

where ω_m is the motional frequency of the m^{th} normal mode.

Plugging Equations 6.16 and 6.18 into Equation 6.14 gives

$$\begin{aligned}\hat{H} \approx & \sum_{n=1}^{N}\sum_{l=0}^{d-1}\hbar\Omega_{l,n}\cos\left(\mu t+\phi_{M,l}\right)\left[e^{-i(-1)^l\phi'_{S,l}}|l+1\rangle\langle l|_n+e^{i(-1)^l\phi'_{S,l}}|l\rangle\langle l+1|_n\right]\\ &+\sum_{m=1}^{N}\sum_{n=1}^{N}\sum_{l=0}^{d-1}\hbar\eta_{m,n}\Omega_{l,n}\cos\left(\mu t+\phi_{M,l}\right)\left(e^{i\omega_m t}\hat{a}_m^\dagger+e^{-i\omega_m t}\hat{a}_m\right)\\ &\times\left[-i\left(-1\right)^l e^{-i(-1)^l\phi'_{S,l}}|l+1\rangle\langle l|_n+i\left(-1\right)^l e^{i(-1)^l\phi'_{S,l}}|l\rangle\langle l+1|_n\right]\end{aligned} \tag{6.19}$$

Consider the case where the detuning of the perturbation, μ, is close to one of the centre-of-mass (COM) normal mode frequency, $\omega_m = \omega_C$ where the subscript C denotes the centre-of-mass mode, i.e. $\mu \approx \omega_C$. For the case where $\mu \ll \Omega_{l,n}$ and $|\mu - \omega_m| \ll \Omega_{l,n}$ for $m \neq C$, RWA can again be applied and the following Hamiltonian is obtained

$$\begin{aligned}\hat{H} &\approx \sum_{n=1}^{N}\sum_{l=0}^{d-1}\frac{\hbar\eta_C\Omega_{l,n}}{2}\left(e^{i(\omega_C-\mu)t-i\phi_{M,l}}\hat{a}_C^\dagger+e^{-i(\omega_C-\mu)t+i\phi_{M,l}}\hat{a}_C\right)\\ &\times\left[-i\left(-1\right)^l e^{-i(-1)^l\phi'_{S,l}}|l+1\rangle\langle l|_n+i\left(-1\right)^l e^{i(-1)^l\phi'_{S,l}}|l\rangle\langle l+1|_n\right]\\ &=\sum_{n=1}^{N}\sum_{l=0}^{d-1}\frac{\hbar\eta_C\Omega_{l,n}}{2}\left(e^{i(\omega_C-\mu)t-i\phi_{M,l}}\hat{a}_C^\dagger+e^{-i(\omega_C-\mu)t+i\phi_{M,l}}\hat{a}_C\right)\\ &\times\left[e^{-i(-1)^l\left(\phi'_{S,l}+\frac{\pi}{2}\right)}|l+1\rangle\langle l|_n+e^{i(-1)^l\left(\phi'_{S,l}+\frac{\pi}{2}\right)}|l\rangle\langle l+1|_n\right]\end{aligned} \tag{6.20}$$

By controlling the perturbation phases and amplitudes such that

$$\begin{aligned}\phi_S &= -\left(-1\right)^l\left(\phi'_{S,l}+\frac{\pi}{2}\right)\\ \phi_M &= \phi_{M,l}\text{ for all }l\\ \Omega_l &= \bar{\Omega}\sqrt{s(s+1)-l'(l'+1)}\end{aligned} \tag{6.21}$$

We arrive at the Hamiltonian

$$\begin{aligned}\hat{H} \approx & \sum_{n=1}^{N}\sum_{l=0}^{d-1}\hbar\eta_C\bar{\Omega}\left(e^{i(\omega_C-\mu)t-i\phi_M}\hat{a}_C^\dagger+e^{-i(\omega_C-\mu)t+i\phi_M}\hat{a}_C\right)\\ &\times\frac{\sqrt{s(s+1)-l'(l'+1)}}{2}\left[e^{i\phi_S}|l+1\rangle\langle l|_n+e^{-i\phi_S}|l\rangle\langle l+1|_n\right]\end{aligned} \tag{6.22}$$

From Equation 6.22, it can be seen that ϕ_M and ϕ_S are associated with the motional and "spin" operators of the ions respectively. Thereby, ϕ_M and ϕ_S are called the motional and spin phases. By defining

$$\hat{S}_{\phi_S} = \sum_{l'=-s}^{s-1} \frac{\sqrt{s(s+1) - l'(l'+1)}}{2} \left[e^{i\phi_S} |l'+s+1\rangle\langle l'+s|_n + e^{-i\phi_S} |l'+s\rangle\langle l'+s+1|_n \right] \tag{6.23}$$

as the general "spin" operator with spin phase ϕ_S, we arrive at

$$\hat{H} \approx \sum_{n=1}^{N} \hbar\eta_C\bar{\Omega} \left(e^{i(\omega_C-\mu)t - i\phi_M} \hat{a}_C^\dagger + e^{-i(\omega_C-\mu)t + i\phi_M} \hat{a}_C \right) \hat{S}_{\phi_S} \tag{6.24}$$

By setting the laser phases such that the motional and spin phases are both 0, i.e. $\phi_M = 0$ and $\phi_S = 0$, we obtain the ideal Hamiltonian as shown in Equation 6.3.

To evaluate how a state under this Hamiltonian would evolve with time, we need to solve Schrodinger's equation as shown in Equation 5.23 to obtain the time evolution operator. For a time-varying Hamiltonian, the solution to the Schrodinger's equation can be approximated with Magnus expansion [53].

$$\hat{U}(t) = e^{\sum_k \hat{M}_k(t)} \tag{6.25}$$

where $\hat{M}_k(t)$ is the k^{th} order Magnus expansion. With the ideal Hamiltonian in Equation 6.3, the first order Magnus expansion is

$$\begin{aligned} M_1(t) &= -\frac{i}{\hbar} \int_0^t \hat{H}(t_1)\, dt_1 \\ &= \left(\alpha(t)\hat{a}^\dagger - \alpha^*(t)\hat{a}\right) \sum_{n=1}^{N} \hat{S}_{x,n} \\ \alpha(t) &= \frac{\eta_C\Omega}{\omega_C - \mu} \left[1 - e^{i(\omega_M-\mu)t}\right] \end{aligned} \tag{6.26}$$

The second order Magnus expansion is

$$M_2(t) = -\frac{1}{2\hbar^2} \int_0^t dt_1 \int_0^{t_1} [\hat{H}(t_1), \hat{H}(t_2)]\, dt_2 \tag{6.27}$$

Evaluating the commutator in Equation 6.27 gives

$$\begin{aligned}\left[\hat{H}(t_1), \hat{H}(t_2)\right] &= \hbar^2\eta_C^2\bar{\Omega}^2\Big(e^{i(\omega_C-\mu)t_1-i(\omega_C-\mu)t_2}\left[\hat{a}_C^\dagger, \hat{a}_C\right] \\ &\quad + e^{-i(\omega_C-\mu)t_1+i(\omega_C-\mu)t_2}\left[\hat{a}_C, \hat{a}_C^\dagger\right]\Big)\left(\sum_{n=1}^{N}\hat{S}_{x,n}\right)^2 \\ &= \hbar^2\eta_C^2\bar{\Omega}^2\Big(-e^{i(\omega_C-\mu)t_1-i(\omega_C-\mu)t_2}+e^{-i(\omega_C-\mu)t_1+i(\omega_C-\mu)t_2}\Big)\left(\sum_{n=1}^{N}\hat{S}_{x,n}\right)^2 \\ &= 2i\hbar^2\eta_C^2\bar{\Omega}^2\Big(\sin\left((\omega_C-\mu)\,t_2-(\omega_C-\mu)\,t_1\right)\Big)\left(\sum_{n=1}^{N}\hat{S}_{x,n}\right)^2\end{aligned} \tag{6.28}$$

Plugging Equation 6.28 into Equation 6.27 gives

$$\begin{aligned}M_2(t) &= -i\eta_C^2\bar{\Omega}^2\int_0^t\int_0^{t_1}\Big(\sin\left((\omega_C-\mu)\,t_2-(\omega_C-\mu)\,t_1\right)\Big)\left(\sum_{n=1}^{N}\hat{S}_{x,n}\right)^2 dt_2\,dt_1 \\ &= -i\eta_C^2\bar{\Omega}^2\int_0^t\Big(-\frac{1}{\omega_C-\mu}+\frac{\cos\left((\omega_C-\mu)\,t_1\right)}{\omega_C-\mu}\Big)\left(\sum_{n=1}^{N}\hat{S}_{x,n}\right)^2 dt_1 \\ &= i\frac{\eta_C^2\bar{\Omega}^2}{\omega_C-\mu}\Big(t-\frac{\sin\left((\omega_C-\mu)\,t\right)}{\omega_C-\mu}\Big)\left(\sum_{n=1}^{N}\hat{S}_{x,n}\right)^2\end{aligned} \tag{6.29}$$

For the case where $t \gg |\frac{\sin((\omega_C-\mu)t)}{\omega_C-\mu}|$, the second order Magnus expansion can be approximated as

$$M_2(t) \approx i\frac{\eta_C^2\hat{\Omega}^2}{\omega_C-\mu}t\left(\sum_{n=1}^{N}\hat{S}_{x,n}\right)^2 \tag{6.30}$$

For higher order Magnus expansions, i.e. $k \geq 3$, they are zero since $\left[\hat{H}(t_1)\left[\hat{H}(t_2), \hat{H}(t_3)\right]\right] = 0$.

To minimize coupling to the phonon states (which is equivalent to minimizing $M_1(t)$ and closing the loop in the phase space picture in Figure 6.2a) and obtain the desired entangling gate, we require

$$t = K\frac{2\pi}{|\omega_C-\mu|}, \tag{6.31}$$

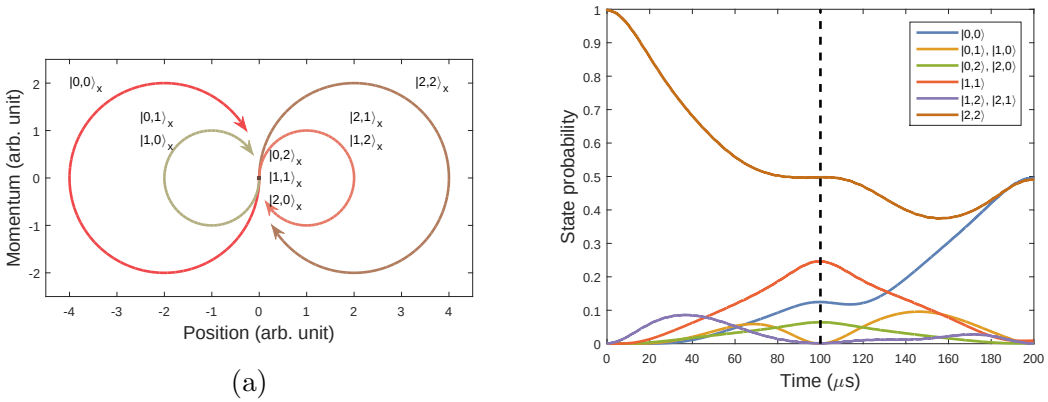

(a) (b)

Figure 6.2: (a) Illustration of evolution of 3-level qudits in phase space. (b) State probability evolution of the 3-level qudit entangling gate with $\theta_0 = -\frac{\pi}{4}$ at $t = \frac{2\pi}{\omega_C - \mu} = 100\,\mu$s. The dashed line marks the time when the desired entangled output state is achieved.

where K is a positive integer. The resultant unitary of the generalized Mølmer-Sørensen gate is then

$$\hat{U} = \exp\left(\frac{2i\eta_C^2\bar{\Omega}^2\pi}{(\omega_C - \mu)\,|\omega_C - \mu|} K \left(\sum_{n=1}^{N} \hat{S}_{x,n}\right)^2\right) \tag{6.32}$$

The ion qudits in eigenstates of $\hat{S}_x$ after the gate in Equation 6.32 gains a phase of

$$\begin{aligned} \theta &= \theta_0 \left(\sum_{n=1}^{N} \lambda_n\right)^2 \\ \theta_0 &= \frac{2K\eta_C^2\bar{\Omega}^2\pi}{(\omega_C - \mu)|\omega_C - \mu|}, \end{aligned} \tag{6.33}$$

where λ_n is the eigenvalue of the n^{th} ion with respect to $\hat{S}_x$. For a two-qudit gate, $N = 2$, and the output is an entangled 2-qudit state in general.

In the phase space picture as shown in Figure 6.2a, this operation corresponds to displacing the system in the phase space with a radius proportional to $S_{x,1} + S_{x,2}$. The geometric phase gained after closing the loop is proportional to the area enclosed by the trajectory, which is proportional to $(S_{x,1} + S_{x,2})^2$.

6.2 Error Sources

In order to estimate the expected error of the two-qudit entangling gate, we consider sources of error that are intrinsic to the formulation as well as experimental imperfections that are difficult to overcome. The intrinsic sources of error are:

1. Inaccuracy from Lamb-Dicke approximation.
2. Inaccuracy from RWA.
3. Presence of spectator phonon modes.
4. Photon scattering.

The experimental imperfections deemed difficult to overcome are:

5. Imperfect cooling of ions.
6. Motional heating of ions.
7. Magnetic field noise.

6.2.1 Lamb-Dicke Approximation

In Section 6.1, one of the approximations made is the Lamb-Dicke approximation (LDA), which can be found in Equation 6.16. This approximation introduces some error into the qudit entangling gate. In this section, focus is put on obtaining the time evolution operator without making the LDA in order to analytically investigate the forms of error introduced by LDA.

Without making the LDA, considering only the centre-of-mass mode, the form for Equation 6.16 is

$$\begin{aligned} e^{\pm ik\hat{x}'} &= e^{\pm i\left(e^{i\omega_C t}\hat{a}_C^\dagger + e^{-i\omega_C t}\hat{a}\right)} \\ &= \sum_{n=0}^{\infty} \frac{\left[\pm i\eta_C \left(e^{i\omega_C t}\hat{a}^\dagger + e^{-i\omega_C t}\hat{a}\right)\right]^n}{n!} \end{aligned} \tag{6.34}$$

For the purpose of deriving the error due to LDA, it is useful to rewrite Equation 6.34 as

$$\begin{aligned} e^{\pm i\left(e^{i\omega_C t}\hat{a}_C^\dagger + e^{-i\omega_C t}\hat{a}\right)} &= f_0\left(\hat{n}, \pm\eta_C\right) + e^{i\omega_C t}\hat{a}^\dagger f_1\left(\hat{n}, \pm\eta_C\right) + e^{-i\omega_C t}\hat{a} f_{-1}\left(\hat{n}, \pm\eta_C\right) \\ &+ e^{i2\omega_C t}\left(\hat{a}^\dagger\right)^2 f_2\left(\hat{n}, \pm\eta_C\right) + e^{-i2\omega_C t}\hat{a}^2 f_{-2}\left(\hat{n}, \pm\eta_C\right) + \cdots \end{aligned} \tag{6.35}$$

where $f_k(\hat{n}, \eta)$ is some function of the $\hat{n}$ operator for k-phonon transition.

Before plugging in Equation 6.35 into Equation 6.14, it can be noted that if the condition $\hat{\Omega_{l,n}} \ll \mu$ holds true, RWA can be applied. As a result, the only significant terms for the expansion in Equation 6.35 are the single phonon transition terms, $f_1\left(\hat{n}, \pm\eta_C\right)\hat{a}^\dagger e^{i\omega_C t}$ and $f_{-1}\left(\hat{n}, \pm\eta_C\right)\hat{a}e^{-i\omega_C t}$, as they are the only terms that give the slowly varying terms with a frequency of $|\mu - \omega_m|$ in the Hamiltonian.

From Ref. [28], the matrix element for a single phonon transition, $|n\rangle$ to $|n-1\rangle$ is

$$\langle n-1|e^{\pm i\eta_C\left(\hat{a}_C^\dagger + \hat{a}_C\right)}|n\rangle = \pm i\eta_C \frac{e^{-\eta_C^2/2}}{\sqrt{n}} L_{n-1}^1\left(\eta_C^2\right) \tag{6.36}$$

where L_{n-1}^1 are the generalized Laguerre polynomials

$$L_n^\alpha(x) = \sum_{m=0}^{n} (-1)^m \begin{pmatrix} n+\alpha \\ n-m \end{pmatrix} \frac{x^m}{m!} = \sum_{m=0}^{n} (-1)^m \frac{(n+\alpha)!x^m}{(n-m)!\,(m+\alpha)!m!} \tag{6.37}$$

To obtain the form of $f_{-1}\left(\hat{n}\right)$ from the matrix element, it can be noted that

$$\begin{aligned} \langle n-1|e^{\pm i\eta_C\left(\hat{a}_C^\dagger + \hat{a}_C\right)}|n\rangle &= \pm i\eta_C \frac{e^{-\eta_C^2/2}}{\sqrt{n}} L_{n-1}^1\left(\eta_C^2\right) \\ &= \pm i\eta_C \frac{e^{-\eta_C^2/2}}{n} L_{n-1}^1\left(\eta_C^2\right)\langle n-1|\hat{a}|n\rangle \\ &= \langle n-1|\hat{a}\left(\pm i\eta_C \frac{e^{-\eta_C^2/2}}{\hat{n}} L_{\hat{n}-1}^1\left(\eta_C^2\right)\right)|n\rangle \end{aligned} \tag{6.38}$$

Thus,

$$f_{-1}\left(\hat{n}, \pm\eta_C\right) = \pm i\eta_C \frac{e^{-\eta_C^2/2}}{\hat{n}} L_{\hat{n}-1}^1\left(\eta_C^2\right) \tag{6.39}$$

To derive $f_1(\hat{n})$, we note that

$$\begin{aligned}\langle n+1|e^{\pm i\eta_C\left(\hat{a}_C^\dagger+\hat{a}_C\right)}|n\rangle &= \pm i\eta_C\frac{e^{-\eta_C^2/2}}{\sqrt{n+1}}L_n^1\left(\eta_C^2\right)\\ &= \pm i\eta_C\frac{e^{-\eta_C^2/2}}{n+1}L_n^1\left(\eta_C^2\right)\langle n+1|\hat{a}_C^\dagger|n\rangle\\ &= \langle n+1|\hat{a}_C^\dagger\left(\pm i\eta_C\frac{e^{-\eta_C^2/2}}{\hat{n}+1}L_{\hat{n}}^1\left(\eta_C^2\right)\right)|n\rangle\end{aligned} \tag{6.40}$$

This implies that

$$f_1(\hat{n},\pm\eta_C) = \pm i\eta_C\frac{e^{-\eta_C^2/2}}{\hat{n}+1}L_{\hat{n}}^1\left(\eta_C^2\right) \tag{6.41}$$

From Equations 6.41 and 6.39, it can be inferred that

$$f_{\pm1}(\hat{n},\pm\eta_C) = \pm f_{\pm1}(\hat{n},\eta_C) \tag{6.42}$$

and

$$f_{-1}(\hat{n},\eta_C) = f_1(\hat{n}-1,\eta_C) \tag{6.43}$$

Thus, keeping only the terms with single phonon transition, plugging Equation 6.35 into Equation 6.14 gives

$$\begin{aligned}\hat{H} \approx& \sum_{n=1}^{N}\sum_{l=0}^{d-1}\hbar\Omega_{l,n}\cos\left(\mu t+\phi_{M,l}\right)\\ &\times\Big[-(-1)^l\left(e^{i\omega_C t}\hat{a}_C^\dagger f_1(\hat{n},\eta_C)+e^{-i\omega_C t}\hat{a}_C f_1(\hat{n}-1,\eta_C)\right)e^{-i(-1)^l\phi'_{S,l}}|l+1\rangle\langle l|_n\\ &+(-1)^l\left(e^{i\omega_C t}\hat{a}_C^\dagger f_1(\hat{n},\eta_C)+e^{-i\omega_C t}\hat{a}_C f_1(\hat{n}-1,\eta_C)\right)e^{i(-1)^l\phi'_{S,l}}|l\rangle\langle l+1|_n\Big]\\ =& \sum_{n=1}^{N}\sum_{l=0}^{d-1}\frac{\hbar\Omega_{l,n}}{i}\cos\left(\mu t+\phi_{M,l}\right)\\ &\times\Big[-i(-1)^l\left(e^{i\omega_C t}\hat{a}_C^\dagger f_1(\hat{n},\eta_C)+e^{-i\omega_C t}\hat{a}_C f_1(\hat{n}-1,\eta_C)\right)e^{-i(-1)^l\phi'_{S,l}}|l+1\rangle\langle l|_n\\ &+i(-1)^l\left(e^{i\omega_C t}\hat{a}_C^\dagger f_1(\hat{n},\eta_C)+e^{-i\omega_C t}\hat{a}_C f_1(\hat{n}-1,\eta_C)\right)e^{i(-1)^l\phi'_{S,l}}|l\rangle\langle l+1|_n\Big]\end{aligned} \tag{6.44}$$

With the definition of the motional and spin phases as defined in Equation 6.22 and making a RWA, the Hamiltonian can be rewritten as

$$\begin{aligned}
\hat{H} &\approx \sum_{n=1}^{N}\sum_{l=0}^{d-1} \frac{\hbar\Omega_{l,n}}{i}\left(e^{i(\omega_C-\mu)t-i\phi_M}\hat{a}_C^\dagger f_1\left(\hat{n},\eta_C\right)+e^{-i(\omega_C-\mu)t+i\phi_M}\hat{a}_C f_1\left(\hat{n}-1,\eta_C\right)\right) \\
&\times \frac{e^{i\phi_S}|l+1\rangle\langle l|_n + e^{i\phi_S}|l\rangle\langle l+1|_n}{2} \\
&= \sum_{n=1}^{N}\sum_{l=0}^{d-1} \hbar\eta_C\Omega_{l,n}\left(e^{i(\omega_C-\mu)t-i\phi_M}\hat{a}_C^\dagger \frac{f_1\left(\hat{n},\eta_C\right)}{i\eta_C}+e^{-i(\omega_C-\mu)t+i\phi_M}\hat{a}_C \frac{f_1\left(\hat{n}-1,\eta_C\right)}{i\eta_C}\right)\hat{S}_{\phi_S} \\
&= \sum_{n=1}^{N}\sum_{l=0}^{d-1} \hbar\eta_C\Omega_{l,n}\left(e^{i(\omega_C-\mu)t-i\phi_M}\hat{a}_C^\dagger g_1\left(\hat{n},\eta_C\right)+e^{-i(\omega_C-\mu)t+i\phi_M}\hat{a} g_1\left(\hat{n}-1,\eta_C\right)\right)\hat{S}_{\phi_S}
\end{aligned} \tag{6.45}$$

where we have defined $g_1\left(\hat{n},\eta_C\right) = \frac{f_1(\hat{n},\eta_C)}{i\eta_C}$. Comparing Equation 6.45 with Equatoin 6.24, it can be seen that not making the LDA transforms $\hat{a}_C^\dagger \rightarrow \hat{a}_C^\dagger g_1\left(\hat{n},\eta_C\right)$ and $\hat{a}_C \rightarrow \hat{a}_C g_1\left(\hat{n}-1,\eta_C\right)$. To obtain the time evolution operator with this Hamiltonian, the Magnus expansion is employed again to evaluate the solution to the Schrodinger's equation. For simplicity, the case where $\phi_M = 0$ and $\phi_S = 0$ is evaluated. The first order Magnus expansion is straightforward and the following is obtained

$$\begin{aligned}
M_1(t) &= -\frac{i}{\hbar}\int_0^t \hat{H}(t_1)\,dt_1 \\
&= \left(\alpha(t)\hat{a}_C^\dagger g_1\left(\hat{n},\eta_C\right) - \alpha^*(t)\hat{a}_C g_1\left(\hat{n}-1,\eta_C\right)\right)\sum_{n=1}^{N}\hat{S}_{x,n} \\
\alpha(t) &= \frac{\eta_C\Omega}{\omega_C-\mu}\left[1-e^{i(\omega_M-\mu)t}\right]
\end{aligned} \tag{6.46}$$

From Equation 6.46, it can be seen that spin-phonon coupling is still minimized in the same way by choosing the gate time to be integer multiples of $\frac{2\pi}{|\omega_C-\mu|}$.

To evaluate the second order term in the Magnus expansion, we need to evaluate the commutator of the Hamiltonian $\left[\hat{H}\left(t_1\right),\hat{H}\left(t_2\right)\right]$. Note that $\left[\hat{a}_C^\dagger g_1\left(\hat{n},\eta_C\right),\hat{a}_C^\dagger g_1\left(\hat{n},\eta_C\right)\right] =$

$[\hat{a}_C g_1(\hat{n}-1,\eta_C), \hat{a}_C g_1(\hat{n}-1,\eta_C)] = 0$. Thus,

$$\begin{aligned}\left[\hat{H}(t_1), \hat{H}(t_2)\right] = \hbar^2\eta_C^2\bar{\Omega}^2\Big(&e^{i(\omega_C-\mu)t_1 - i(\omega_C-\mu)t_2}\left[\hat{a}_C^\dagger g_1(\hat{n},\eta_C), \hat{a}_C g_1(\hat{n}-1,\eta_C)\right] \\ &+ e^{-i(\omega_C-\mu)t_1 + i(\omega_C-\mu)t_2}\left[\hat{a}_C g_1(\hat{n}-1,\eta_C), \hat{a}_C^\dagger g_1(\hat{n},\eta_C)\right]\Big)\left(\sum_{n=1}^{N}\hat{S}_{x,n}\right)^2\end{aligned} \tag{6.47}$$

Evaluating $\hat{a}_C g_1(\hat{n}-1,\eta_C)\,\hat{a}_C^\dagger g_1(\hat{n},\eta_C)\,|n\rangle$ gives

$$\begin{aligned}\hat{a}_C g_1(\hat{n}-1,\eta_C)\,\hat{a}_C^\dagger g_1(\hat{n},\eta_C)\,|n\rangle &= \sqrt{n+1}\,g_1(n,\eta_C)\,\hat{a}_C g_1(\hat{n}-1,\eta_C)\,|n+1\rangle \\ &= (n+1)\,g_1^2(n,\eta_C)\,|n\rangle\end{aligned} \tag{6.48}$$

Similarly,

$$\hat{a}_C^\dagger g_1(\hat{n},\eta_C)\,\hat{a}_C g_1(\hat{n}-1,\eta_C)\,|n\rangle = n g_1^2(n-1,\eta_C)\,|n\rangle \tag{6.49}$$

Thus, the commutator $\left[\hat{a}_C g_1(\hat{n}-1,\eta_C), \hat{a}_C^\dagger g_1(\hat{n},\eta_C)\right]$ is

$$\begin{aligned}\left[\hat{a}_C g_1(\hat{n}-1,\eta_C), \hat{a}_C^\dagger g_1(\hat{n},\eta_C)\right] &= (\hat{n}+1)\,g_1^2(n,\eta_C) - \hat{n} g_1^2(n-1,\eta_C) \\ &= \frac{e^{-\eta_C^2}}{\hat{n}+1}\left(L_{\hat{n}}^1\left(\eta_C^2\right)\right)^2 - \frac{e^{-\eta_C^2}}{\hat{n}}\left(L_{\hat{n}-1}^1\left(\eta_C^2\right)\right)^2 \\ &= 1 - \eta_C^2(2\hat{n}+1) + \eta_C^4\left(\frac{5}{4}\hat{n}^2 + \frac{5}{4}\hat{n} + \frac{1}{2}\right) + \cdots\end{aligned} \tag{6.50}$$

By rewriting $\left[\hat{a}_C g_1(\hat{n}-1,\eta_C), \hat{a}_C^\dagger g_1(\hat{n},\eta_C)\right] = 1 - G(\hat{n},\eta_C)$, the second order Magnus expansion is

$$\begin{aligned}M_2(t) &= -\frac{1}{2\hbar^2}\int_0^t dt_1 \int_0^{t_1}\left[\hat{H}(t_1), \hat{H}(t_2)\right] dt_2 \\ &= -i\eta_C^2\bar{\Omega}^2\left(1 - G(\hat{n},\eta_C)\right)\left(\sum_{n=1}^{N}\hat{S}_{x,n}\right)^2 \\ &\times \int_0^t dt_1 \int_0^{t_1}\left(\sin\left((\omega_C-\mu)t_2 - (\omega_C-\mu)t_1\right)\right) dt_2 \\ &= i\frac{\eta_C^2\bar{\Omega}^2}{\omega_C-\mu}\left(1 - G(\hat{n},\eta_C)\right)\left(t - \frac{\sin\left((\omega_C-\mu)t\right)}{\omega_C-\mu}\right)\left(\sum_{n=1}^{N}\hat{S}_{x,n}\right)^2\end{aligned} \tag{6.51}$$

Comparing Equations 6.29 and 6.51 shows that the Rabi frequency is transformed as $\bar{\Omega} \rightarrow \sqrt{1 - G\left(\hat{n}, \eta_C\right)}\bar{\Omega}$ when no LDA is employed. This implies that the optimum value of $\bar{\Omega}$ for an intended phase, θ_0, is shifted by a different amount for an ion in a different phonon Fock state. If an ion is in a superposition of phonon Fock states or is in a mixed thermal state, it is impossible to pick a single Rabi frequency that satisfies $\theta_0 = \frac{2\eta_C^2 \bar{\Omega}^2 \pi}{(\omega_C - \mu)|\omega_C - \mu|}$ for more than 1 value of n. The deviations in the phases gained by the different phonon Fock states contribute to errors in the gate.

Other than the deviations of the gate phases for different phonon Fock states, there is another form of error introduced by LDA. Without LDA, it can be observed that higher order Magnus expansions are no longer 0 since $\left[\hat{a}_C g_1\left(\hat{n} - 1, \eta_C\right), G\left(\hat{n}, \eta_C\right)\right] \neq 0$ or $\left[\hat{a}_C^\dagger g_1\left(\hat{n}, \eta_C\right), G\left(\hat{n}, \eta_C\right)\right] \neq 0$. This implies that the third and higher order commutators of the Hamiltonian is non-zero in general. Thus, making the LDA effectively neglects the higher order terms in the Magnus expansion, which contributes to errors in the gate.

To obtain an estimate of the error due to LDA, numerical simulations with the realistic Hamiltonian with and without LDA are performed. The improvement in the fidelity of the output state obtained with LDA is then quantified as the error due to LDA. Details of numerical simulations are found in Section 6.3.

6.2.2 Rotating Wave Approximation

In Section 6.1, 3 RWAs are made. The first RWA is employed when it is assumed that each laser perturbation is only close to resonance to a specific target transition and other off-resonant couplings can be ignored to arrive at Equation 6.6. A second RWA is employed which neglects the fast rotating terms $e^{\pm(2\omega_l + \mu)t}$ in Equation 6.11 to reach Equation 6.12. A third RWA is applied to Equation 6.19 to arrive at Equation 6.20.

The error from the first RWA may not be intrinsic to this qudit entangling gate, as depending on the physical system, there may be no need to employ the first RWA. An example would be the case where polarization control only allows coupling of a laser perturbation to the target transition and is forbidden by selection rule to the other transitions. The third RWA would typically introduce a much larger error as compared to the second RWA, as the laser detuning is usually much smaller than the transition frequency in a trapped ion system $\mu \ll \omega_l$. Thus, this study primarily investigates the error introduced by the third RWA as it is the one that is intrinsic to the formulation of this qudit entangling gate and introduces the most error.

Numerical simulations are carried out to quantify the error due to RWA. Since it is

difficult to obtain an analytical form of the Hamiltonian with RWA without LDA (see Equation 6.73), the improvement to the fidelity with RWA is approximated by increasing the frequencies of the motional states and laser frequency detunings. Let the laser detuning be rewritten as

$$\mu = \omega_C + \delta \tag{6.52}$$

where δ is the detuning from the centre-of-mass mode frequency. The frequencies of other normal modes can also be rewritten as

$$\omega_m = \omega_C - \Delta\omega_m \tag{6.53}$$

where $\Delta\omega_m$ is the difference between the frequency of the centre-of-mass mode with the m^{th} motional mode. By increasing ω_C while keeping δ and $\Delta\omega_m$ the same, the approximation from RWA becomes more accurate while keeping the dynamics of other error sources considered in this article the same. Thus, the error due to RWA is quantified by the improvement of the fidelity of the output state when ω_C is increased significantly with fixed δ and $\Delta\omega_m$.

6.2.3 Spectator Phonon Modes

To arrive at Equation 6.20 from Equation 6.19, there is another assumption that is made before employing a RWA. It is assumed that the laser detuning is tuned close to only one normal mode frequency, which is the centre-of-mass mode, and sufficiently far off-resonant from the other normal mode frequencies so that they can be neglected with RWA. Assuming that there are 2 ions, which is the minimum number of ions required for this gate, there is an additional normal mode, being the tilt mode [52]. The full expression for $k\hat{x}'_n$ from Equation 6.18 is then

$$k\hat{x}'_n = \eta_C \left(e^{i\omega_C t}\hat{a}_C^\dagger + e^{-i\omega_C t}\hat{a}_C\right) - (-1)^n \eta_T \left(e^{i\omega_T t}\hat{a}_T^\dagger + e^{-i\omega_T t}\hat{a}_T\right) \tag{6.54}$$

where we have defined $\eta_T = \eta_{T,1} = -\eta_{T,2}$ and the subscript T denotes the tilt mode. The Hamiltonian with LDA and RWA is then

$$\begin{aligned}\hat{H} \approx \sum_{n=1}^{2} \hbar\hat{\Omega}\Big[&\eta_C \left(e^{i(\omega_C-\mu)t-i\phi_M}\hat{a}_C^\dagger + e^{-i(\omega_C-\mu)t+i\phi_M}\hat{a}_C\right) \\ &- (-1)^n \eta_T \left(e^{i(\omega_T-\mu)t-i\phi_M}\hat{a}_T^\dagger + e^{-i(\omega_T-\mu)t+i\phi_M}\hat{a}_T\right)\Big]\hat{S}_{\phi_S}\end{aligned} \tag{6.55}$$

The additional term introduced by the tilt mode in Equation 6.55 causes deviation from the ideal Hamiltonian and thus introduces error to the operation. Improvement to the

output state fidelity when the realistic Hamiltonian is simulated without the tilt mode is quantified as the error due to a spectator phonon mode.

6.2.4 Photon Scattering

Raman transition is a common method to drive the transition between levels for the Mølmer-Sørensen gate [15, 50]. Employing Raman transitions for the target transitions in this qudit entangling gate, some finite probability of photon scattering events is inevitable, as discussed in Section 5.2.3. To assess the error due to photon scattering events, it is imperative to compute the probability of a scattering event occurring within the gate time. Employing the same method in Section 5.2.3, any scattering event is assumed to completely decohere the quantum system, which gives an upper estimate of the error from photon scattering.

In this section, the photon scattering probability is computed assuming $^{137}Ba^{+}$ as the ion species and encoding scheme as shown in Figure 6.1. The Raman beam frequencies applied to drive the entangling gate for a 3 and 5-level system is also shown in Figure 6.1. From Equation 5.13, the total scattering rate in terms of the population in the encoded states can be derived to be (see Appendix B)

$$R_{SE} = \sum_i \sum_j \sum_l \gamma_i P_l \frac{\xi_j^2}{4\hbar^2 \left(\omega_R - \omega_i\right)^2} |\langle i|\hat{d}\cdot\hat{\epsilon}_j|l\rangle|^2 \tag{6.56}$$

where P_l is the population of the $|l\rangle$ state, ω_R is the frequency of the Raman beam and ω_i is the transition frequency between a state in the $6S$ level and one in the $|i\rangle$ state, which is either the $6P_{1/2}$ state or $6P_{3/2}$ state in this case.

For the case with pure polarizations, i.e. $|r_+| = 1$ for Raman beams 1 and 2, $|r_-| = 1$ for Raman beams 3 and 4, $|b_0| = 1$ for Raman beam 0 as indexed in Figure 6.1a. Assuming that $\xi_r = \xi_b = \bar{\xi}$ for all the Raman beams, we have

$$\begin{aligned} \sum_j \left(r_{-,j}\xi_{r,j}\right)^2 &= 2\bar{\xi}^2 \\ \sum_l \left(r_{+,l}\xi_{r,l}\right)^2 &= 2\bar{\xi}^2 \\ \sum_k \left(b_{0,k}\xi_{b,k}\right)^2 &= \bar{\xi}^2 \end{aligned} \tag{6.57}$$

Using Equation 5.14, the summation of the total scattering rate is then

$$\begin{aligned} R_{SE} &= \sum_l P_l R_{SE,l} \\ &= \sum_l P_l \frac{|\langle 6P, L=1|\hat{d}|6S, L=0\rangle|^2}{4\hbar^2} \frac{5}{3} \left[\frac{\gamma_{1/2}}{\Delta_{1/2}^2} + 2\frac{\gamma_{3/2}}{\Delta_{3/2}^2} \right] \hat{\xi}^2 \end{aligned} \tag{6.58}$$

Since $\sum_l P_l = 1$,

$$R_{SE} = \frac{|\langle 6P, L=1|\hat{d}|6S, L=0\rangle|^2}{4\hbar^2} \frac{5}{3} \left[\frac{\gamma_{1/2}}{\Delta_{1/2}^2} + 2\frac{\gamma_{3/2}}{\Delta_{3/2}^2} \right] \hat{\xi}^2 \tag{6.59}$$

From Equation 6.21, the Rabi frequency for each transition has to satisfy $\sqrt{2}\bar{\Omega} = \Omega_0 = \Omega_1$. The relation between $\bar{\xi}$ with $\bar{\Omega}$ can then be derived from Equation 5.16 to be

$$\bar{\xi}^2 = \frac{4\sqrt{6}\hbar^2\bar{\Omega}}{|\langle 6P, L=1|\hat{d}|6S, L=0\rangle|^2} \left(\frac{\Delta_{1/2}\Delta_{3/2}}{\Delta_{1/2} - \Delta_{3/2}} \right) \tag{6.60}$$

From Equations 6.60 and 6.59, the scattering rate can be rewritten as

$$R_{SE} = \frac{10}{\sqrt{6}} \bar{\Omega} \left[\frac{\gamma_{1/2}}{\Delta_{1/2}^2} + 2\frac{\gamma_{3/2}}{\Delta_{3/2}^2} \right] \frac{\Delta_{1/2}\Delta_{3/2}}{\Delta_{1/2} - \Delta_{3/2}} \tag{6.61}$$

The scattering probability within the gate time is thus

$$\begin{aligned} P_{SE} &= R_{SE} t_{gate} \\ &= \frac{10}{\sqrt{6}} \bar{\Omega} \left[\frac{\gamma_{1/2}}{\Delta_{1/2}^2} + 2\frac{\gamma_{3/2}}{\Delta_{3/2}^2} \right] \frac{\Delta_{1/2}\Delta_{3/2}}{\Delta_{1/2} - \Delta_{3/2}} t_{gate} \end{aligned} \tag{6.62}$$

where t_{gate} is the gate time.

For 5-level qudits, similar derivation methods are followed to arrive at the photon scattering probability. Let $\xi_r = \xi_b = \bar{\xi}$ for the transitions $|1\rangle \leftrightarrow |2\rangle$ and $|2\rangle \leftrightarrow |3\rangle$. From Equation 6.21, the requirement for the Rabi frequencies is $\bar{\Omega} = \Omega_0/2 = \Omega_3/2 = \Omega_1/\sqrt{6} = \Omega_2/\sqrt{6}$. From Equation 5.21, this implies that

$$\frac{\xi_{3/4/5/6}}{\xi_{1/2/7/8}} = 3 \tag{6.63}$$

where ξ_i is the electric field amplitude of the i^{th} Raman beam as shown in Figure 6.1b. Thus,

$$\begin{aligned}\sum_j \left(r_{-,j}\xi_{r,j}\right)^2 &= \frac{20}{9}\bar{\xi}^2 \\ \sum_l \left(r_{+,l}\xi_{r,l}\right)^2 &= \frac{20}{9}\bar{\xi}^2 \\ \sum_k \left(b_{0,k}\xi_{b,k}\right)^2 &= \bar{\xi}^2\end{aligned} \tag{6.64}$$

With pure Raman beam polarizations, the expression of $\bar{\xi}^2$ in terms of $\bar{\Omega}$ can be derived from Equation 5.21 to be

$$\bar{\xi}^2 = \frac{12\sqrt{6}\hbar^2\bar{\Omega}}{|\langle\, 6P, L=1||\vec{d}||\, 6S, L=0\rangle|^2}\left(\frac{\Delta_{1/2}\Delta_{3/2}}{\Delta_{1/2}-\Delta_{3/2}}\right) \tag{6.65}$$

Using Equations 5.20, 6.64, and 6.65, the photon scattering probability is derived to be

$$P_{SE} = \frac{49\sqrt{6}}{9}\bar{\Omega}\left(\frac{\gamma_{1/2}}{\Delta_{1/2}^2} + 2\frac{\gamma_{3/2}}{\Delta_{3/2}^2}\right)\frac{\Delta_{1/2}\Delta_{3/2}}{\Delta_{1/2}-\Delta_{3/2}}t_{gate} \tag{6.66}$$

In the 2-qudit entanglement, the probability of zero scattering event for both ions is

$$P(\text{no scattering}) = (1-P_{SE})^2 \approx 1 - 2P_{SE} \tag{6.67}$$

Thus, accounting for error due to photon scattering, the fidelity of the gate without photon scattering would be transformed by

$$F \to F\,(1-P_{SE})^2 \tag{6.68}$$

The error due to photon scattering can be estimated in a straightforward manner by taking $2P_{SE}$ to be the error.

6.2.5 Imperfect Cooling of Ions

Realistically, it is difficult to perfectly cool the ion to the absolute phonon ground state [15]. An imperfectly cooled ion can be described to be in a mixed thermal state with

a spread in distribution in the different phonon Fock states [54]. A thermal state has a probability distribution of the phonon Fock states in the form

$$P_n = \frac{\bar{n}^n}{(\bar{n}+1)^{n+1}} \tag{6.69}$$

where $\bar{n}$ is the average phonon number. As shown in Section 6.2.1, a spread in the probability distribution leads to error in the gate.

In order to quantify the error due to imperfect cooling of ions, the improvement in the fidelity of the output state when $\bar{n}$ is set to zero is regarded as the value of error.

6.2.6 Motional Heating of Ions

In a realistic trapped ion system, there are external sources of heat that can heat up the vibrational motion [28]. If this heating event happens during the gate time, the trajectory of the 2-qudit state in the motional phase space would be distorted, which introduces errors to the gate. Analytical form of the error introduced for the qubit version of the Mølmer-Sørensen gate has also been derived [28]. For the qudit version, we rely on numerical simulations to obtain an upper bound of the error.

To obtain an upper bound of the error due to motional heating of ions, the ion phonon state is increased by one when the motional phase space displacement is maximal, from which the fidelity, F_{heat}, is computed. The overall fidelity is then computed by

$$F = (1 - P_{heat})\, F_0 + P_{heat} F_{heat} \tag{6.70}$$

where P_{heat} is the probability that a phonon hop happens due to motional heating from the environment during the gate time and F_0 is the fidelity when no phonon hop happens. The error due to motional heating of ions is then quantified as $F_0 - F$.

6.2.7 Magnetic field noise

As described in Section 5.2.1, when there are deviations of the magnetic field from the ideal value, the Hamiltonian matrix is modified with additional diagonal terms as shown in Equation 5.6. This deviation from the ideal Hamiltonian introduces error to our gate.

The error due to magnetic field noise is quantified from numerical simulations by taking the difference of the output fidelity with and without $\hat{H}_{noise}$ as defined in Equation 5.6.

6.3 Numerical Simulations for Qudit Entangling Gate

The Scrhödinger's equation as shown in Equation 5.23 is used to evaluate the evolution of a state under a certain Hamiltonian. The MATLAB function ode113 is used to numerically evaluate the time-evolution of an input state.

To account for the error sources under consideration, a realistic Hamiltonian has to be rederived from Equation 6.14. For simplicity, the values of spin and motional phases are chosen to be zero, $\phi_S = \phi_M = 0$. This gives

$$\begin{aligned}\hat{H} = &\sum_{n=1}^{N}\sum_{l=0}^{d-1}\hbar\bar{\Omega}\sqrt{s(s+1)-l'(l'+1)}\cos(\mu t)\\ &\times\left[i\,(-1)^l\,e^{-i(-1)^l k\hat{x}'_n}|l+1\rangle\langle l|_n - i\,(-1)^l\,e^{i(-1)^l k\hat{x}'_n}|l\rangle\langle l+1|_n\right]\end{aligned} \tag{6.71}$$

Due to computational limitations, the simulations is done with $N = 2$. Two normal modes are thus present for a chosen axis. Assuming that the transverse mode is chosen as the phonon bus, the two modes are the centre-of-mass mode and tilt mode. Substituting Equation 6.54 into Equation 6.71 gives

$$\begin{aligned}\hat{H} = &\sum_{n=1}^{2}\sum_{l=0}^{d-1}\hbar\Omega\sqrt{s(s+1)-l'(l'+1)}\cos(\mu t)\\ &\left[i(-1)^l e^{-i(-1)^l(\eta_C(e^{i\omega_C t}\hat{a}_C^\dagger+e^{-i\omega_C t}\hat{a}_C)-(-1)^n\eta_T(e^{i\omega_T t}\hat{a}_T^\dagger+e^{-i\omega_T t}\hat{a}_T))}|l+1\rangle\langle l|_n\right.\\ &\left.-i(-1)^l e^{i(-1)^l(\eta_C(e^{i\omega_C t}\hat{a}_C^\dagger+e^{-i\omega_C t}\hat{a}_C)-(-1)^n\eta_T(e^{i\omega_T t}\hat{a}_T^\dagger+e^{-i\omega_T t}\hat{a}_T))}|l\rangle\langle l+1|_n\right]\end{aligned} \tag{6.72}$$

which is the Hamiltonian without LDA, without the RWA under consideration, and with a spectator phonon mode. To account for magnetic field noise, $\hat{H}_{noise}$ as defined in Equation 5.6 is added to Equation 6.72, giving

$$\begin{aligned}\hat{H} = &\sum_{n=1}^{2}\sum_{l=0}^{d-1}\hbar\Omega\sqrt{s(s+1)-l'(l'+1)}\cos(\mu t)\\ &\left[i(-1)^l e^{-i(-1)^l(\eta_C(e^{i\omega_C t}\hat{a}_C^\dagger+e^{-i\omega_C t}\hat{a}_C)-(-1)^n\eta_T(e^{i\omega_T t}\hat{a}_T^\dagger+e^{-i\omega_T t}\hat{a}_T))}|l+1\rangle\langle l|_n\right.\\ &\left.-i(-1)^l e^{i(-1)^l(\eta_C(e^{i\omega_C t}\hat{a}_C^\dagger+e^{-i\omega_C t}\hat{a}_C)-(-1)^n\eta_T(e^{i\omega_T t}\hat{a}_T^\dagger+e^{-i\omega_T t}\hat{a}_T))}|l\rangle)\langle l+1|_n\right]+\hat{H}_{noise}\end{aligned} \tag{6.73}$$

Equation 6.73 is used to numerically evolve an initial state in the MATLAB simulations. Since the internal electronic states are only of concern and not the phonon state at the

output, the phonon states after the gate are removed by partial tracing the density operator of the output state. The fidelity is then computed from the ideal (electronic) output state with

$$F = \langle \psi_{ideal} | \mathrm{Tr}_{phonon}(\hat{U}(t_{gate})\rho_0 \hat{U}^\dagger(t_{gate})) | \psi_{ideal} \rangle \tag{6.74}$$

where $|\psi_{ideal}\rangle$ is the ideal output state, ρ_0 is the initial density matrix, $\mathrm{Tr}_{phonon}(\rho)$ is the partial trace over the normal-mode phonon states of an arbitrary density matrix ρ.

To account for the error due to imperfect cooling of ions, the input density matrix is in the form

$$\rho_0 = \sum_m \sum_n P_C(m) P_T(n) |\psi_0, m, n\rangle\langle\psi_0, m, n| \tag{6.75}$$

where $P(x)$ is the phonon Fock state population for the $|x\rangle$ Fock state, subscripts C and T again refer to the centre-of-mass and tilt modes respectively, and $|\psi_0\rangle$ is the input internal state of the ions.

The optimal strategy for a fast simulation is to evaluate the time evolution operator from Schrödinger's equation and compute the fidelity according to Equation 6.74 from the initial density matrix. However, this method is too memory-intensive for us, and an alternative approach is used. First, the evolution of each pure state $|\psi_0, m, n\rangle$ is computed by numerically solving Schrödinger's equation. The output fidelity of each of the pure state is then weighted by the phonon populations, $P_C(m)P_T(n)$:

$$\begin{aligned} F_{m,n} &= P_C(m)P_T(n)\langle\psi_{ideal}|\mathrm{Tr}_{phonon}\left(\hat{U}(t)|\psi_0, m, n\rangle\langle\psi_0, m, n|\hat{U}^\dagger(t)\right)|\psi_{ideal}\rangle \\ &= P_C(m)P_T(n)\sum_{m'}\sum_{n'}\langle\psi_{ideal}|\langle m', n'|\hat{U}(t)|\psi_0, m, n\rangle\langle\psi_0, m, n|\hat{U}^\dagger(t)|m', n'\rangle|\psi_{ideal}\rangle \end{aligned} \tag{6.76}$$

The weighted fidelities are then summed to obtain the overall fidelity

$$\begin{aligned} F &= \sum_m \sum_n F_{m,n} \\ &= \langle\psi_{ideal}|\sum_{m'}\sum_{n'}\langle m', n'|\hat{U}(t)\sum_m\sum_n P_C(m)P_T(n)|\psi_0, m, n\rangle\langle\psi_0, m, n|\hat{U}^\dagger(t)|m', n'\rangle|\psi_{ideal}\rangle \end{aligned} \tag{6.77}$$

which is equivalent to Equation 6.74. It is impossible to numerically sum over the infinite series of Fock states in the simulations. Thus, the number of allowed Fock states for the

centre-of-mass and tilt modes are chosen such that they are large enough for fidelity results accurate up to the fourth decimal place. With $\bar{n}_C = 0.1$ and $\bar{n}_T = 0$, 20 and 2 allowed Fock states for the centre-of-mass and tilt modes are found to be sufficiently accurate. To further speed up the simulations, states where $P_C(m)P_T(n) < 10^{-5}$ are ignored.

In Section 6.2.1, it can be seen that the optimum Rabi frequency for a certain phonon Fock state is shifted by

$$\bar{\Omega} = \frac{\bar{\Omega}_{LDA}}{\sqrt{1 - G\left(\hat{n}, \eta_C\right)}} \tag{6.78}$$

where $\bar{\Omega}_{LDA}$ is the optimum Rabi frequency for the intended gate phase with LDA. For input states with a superposition of or mixed phonon states, the fidelity with errors only from the shifted geometric phase from the LDA case can be written as

$$F = \sum_{n=0}^{\infty} P_n |\langle\psi_0| e^{i(\theta_n - \theta_{ideal})\left(\sum_{n=1}^{N} \hat{S}_{x,n}\right)^2} |\psi_0\rangle|^2. \tag{6.79}$$

Define

$$f(\Delta\theta_n) = |\langle\psi_0| e^{i\Delta\theta_n\left(\sum_{n=1}^{N} \hat{S}_{x,n}\right)^2} |\psi_0\rangle|^2, \tag{6.80}$$

where $\Delta\theta_n = \theta_n - \theta_{ideal}$. For small $\Delta\theta_n$, $f(\Delta\theta_n)$ can be approximated with Taylor series expansion

$$f(\Delta\theta_n) = \sum_{l=0}^{\infty} \frac{d^l f(0)}{d\Delta\theta_n^l} \frac{\Delta\theta_n^l}{l!}. \tag{6.81}$$

Since $f(0) = 1$ is a maximum point, $\frac{df(0)}{d\Delta\theta_n} = 0$. Keeping the largest non-zero term,

$$f(\Delta\theta_n) \approx 1 + \frac{d^2 f(0)}{d\Delta\theta_n^2} \frac{\Delta\theta_n^2}{2}. \tag{6.82}$$

To maximize the fidelity,

$$\begin{aligned} \frac{dF}{d\Omega} &= \sum_{n=0}^{\infty} P_n \frac{df(\Delta\theta_n)}{d\Omega} \\ &\approx \sum_{n=0}^{\infty} P_n \Delta\theta_n \frac{d^2 f}{d\Delta\theta_n^2}(0) \frac{d\Delta\theta_n}{d\Omega} = 0, \end{aligned} \tag{6.83}$$

which implies

$$\sum_{n=0}^{\infty} P_n((1-G(n,\eta))\Omega^2 - \Omega_{LDA}^2)(1-G(n,\eta))\Omega = 0. \tag{6.84}$$

The solution where $\Omega = 0$ does not satisfy the condition $\Delta\theta_n \approx 0$. Thus, the optimum value of the Rabi frequency is approximately

$$\Omega \approx \Omega_{LDA}\sqrt{1 + \frac{\sum_{n=0}^{\infty} P_n G(n,\eta)(1-G(n,\eta))}{\sum_{n=0}^{\infty} P_n (1-G(n,\eta))^2}}. \tag{6.85}$$

Since the objective is to obtain the error due to experimental imperfections and not inaccurate parameters, the Rabi frequency in Equation 6.85 is used for the simulations.

To estimate the upper bound of the error due to motional heating, the centre-of-mass phonon states are transformed as $|m\rangle \rightarrow |m+1\rangle$ at time $t = t_{gate}/2$ in order to compute F_{heat} as defined in Section 6.2.6.

With these, the simulations have accounted for the error sources under consideration except for photon scattering, which is obtained from manual calculations as outlined in Section 6.2.4. To simulate the output fidelity with LDA, the terms $e^{\pm i(-1)^l(\eta_C(e^{i\omega_C t}\hat{a}_C^\dagger + e^{-i\omega_C t}\hat{a}_C) - (-1)^n\eta_T(e^{i\omega_T t}\hat{a}_T^\dagger + e^{-i\omega_T t}\hat{a}_T))}$ in Equation 6.73 is transformed to

$$\begin{aligned} & e^{\pm i(-1)^l(\eta_C(e^{i\omega_C t}\hat{a}_C^\dagger + e^{-i\omega_C t}\hat{a}_C) - (-1)^n\eta_T(e^{i\omega_T t}\hat{a}_T^\dagger + e^{-i\omega_T t}\hat{a}_T))} \\ \rightarrow\ & 1 \pm i(-1)^l(\eta_C(e^{i\omega_C t}\hat{a}_C^\dagger + e^{-i\omega_C t}\hat{a}_C) - (-1)^n\eta_T(e^{i\omega_T t}\hat{a}_T^\dagger + e^{-i\omega_T t}\hat{a}_T)) \end{aligned} \tag{6.86}$$

and the output fidelities are evaluated with the new Hamiltonian. To estimate output fidelities with RWA, ω_C is increased to $2\pi \times 50\,\text{MHz}$ while keeping δ and $\Delta\omega_m$ fixed. Simulations are then carried out with the Hamiltonian in Equation 6.73. To ensure that the fideltiy has converged sufficiently, ω_C is further increased to $2\pi \times 60\,\text{MHz}$ and the computed fidelity is ensured to be within ± 0.0001 from the fidelity obtained with $\omega_C = 2\pi \times 50\,\text{MHz}$. For the simulations without a spectator phonon mode, η_T is set to zero.

6.4 Error Estimation Results

The simulations and errors are evaluated for $^{137}Ba^+$ ions. To model a realistic ion trap, the parameters used are $\eta_C = 0.0507$, $\omega_C = 2\pi \times 2\,\text{MHz}$, $\omega_T = 2\pi \times 1.8\,\text{MHz}$, $\mu = 2\pi \times 2.01\,\text{MHz}$, $K = 1$ and thus a gate time of $t_{gate} = \frac{2\pi}{|\omega_C - \mu|} = 100\,\mu\text{s}$. We set $\theta_0 = -\frac{\pi}{4}$ as an example. This value of θ_0 is chosen as it results in a non-trivial entanglement result

Error Source	3-level Qudit	5-level Qudit**
LDA	3×10^{-4}	3.0×10^{-3}
RWA	4×10^{-4}	2.6×10^{-3}
Spectator mode	2.7×10^{-3}	1.09×10^{-2}
Photon scattering*	3.0×10^{-3}	9.7×10^{-3}
Imperfect cooling	$< 10^{-4}$	$< 10^{-4}$
Motional heating	3.3×10^{-3}	4.6×10^{-3}
Magnetic field noise	$< 10^{-4}$	$< 10^{-4}$

Table 6.1: Error estimate from error sources for the qudit entangling gate. Each error estimate except for photon scattering is obtained by the increase in fidelity when the error source is removed from the simulation. *Error for photon scattering listed here is $2P_{SE}$, where P_{SE} is the photon scattering probability as defined in text. **The error estimates for $d = 5$ listed here are obtained for the case without the large error from off-resonant frequencies (see text in Section 6.4 and Appendix C).

that is not replicable by a single qubit MS gate for a 3-level qudit system. For example, $\theta_0 = -\frac{\pi}{2}$ acting on the state $|2, 2\rangle$ of a 3-level qudit system can be shown to give the same output as a qubit MS gate acting on the appropriate transition levels (see Figure 6.2b at $t = 200\,\mu$s). We kept $\theta_0 = -\frac{\pi}{4}$ for the 5-level qudit for simplicity. The motional heating rate is assumed to be $100\,\text{s}^{-1}$, which is a realistic estimate [55]. The error due to each error sources is shown in Table 6.1.

The fidelity obtained with all the error sources taken into consideration for $d = 3$ is 0.9910. For $d = 5$, off-resonant transition frequencies distorts the Hamiltonian significantly from the encoding scheme in Figure 6.1b, and results in a fidelity much smaller than 1, which is $F = 0.0296$ (see Appendix C). It is noted that this error is present due to symmetry of the chosen encoding scheme in Figure 6.1b, and may be overcome with other encoding schemes. Without this error, an overall fidelity of 0.9719 is obtained for $d = 5$ with these parameters. From Table 6.1, the spectator phonon mode, photon scattering and motional heating of ions are the major sources of error.

To reduce the error due to a spectator phonon mode, a direct way is to tune the trap parameters such that the spectator mode is detuned farther from the desired phonon mode frequency. This would reduce the contribution to the state evolution from the spectator modes. To eliminate the spectator mode contribution without the need to tune the trap parameters, clever pulse shaping could be performed which removes spin-phonon coupling of spectator modes, which is shown for the qubit case [56]. Assuming that spectator mode error can be eliminated by clever pulse shaping techniques, the fidelity for this 3-level

qudit entangling gate can be increased to 0.9937. Neglecting the error due to off-resonant frequencies again, the fidelity for the 5-level qudit entangling gate is 0.9828 if the error from spectator mode can be overcome. For the photon scattering error and error due to motional heating, it is noted that they are overestimations. More elaborate estimations of these sources of error are likely to lower them.

Overall, it is possible to achieve close to 99.25% for 3-level qudits with this generalized entangling gate. However, it is noted that the photon scattering error and motional heating error are crude overestimates in this thesis. The achievable fidelity may exceed 99.25% once more careful considerations of the two error sources are taken into account. For $d \geq 5$, this gate is not applicable for our encoding scheme using $^{137}Ba^{+}$ due to error from off-resonant frequencies.

Chapter 7

Conclusion

Two main studies are presented in this thesis. The first is on investigating tolerable imperfections of a quadrupole blade ion trap while the second is on the formulations and error estimations of qudit gates. For the first study, it is found that geometric misalignment that are axially symmetric are not major issues as the excess micromotions stem from a mismatch in the DC and RF null lines, which can be corrected as long as variable DC bias voltages are incorporated into the trap design. Geometric misalignment that are axially asymmetric introduce excess micromotion in the axial direction, which cannot be compensated with DC bias voltages as there is no RF null in the axial direction. Of the misalignment which are axially asymmetric, the more sensitive ones are axial translation and in-plane rotation of a blade electrode. For electrical imperfections, cis-amplitude mismatch and cis-phase shift of the RF voltages do not cause excess micromotion. Trans-amplitude mismatch can be corrected with DC biasing voltages similar to axially-symmetric geometric misalignment. Only trans-phase shift is critical in terms of electrical imperfections within our considerations.

Error estimations for the single qudit gate set which is composed of the generalized Pauli operators, generalized $\pi/8$ gate, and QFT are investigated for our proposed encoding schemes for $^{137}Ba^{+}$. The largest errors among the set of single qudit gates is the QFT gate. Conservative estimates give achievable QFT gate fidelities of 99.98% and 99.8% for 3 and 5-level qudits respectively. A qudit version of the Mølmer-Sørensen gate is formulated and presented. The estimated errors for the qudit Mølmer-Sørensen gate is 99.10% for 3-level qudits. The 5-level qudit Mølmer-Sørensen gate fails due to unwanted transitions from off-resonant frequencies for our encoding scheme. The failure stems from the symmetry in our encoding scheme which causes unwanted resonant transitions from the "off-resonant" frequencies. However, this is not a fundamentally limiting factor as

there may be other encoding schemes which avoids the symmetry which brought about this error. Alternatively, other qudit entangling gates could be devised which averts this error. The qudit Mølmer-Sørensen gate does not quite meet the fault tolerance threshold of 99.25% (for qubits) as reported in Ref. [18]. However, the threshold is expected to be more forgiving for higher dimensional qudits. In addition, it is acknowledged that 2 of the major sources of error from the calculations are crude overestimations. Future work is to be done to properly account for these sources of error and the fidelity for the 3-level qudit Mølmer-Sørensen gate is expected to be much closer or exceed the 99.25% figure.

References

[1] P.W. Shor. Polynomial-time algorithms for prime factorizationand discrete logarithms on a quantum computer. *SIAM J. COMPUT.*, 26(5):1484–1509, 1997.

[2] B. P. Lanyon, M. Barbieri, M. P. Almeida, T. Jennewein, T. C. Ralph, K. J. Resch, J. L. O'Brien G. J. Pryde, A. Gilchrist, and A. G. White. Simplifying quantum logic using higher-dimensional Hilbert spaces. *Nature Physics*, 5:134–140.

[3] A. Fedorov, M. Baur L. Steffen, M. P. da Silva, and A. Wallraff. Implementation of a Toffoli gate with superconducting circuits. *Nature*, 481:170–172, 2011.

[4] V. Parasa and M. Perkowski. Quantum phase estimation using multivalued logic. In *2011 41st IEEE International Symposium on Multiple-Valued Logic*, pages 224–229, May 2011.

[5] H. Häffner, C.F. Roos, and R. Blatt. Quantum computing with trapped ions. *Physics Reports*, 469(4):155 – 203, 2008.

[6] R. Ozeri. The trapped-ion qubit tool box. *Contemporary Physics*, 52(6):531–550, 2011.

[7] P. Schindler, D. Nigg, T. Monz, J. T. Barreiro, E. Martinez, S. X. Wang, S. Quint, M. F. Brandl, V. Nebendahl, C. F. Roos, M. Chwalla, M. Hennrich, and R. Blatt. A quantum information processor with trapped ions. *New Journal of Physics*, 15(12):123012, dec 2013.

[8] G. Pagano, P. W. Hess, H. B. Kaplan, W. L. Tan, P. Richerme, P. Becker, A. Kyprianidis, J. Zhang, E. Birckelbaw, M. R. Hernandez, Y. Wu, and C. Monroe. Cryogenic trapped-ion system for large scale quantum simulation. *Quantum Science and Technology*, 4(1):014004, oct 2018.

[9] D. J. Berkeland, J. D. Miller, J. C. Bergquist, W. M. Itano, and D. J. Wineland. Minimization of ion micromotion in a paul trap. *Journal of Applied Physics*, 83(10):5025–5033, 1998.

[10] S. Olmschenk. *QUANTUM TELEPORTATION BETWEEN DISTANT MATTER QUBITS*. PhD thesis, University of Michigan, 2009.

[11] K. G. Johnson, J. D. Wong-Campos, A. Restelli, K. A. Landsman, B. Neyenhuis, J. Mizrahi, and C. Monroe. Active stabilization of ion trap radiofrequency potentials. *Review of Scientific Instruments*, 87(5):053110, 2016.

[12] C. J. Foot, D. Trypogeorgos, E. Bentine, A. Gardner, and M. Keller. Two-frequency operation of a paul trap to optimise confinement of two species of ions. *International Journal of Mass Spectrometry*, 430:117 – 125, 2018.

[13] J. Chiaverini, R. B. Blakestad, J. Britton, J. D. Jost, C. Langer, D. Leibfried, R. Ozeri, and D. J. Wineland. Surface-electrode architecture for ion-trap quantum information processing. *Quantum Information & Computation*, 5:419–439, 09 2005.

[14] S. Seidelin, J. Chiaverini, R. Reichle, J. J. Bollinger, D. Leibfried, J. Britton, J. H. Wesenberg, R. B. Blakestad, R. J. Epstein, D. B. Hume, W. M. Itano, J. D. Jost, C. Langer, R. Ozeri, N. Shiga, and D. J. Wineland. Microfabricated surface-electrode ion trap for scalable quantum information processing. *Phys. Rev. Lett.*, 96:253003, Jun 2006.

[15] J. P. Gaebler, T. R. Tan, Y. Lin, Y. Wan, R. Bowler, A. C. Keith, S. Glancy, K. Coakley, E. Knill, D. Leibfried, and D. J. Wineland. High-fidelity universal gate set for $^{9}Be^{+}$ ion qubits. *Phys. Rev. Lett.*, 117:060505, Aug 2016.

[16] Amir Mohammadi, Joschka Wolf, Artjom Krükow, Markus Deiß, and Johannes Hecker Denschlag. Minimizing rf-induced excess micromotion of a trapped ion with the help of ultracold atoms. *Applied Physics B*, 125(7):122, Jun 2019.

[17] N. Herschbach, K. Pyka, J. Keller, and T. E. Mehlstäubler. Linear paul trap design for an optical clock with coulomb crystals. *Applied Physics B*, 107(4):891–906, Jun 2012.

[18] A. G. Fowler, M. Mariantoni, J. M. Martinis, and A. N. Cleland. Surface codes: Towards practical large-scale quantum computation. *Phys. Rev. A*, 86:032324, Sep 2012.

[19] E. T. Campbell. Enhanced fault-tolerant quantum computing in d-level systems. *Phys. Rev. Lett.*, 113:230501, Dec 2014.

[20] R. S. Andrist, J. R. Wootton, and H. G. Katzgraber. Error thresholds for abelian quantum double models: Increasing the bit-flip stability of topological quantum memory. *Phys. Rev. A*, 91:042331, Apr 2015.

[21] J. Randall, S. Weidt, E. D. Standing, K. Lake, S. C. Webster, D. F. Murgia, T. Navickas, K. Roth, and W. K. Hensinger. Efficient preparation and detection of microwave dressed-state qubits and qutrits with trapped ions. *Phys. Rev. A*, 91:012322, Jan 2015.

[22] C. Senko, P. Richerme, J. Smith, A. Lee, I. Cohen, A. Retzker, and C. Monroe. Realization of a quantum integer-spin chain with controllable interactions. *Phys. Rev. X*, 5:021026, Jun 2015.

[23] Ashok Muthukrishnan. Multivalued logic gates for quantum computation. *Phys. Rev. A*, 62, 10 2000.

[24] A. B. Klimov, R. Guzmán, J. C. Retamal, and C. Saavedra. Qutrit quantum computer with trapped ions. *Phys. Rev. A*, 67:062313, Jun 2003.

[25] Brian Mischuck and Klaus Mølmer. Qudit quantum computation in the jaynes-cummings model. *Phys. Rev. A*, 87:022341, Feb 2013.

[26] MingXing Luo and XiaoJun Wang. Universal quantum computation with qudits. *Science China Physics, Mechanics & Astronomy*, 57(9):1712–1717, Sep 2014.

[27] J. I. Cirac and P. Zoller. Quantum computations with cold trapped ions. *Phys. Rev. Lett.*, 74:4091–4094, May 1995.

[28] A. Sørensen and K. Mølmer. Entanglement and quantum computation with ions in thermal motion. *Phys. Rev. A*, 62:022311, Jul 2000.

[29] V. N. Gheorghe F. G. Major and G. Werth. *Charged Particle Traps Physics and Techniques of Charged Particle Field Confinement*. Springer, 2005.

[30] H. Reid. 18.305 lecture notes: Stability of mathieus equation via classical and rg methods, 2015. Retrieved from http://homerreid.com/teaching/18.305/Notes/MathieuStability.pdf.

[31] R. Cosson, G. Vernizzi, and X. Yang. Mathieu functions and numerical solutions of the mathieu equation. In *2009 IEEE International Workshop on Open-source Software for Scientific Computation (OSSC)*, pages 3–10, Sep. 2009.

[32] S. Debnath. *A Programmable Five Qubit Quantum Computer Using Trapped Atomic Ions*. PhD thesis, University of Maryland, 2016.

[33] J. D. Siverns, L. R. Simkins, S. Weidt, and W. K. Hensinger. On the application of radio frequency voltages to ion traps via helical resonators. *Applied Physics B*, 107(4):921–934, Jun 2012.

[34] W. W. Macalpine and R. O. Schildknecht. Coaxial resonators with helical inner conductor. *Proceedings of the IRE*, 47(12):2099–2105, Dec 1959.

[35] Modeling of a 3D Inductor. https://www.comsol.com/model/modeling-of-a-3d-inductor-10299. Accessed: 2019-07-17.

[36] P. Sippel C. Dichtl and S. Krohns. Dielectric Properties of 3D Printed Polylactic Acid . *Advances in Materials Science and Engineering*, 2017.

[37] G. Janik, W. Nagourney, and H. Dehmelt. Doppler-free optical spectroscopy on the ba+ mono-ion oscillator. *J. Opt. Soc. Am. B*, 2(8):1251–1257, Aug 1985.

[38] EMVA 1288 Overview: Imaging Performance. https://www.flir.com/discover/iis/machine-vision/emva-1288-overview-imaging-performance/. Accessed: 2019-07-18.

[39] P. J. Low, Brendan M. W., A. Cox, M. L. Day, and C. Senko. Practical trapped-ion protocols for universal qudit-based quantum computing. *arXiv e-prints*, page arXiv:1907.08569, Jul 2019.

[40] S. G. Schirmer, A. D. Greentree, V. Ramakrishna, and H. Rabitz. Constructive control of quantum systems using factorization of unitary operators. *Journal of Physics A: Mathematical and General*, 35(39):8315–8339, sep 2002.

[41] M. Howard and J. Vala. Qudit versions of the qubit $\pi/8$ gate. *Phys. Rev. A*, 86:022316, Aug 2012.

[42] R. Blatt and G. Werth. Precision determination of the ground-state hyperfine splitting in $^{137}Ba^{+}$ using the ion-storage technique. *Phys. Rev. A*, 25:1476–1482, Mar 1982.

[43] D. A. Steck. Quantum and atom optics. available online at http://steck.us/teaching (revision 0.12.6, 23 April 2019).

[44] T. Monz. *Quantum information processing beyond ten ion-qubits*. PhD thesis, University of Innsbruck, 2011.

[45] T. Ruster, C. T. Schmiegelow, H. Kaufmann, C. Warschburger, F. Schmidt-Kaler, and U. G. Poschinger. A long-lived zeeman trapped-ion qubit. *Applied Physics B*, 122(10):254, Sep 2016.

[46] R. Ozeri, W. M. Itano, R. B. Blakestad, J. Britton, J. Chiaverini, J. D. Jost, C. Langer, D. Leibfried, R. Reichle, S. Seidelin, J. H. Wesenberg, and D. J. Wineland. Errors in trapped-ion quantum gates due to spontaneous photon scattering. *Phys. Rev. A*, 75:042329, Apr 2007.

[47] P. L. Knight, E. A. Hinds, M. B. Plenio, D. J. Wineland, M. Barrett, J. Britton, J. Chiaverini, B. DeMarco, W. M. Itano, B. Jelenkovi, C. Langer, D. Leibfried, V. Meyer, T. Rosenband, and T. Schtz. Quantum information processing with trapped ions. *Philos. Trans. R. Soc. London, Ser. A*, 361(1808):1349–1361, 2003.

[48] A. Kramida, Yu. Ralchenko, J. Reader, and and NIST ASD Team. NIST Atomic Spectra Database (ver. 5.6.1), [Online]. Available: `https://physics.nist.gov/asd` [2018, July 05]. National Institute of Standards and Technology, Gaithersburg, MD., 2018.

[49] J.-L. Brylinski and R. Brylinski. Universal quantum gates. 09 2001.

[50] P. C. Haljan, K.-A. Brickman, L. Deslauriers, P. J. Lee, and C. Monroe. Spin-dependent forces on trapped ions for phase-stable quantum gates and entangled states of spin and motion. *Phys. Rev. Lett.*, 94:153602, Apr 2005.

[51] R. T. Sutherland, R. Srinivas, S. C. Burd, D. Leibfried, A. C. Wilson, D. J. Wineland, D. T. C. Allcock, D. H. Slichter, and S. B. Libby. Versatile laser-free trapped-ion entangling gates. *New Journal of Physics*, 21(3):033033, mar 2019.

[52] D.F.V. James. Quantum dynamics of cold trapped ions with application to quantum computation. *Applied Physics B*, 66(2):181–190, Feb 1998.

[53] S. Blanes, F. Casas, J. A. Oteo, and J. Ros. The magnus expansion and some of its applications. *Physics Reports*, 470(5):151 – 238, 2009.

[54] D. M. Meekhof, C. Monroe, B. E. King, W. M. Itano, and D. J. Wineland. Generation of nonclassical motional states of a trapped atom. *Phys. Rev. Lett.*, 76:1796–1799, Mar 1996.

[55] C. Senko. *Dynamics and excited states of quantum many-body spin systems with trapped ions*. PhD thesis, University of Maryland, 2014.

[56] T. Choi, S. Debnath, T. A. Manning, C. Figgatt, Z.-X. Gong, L.-M. Duan, and C. Monroe. Optimal quantum control of multimode couplings between trapped ion qubits for scalable entanglement. *Phys. Rev. Lett.*, 112:190502, May 2014.

[57] C. D. Bruzewicz, J. Chiaverini, R. McConnell, and J. M. Sage. Trapped-ion quantum computing: Progress and challenges. *Applied Physics Reviews*, 6(2):021314, 2019.

[58] M. Drewsen, C. Brodersen, L. Hornekaer, J. S. Hangst, and J. P. Schifffer. Large ion crystals in a linear paul trap. *Physical Review Letters - PHYS REV LETT*, 81:2878–2881, 10 1998.

[59] R. Loudon. *The Quantum Theory of Light*. Oxford, 1983.

APPENDICES

Appendix A

Raman Transition Rabi Frequency - Electric Field Relation

In this appendix, the relation between the Rabi frequency of a Raman transition and the electric field amplitudes of the Raman beams is derived for Ba^+ ion in terms of the reduced transition matrix element $\langle 6P, L=1|\hat{d}|6S, L=0\rangle$. The angular momentum of a hyperfine state, $\vec{F}$, can be decomposed to

$$\vec{F} = \vec{I} + \vec{J} = \vec{I} + \vec{L} + \vec{S} \tag{A.1}$$

where $\vec{I}$ is the nuclear spin, $\vec{L}$ is the electron orbital angular momentum, and $\vec{S}$ is the electron spin. The Rabi frequency for a Raman transition is

$$\Omega = \frac{1}{2\hbar^2} \frac{\langle e|\vec{d}\cdot\xi_r\hat{\epsilon}_r|i\rangle\langle i|\vec{d}\cdot\xi_b\hat{\epsilon}_b|g\rangle}{\Delta_i} \tag{A.2}$$

where $|g\rangle$ and $|e\rangle$ are the ground and excited states that the Raman transition is driving. $|i\rangle$ is the high energy state that the Raman transition off-resonantly couples to. $\vec{d}$ is the electric dipole in the spherical basis. Δ_i is the detuning of the Raman laser frequencies from the $|i\rangle$ state.

For $^{137}Ba^+$, in our case, $|g\rangle$ is a level in the $|6S_{1/2}, F=1\rangle$ state, $|e\rangle$ is a level in the $|6S_{1/2}, F=2\rangle$ state, and $|i\rangle$ is any level in the $6P_{1/2}$ and $6P_{3/2}$ states. Since there are multiple $|i\rangle$ states, the net Rabi frequency is the summation of the coupling to all the $|i\rangle$ states

$$\Omega = \frac{1}{2\hbar^2} \sum_i \frac{\langle e|\vec{d}\cdot\xi_r\hat{\epsilon}_r|i\rangle\langle i|\vec{d}\cdot\xi_b\hat{\epsilon}_b|g\rangle}{\Delta_i} \tag{A.3}$$

From Equation A.3, the transition matrix element for off-resonant coupling to each of the $|i\rangle = |6P_{1/2}, F, m_F\rangle$ and $|i\rangle = |6P_{3/2}, F, m_F\rangle$ has to be known for all values of F and m_F, where m_F is the projection of the angular momentum to the quantization axis. This makes evaluating the summation in Equation A.3 difficult as there are many $|i\rangle$ states to couple to. To circumvent this, the transition matrix element can be expressed in terms of the reduced transition matrix element which only depends on the orbital angular momentum.

First, the Wigner-Eckart theorem says that

$$\langle F, m_F|T_q^{(k)}|F', m'_F\rangle = \langle F||T^{(k)}||F'\rangle\langle F', m'_F, k, q|F, m_F\rangle \tag{A.4}$$

where $T_q^{(k)}$ is a spherical tensor operator of rank k of the q^{th} component. In our case, $T_q^{(k)} = \vec{d}\cdot\hat{\epsilon}_q$. Its rank is $k = 1$ since it is a vector operator and q denotes its (spherical) polarization. $\langle F', m'_F, k, q|F, m_F\rangle$ is the Clebsch-Gordan coefficient. $\langle F||T^{(k)}||F'\rangle$ is the reduced transition dipole moment coupling $|F\rangle$ and $|F'\rangle$ states, and is independent of m_F and m'_F. With this, the original transition matrix element is reduced to the form only dependent on F and F' multiplied by the Clebsch-Gordan coefficient. $\langle F||T^{(k)}||F'\rangle$ can be further reduced to a form dependent only on the J component of the angular momentum. Multiplying Equation A.4 by $\langle F, m_F|F', m'_F, k, q\rangle$ and summing over q and m'_F gives

$$\begin{aligned}\sum_{q,m'_F}\langle F||T^{(k)}||F'\rangle\langle F, m_F|F', m'_F, k, q\rangle\langle F', m'_F, k, q|F, m_F\rangle \\ = \sum_{q,m'_F}\langle F, m_F|T_q^{(k)}|F', m'_F\rangle\langle F, m_F|F', m'_F, k, q\rangle\end{aligned} \tag{A.5}$$

Note that $\sum_{q,m'_F}|F', m'_F, k, q\rangle\langle F', m'_F, k, q|$ is the identity matrix for the state $|F, m_F\rangle$. Thus, the Equation A.5 reduces to

$$\langle F||T^{(k)}||F'\rangle = \sum_{q,m'_F}\langle F, m_F|T_q^{(k)}|F', m'_F\rangle\langle F, m_F|F', m'_F, k, q\rangle \tag{A.6}$$

Inserting more identity matrices before and after $T_q^{(k)}$ gives

$$\begin{aligned}\langle F||T^{(k)}||F'\rangle &= \sum_{q,m'_F}\langle F, m_F|\hat{I}T_q^{(k)}\hat{I}|F', m'_F\rangle\langle F, m_F|F', m'_F, k, q\rangle \\ &= \sum_{q,m'_F,m_J,m_I,m'_J,m'_I}\langle F, m_F|J, m_J, I, m_I\rangle\langle J, m_J, I, m_I|T_q^{(k)}|J', m'_J, I', m'_I\rangle \\ &\times \langle J', m'_J, I', m'_I|F', m'_F\rangle\langle F, m_F|F', m'_F, k, q\rangle\end{aligned} \tag{A.7}$$

If the tensor operator is acting on the J state only, then we can write the equation as

$$\begin{aligned}\langle F||T^{(k)}||F'\rangle = &\sum_{q,m'_F,m_J,m_I,m'_J,m'_I} \langle F,m_F|J,m_J,I,m_I\rangle\langle J',m'_J,I',m'_I|F',m'_F\rangle \\ &\times \langle F,m_F|F',m'_F,k,q\rangle\langle I,m_I|I',m'_I\rangle\langle J,m_J|T^{(k)}_q|J',m'_J\rangle \\ = &\sum_{q,m'_F,m_J,m_I,m'_J} \langle F,m_F|J,m_J,I,m_I\rangle\langle J',m'_J,I',m'_I|F',m'_F\rangle \\ &\times \langle F,m_F|F',m'_F,k,q\rangle\langle J,m_J|T^{(k)}_q|J',m'_J\rangle\end{aligned} \tag{A.8}$$

$\langle J,m_J|T^{(k)}_q|J',m'_J\rangle$ can be further reduced by applying the Wigner-Eckart theorem again,

$$\langle J,m_J|T^{(k)}_q|J',m'_J\rangle = \langle J||T^{(k)}||J'\rangle\langle J',m'_J,k,q|J,m_J\rangle \tag{A.9}$$

which gives

$$\begin{aligned}\langle F||T^{(k)}||F'\rangle = &\langle J||T^{(k)}||J'\rangle \\ &\times \sum_{q,m'_F,m_J,m_I,m'_J} \langle F,m_F|J,m_J,I,m_I\rangle\langle J',m'_J,I',m'_I|F',m'_F\rangle \\ &\times \langle F,m_F|F',m'_F,k,q\rangle\langle J',m'_J,k,q|J,m_J\rangle\end{aligned} \tag{A.10}$$

Equation A.10 gives the reduction of the transition matrix element in F to J form. The summation series in Equation A.10 is related to the Wigner-6j symbol by

$$\begin{aligned}&\sum_{q,m'_F,m_J,m_I,m'_J} \langle F,m_F|J,m_J,I,m_I\rangle\langle J',m'_J,I',m'_I|F',m'_F\rangle \\ &\qquad\times \langle F,m_F|F',m'_F,k,q\rangle\langle J',m'_J,k,q|J,m_J\rangle \\ &\qquad= (-1)^{F'+J+k+I}\sqrt{(2F'+1)(2J+1)}\begin{Bmatrix} J & J' & k \\ F' & F & I\end{Bmatrix}\end{aligned} \tag{A.11}$$

where $\begin{Bmatrix} J & J' & k \\ F' & F & I\end{Bmatrix}$ is the Wigner-6j symbol. The final equation relating the transition matrix element in the $\langle F,m_F|T^{(k)}_q|F',m'_F\rangle$ form to $\langle J||T^{(k)}||J'\rangle$ form is then

$$\begin{aligned}\langle F,m_F|T^{(k)}_q|F',m'_F\rangle = &\langle J||T^{(k)}||J'\rangle\langle F',m'_F,k,q|F,m_F\rangle \\ &\times (-1)^{F'+J+k+I}\sqrt{(2F'+1)(2J+1)}\begin{Bmatrix} J & J' & k \\ F' & F & I\end{Bmatrix}\end{aligned} \tag{A.12}$$

To further reduce the transition matrix element to the form $\langle L||T^{(k)}||J'\rangle$, the same method can be used to derive the form

$$\langle J||T^{(k)}||J'\rangle = \langle L||T^{(k)}||L'\rangle(-1)^{J'+L+k+S}\sqrt{(2J'+1)(2L+1)}\begin{Bmatrix} L & L' & k \\ J' & J & S \end{Bmatrix} \tag{A.13}$$

With Equations A.13 and A.10, a transition matrix element in the form $\langle 6P, F, m_F|\vec{d}\cdot\hat{\epsilon}_q|6S, F', m'_F\rangle$ can be reduced to the form $\langle 6P, L||\hat{d}||6S, L'\rangle$ (where $\vec{d}$ has been rewritten as an operator $\hat{d}$) with a corresponding coefficient. Equations 5.16 and 5.21 can then be derived from Equation A.3 after reducing the transition matrix element with Equations A.13 and A.10.

Appendix B

Scattering in Terms of Ground State Population

The total spontaneous emission rate is given by [47]

$$R_{SE} = \sum_i \gamma_i P_i \tag{B.1}$$

where γ_n is the decay rate in the excited state $|i\rangle$ and P_i is the probability that the $|i\rangle$ state is populated. In this case, the $|i\rangle$ states are the $6P_{1/2}$ and $6P_{3/2}$ states. To derive P_i, a simple 2-level system with a ground state $|g\rangle$ and an excited state $|e\rangle$. Consider also an electric dipole perturbation introduced by a laser beam of the form

$$\hat{H}_{pert} = \hat{d} \cdot \xi_0 \hat{\epsilon} \cos(\omega_R t) \tag{B.2}$$

where $\hat{d}$ is the dipole moment operator, ξ_0 is the electric field amplitude of the laser beam, ϵ is the polarization of the laser beam, and ω_R is the laser frequency. The Hamiltonian for this system is

$$\hat{H} = \hat{H}_0 + \hat{H}_{pert} \tag{B.3}$$

where $\hat{H}_0$ is the static Hamiltonian. The general quantum state of the system is written as

$$|\psi\rangle = a(t)\, e^{-i\frac{E_g}{\hbar}t}|g\rangle + b(t)\, e^{-i\frac{E_e}{\hbar}t}|e\rangle \tag{B.4}$$

where $a(t)$ and $b(t)$ are the probability amplitudes for the states $|g\rangle$ and $|e\rangle$ respectively. E_g and E_e are the energies of the $|g\rangle$ and $|e\rangle$ states in the static Hamiltonian. From Schrödinger's equation,

$$i\hbar\frac{d}{dt}|\psi\rangle = \hat{H}|\psi\rangle \tag{B.5}$$

Evaluating the LHS of Schrödinger's equation gives

$$i\hbar\frac{d}{dt}|\psi\rangle = a\left(t\right)E_g e^{-i\frac{E_g}{\hbar}t}|g\rangle + b\left(t\right)E_e e^{-i\frac{E_e}{\hbar}t}|e\rangle + i\hbar\left(\dot{a}\left(t\right)e^{-i\frac{E_g}{\hbar}t}|g\rangle + \dot{b}\left(t\right)e^{-i\frac{E_e}{\hbar}t}|e\rangle\right) \quad \text{(B.6)}$$

The RHS of Schrödinger's equation is

$$\begin{aligned}\hat{H}|\psi\rangle &= \left(\hat{H}_0 + \hat{H}_{pert}\right)|\psi\rangle \\ &= a\left(t\right)E_g e^{-i\frac{E_g}{\hbar}t}|g\rangle + b\left(t\right)E_e e^{-i\frac{E_e}{\hbar}t}|e\rangle + a\left(t\right)\hat{H}_{pert}e^{-i\frac{E_g}{\hbar}t}|g\rangle + b\left(t\right)\hat{H}_{pert}e^{-i\frac{E_e}{\hbar}t}|e\rangle\end{aligned} \quad \text{(B.7)}$$

Comparing Equations B.6 and B.7 gives

$$i\hbar\left(\dot{a}\left(t\right)e^{-i\frac{E_g}{\hbar}t}|g\rangle + \dot{b}\left(t\right)e^{-i\frac{E_e}{\hbar}t}|e\rangle\right) = a\left(t\right)\hat{H}_{pert}e^{-i\frac{E_g}{\hbar}t}|g\rangle + b\left(t\right)\hat{H}_{pert}e^{-i\frac{E_e}{\hbar}t}|e\rangle \quad \text{(B.8)}$$

Multiplying $\langle e|$ from the LHS of Equation B.8 gives

$$i\hbar\dot{b}\left(t\right)e^{-i\frac{E_e}{\hbar}t} = a\left(t\right)e^{-i\frac{E_g}{\hbar}t}\langle e|\hat{H}_{pert}|g\rangle + b\left(t\right)e^{-i\frac{E_e}{\hbar}t}\langle e|\hat{H}_{pert}|e\rangle \quad \text{(B.9)}$$

For an electric dipole perturbation, $\langle e|\hat{H}_{pert}|e\rangle = 0$. Thus,

$$\dot{b}\left(t\right) = -\frac{i}{\hbar}a\left(t\right)e^{i\omega_0 t}\langle e|\hat{H}_{pert}|g\rangle \quad \text{(B.10)}$$

where $\omega_0 = \frac{E_e - E_g}{\hbar}$. Plugging Equation B.2 into Equation B.10 gives

$$\dot{b}\left(t\right) = -i\frac{\xi_0}{\hbar}e^{i\omega_0 t}\langle e|\hat{d}\cdot\hat{\epsilon}|g\rangle \quad \text{(B.11)}$$

Note that the rate equation for the excited state wavefunction amplitude in Equation B.11 only takes into account perturbation from the laser beam and not the spontaneous decay of the state. To include spontaneous decay, Equation B.11 is modified to [59]

$$\dot{b}\left(t\right) = -i\frac{\xi_0}{\hbar}e^{i\omega_0 t}\langle e|\hat{d}\cdot\hat{\epsilon}|g\rangle \rightarrow \dot{b}\left(t\right) = -i\frac{\xi_0}{\hbar}e^{i\omega_0 t}\langle e|\hat{d}\cdot\hat{\epsilon}|g\rangle - \frac{1}{2}\gamma b\left(t\right) \quad \text{(B.12)}$$

Multiplying a factor of $e^{\frac{1}{2}\gamma t}$ to Equation B.12 and rearranging the terms give

$$e^{\frac{1}{2}\gamma t}\dot{b}\left(t\right) + \frac{1}{2}\gamma e^{\frac{1}{2}\gamma t}b\left(t\right) = -e^{\frac{1}{2}\gamma t}\frac{i\xi_0}{\hbar}\cos\left(\omega_R t\right)e^{i\omega_0 t}\langle e|\hat{d}\cdot\hat{\epsilon}|g\rangle \quad \text{(B.13)}$$

which implies

$$\frac{d}{dt}\left(e^{\frac{1}{2}\gamma t}b\left(t\right)\right)=-e^{\frac{1}{2}\gamma t}\frac{i\xi_0}{\hbar}\cos\left(\omega_R t\right)e^{i\omega_0 t}\langle e|\hat{d}\cdot\hat{\epsilon}|g\rangle \tag{B.14}$$

Integrating Equation B.14 gives

$$e^{\frac{1}{2}\gamma t}b\left(t\right)=-\frac{i\xi_0}{2\hbar}\langle e|\hat{d}\cdot\hat{\epsilon}|g\rangle\left[\frac{\exp\left(\frac{1}{2}\gamma t+i\left(\omega_0-\omega_R\right)t\right)-1}{\frac{1}{2}\gamma+i\left(\omega_0-\omega_R\right)}+\frac{\exp\left(\frac{1}{2}\gamma t+i\left(\omega_0+\omega_R\right)t\right)-1}{\frac{1}{2}\gamma+i\left(\omega_0+\omega_R\right)}\right] \tag{B.15}$$

For the case where $|\omega_R-\omega_0|\ll\omega_R+\omega_0$, the term $\frac{\exp\left(\frac{1}{2}\gamma t+i(\omega_0+\omega_R)t\right)-1}{\frac{1}{2}\gamma+i(\omega_0+\omega_R)}$ can be neglected with RWA and the following is obtained

$$b\left(t\right)\approx-\frac{\xi_0}{2\hbar}\langle e|\hat{d}\cdot\hat{\epsilon}|g\rangle\left(\frac{e^{i(\omega_0-\omega_R)t}-e^{-\frac{1}{2}\gamma t}}{\omega_0-\omega_R-i\frac{1}{2}\gamma}\right) \tag{B.16}$$

The probability of populating the excited state is then

$$\left|b\left(t\right)\right|^2=\frac{\xi_0^2}{4\hbar^2}|\langle e|\hat{d}\cdot\hat{\epsilon}|g\rangle|^2\frac{1-2e^{-\frac{1}{2}\gamma t}\cos\left(\left(\omega_0-\omega_R\right)t\right)+e^{-\gamma t}}{\left(\omega_0-\omega_R\right)^2+\gamma^2/4} \tag{B.17}$$

The average probability of populating the excited state is

$$\langle\left|b\left(t\right)\right|^2\rangle=\frac{\xi_0^2}{4\hbar^2}|\langle e|\hat{d}\cdot\hat{\epsilon}|g\rangle|^2\frac{1-\langle2e^{-\frac{1}{2}\gamma t}\cos\left(\left(\omega_0-\omega_R\right)t\right)\rangle+\langle e^{-\gamma t}\rangle}{\left(\omega_0-\omega_R\right)^2+\gamma^2/4} \tag{B.18}$$

For a gate time that is short with respect to the decay rate, i.e. $e^{-\gamma t}\approx1$, and $|\omega_0-\omega_R|\gg\frac{1}{2}\gamma$, we have $\langle2e^{-\frac{1}{2}\gamma t}\cos\left(\left(\omega_0-\omega_R\right)t\right)\rangle\approx0$ and $\langle e^{-\gamma t}\rangle\approx1$, we have

$$\langle\left|b\left(t\right)\right|^2\rangle=\frac{\xi_0^2}{2\hbar^2}|\langle e|\hat{d}\cdot\hat{\epsilon}|g\rangle|^2\frac{1}{\left(\omega_0-\omega_R\right)^2} \tag{B.19}$$

For the case where the gate time is long with respect to the decay rate, i.e. $\gamma t\gg1$, we have $\langle2e^{-\frac{1}{2}\gamma t}\cos\left(\left(\omega_0-\omega_R\right)t\right)\rangle\approx0$ and $\langle e^{-\gamma t}\rangle\approx0$. The average probability of populating the excited state is then

$$\langle\left|b\left(t\right)\right|^2\rangle=\frac{\xi_0^2}{4\hbar^2}|\langle e|\hat{d}\cdot\hat{\epsilon}|g\rangle|^2\frac{1}{\left(\omega_0-\omega_R\right)^2+\gamma^2/4} \tag{B.20}$$

For $|\omega_0 - \omega_R| \gg \frac{1}{2}\gamma$, we arrive at the form that is in agreement with Ref. [47]

$$\langle |b(t)|^2 \rangle = \frac{\xi_0^2}{4\hbar^2} |\langle e|\hat{d}\cdot\hat{\epsilon}|g\rangle|^2 \frac{1}{(\omega_0 - \omega_R)^2} \tag{B.21}$$

For $^{137}Ba^+$, the decay rates from the 6P states are in the order of 100 MHz and the gate times for our single and two-qudit gates are in the order of 100 μs. The detuning of the Raman frequency from the 6P states are in the order of 10 THz. Thus, Equation B.21 applies for in this case.

In the case of the qudit entangling gate, the encoded states in the $6S$ levels can be treated as the ground states and the $6P$ states are the excited states. Since there are multiple ground states, the probability of populating an excited state $|i\rangle$ state is contributed by the sum of the qudit states. For only one laser frequency, P_i can be expressed as

$$P_i = \sum_l P_l \frac{\xi_0^2}{4\hbar^2 (\omega_R - \omega_0)^2} |\langle e|\hat{d}\cdot\hat{\epsilon}|g\rangle|^2 \tag{B.22}$$

where P_l is the probability that an ion is in the state $|l\rangle$. Since we are applying multiple laser frequencies for the qudit entangling gate, the expression for P_i is ultimately

$$P_i = \sum_j \sum_l P_l \frac{\xi_{0,j}^2}{4\hbar^2 (\omega_{R,j} - \omega_0)^2} |\langle e|\hat{d}\cdot\hat{\epsilon}_j|g\rangle|^2 \tag{B.23}$$

The spontaneous emission rate is then

$$R_{SE} = \sum_i \sum_j \sum_l \gamma_i P_l \frac{\xi_j^2}{4\hbar^2 (\omega_{R,j} - \omega_{l,i})^2} |\langle i|\hat{d}\cdot\hat{\epsilon}_j|l\rangle|^2 \tag{B.24}$$

where ω_{li} is the transition frequency between states $|l\rangle$ and $|i\rangle$. Since the hyperfine splitting is approximately 8 GHz whereas the energy differences between the $6P$ and $6S$ states are in the order of terahertz, $\omega_{li} \approx \omega_{l'i}$ for any $|l\rangle$ and $|l'\rangle$. Thus, a single parameter, ω_i can be used to approximate transition frequency from any state $|l\rangle$ to a state $|i\rangle$. The approximation $|\omega_{R,j} - \omega_{R,j'}| \ll |\omega_{R,j} - \omega_i|$ can also be applied due to the small hyperfine splitting as compared to the energy separation between $6P$ and $6S$ states. Thus, a single ω_R can be used to approximate the laser frequencies applied. This gives

$$R_{SE} = \sum_i \sum_j \sum_l \gamma_i P_l \frac{\xi_j^2}{4\hbar^2 (\omega_R - \omega_i)^2} |\langle i|\hat{d}\cdot\hat{\epsilon}_j|l\rangle|^2 \tag{B.25}$$

Applying the method of reducing transition matrix element in Appendix A to Equation B.25 gives Equations 5.14 and 5.20.

Appendix C

Unwanted Resonance for 5-level Entangling Gate

In Chapter 6, it is stated that the 5-level qudit entangling gate fails with the encoding scheme as shown in Figure C.1. Laser perturbations with frequencies as shown in Figure C.1 are applied to implement the entangling gate. However, there are some (unwanted) frequencies in each transition that are allowed by selection rules. For example, the required right and left-circularly polarized light acting on state $|3\rangle$ for the entangling gate acts on state $|1\rangle$ too, but at unwanted frequencies for $|1\rangle$ state. For the transitions $|0\rangle \rightarrow |1\rangle$ and $|1\rangle \rightarrow |2\rangle$, two additional blue-detuned off-resonant frequencies are introduced to each of the transition, whereas two additional red-detuned off-resonant frequencies are introduced to each of the transitions $|2\rangle \rightarrow |3\rangle$ and $|3\rangle \rightarrow |4\rangle$.

From Equations 6.13 and 6.12, the off resonant frequencies modify the ideal Hamiltonian in Equation 6.3 to

$$\begin{aligned}\hat{H} &= \hat{H}_{ideal} + \hat{H}_{OR} \\ \hat{H}_{OR} &= \frac{\hbar\Omega}{2}\sum_{n=1}^{N}\sum_{j=1}^{2}\left(\sum_{l=0}^{1} C_l\left[e^{-i(-1)^l(k\hat{x}'_n-\mu_j t-\frac{\pi}{2})}|l+1\rangle\langle l|_n + e^{i(-1)^l(k\hat{x}'-\mu_j t-\frac{\pi}{2})}|l\rangle\langle l+1|_n\right]\right. \\ &\quad \left. + \sum_{l=2}^{3} C_l\left[e^{-i(-1)^l(k\hat{x}'_n+\mu_j t-\frac{\pi}{2})}|l+1\rangle\langle l|_n + e^{i(-1)^l(k\hat{x}'+\mu_j t-\frac{\pi}{2})}|l\rangle\langle l+1|_n\right]\right)\end{aligned} \tag{C.1}$$

where $\mu_1 = 4\Delta_z - \mu$, $\mu_2 = 4\Delta_z + \mu$, $C_0 = C_3 = 6$, $C_1 = C_2 = \frac{\sqrt{6}}{3}$, and the quantity Δ_z is the energy of the Zeeman splitting in frequency. We further simplify the problem by letting

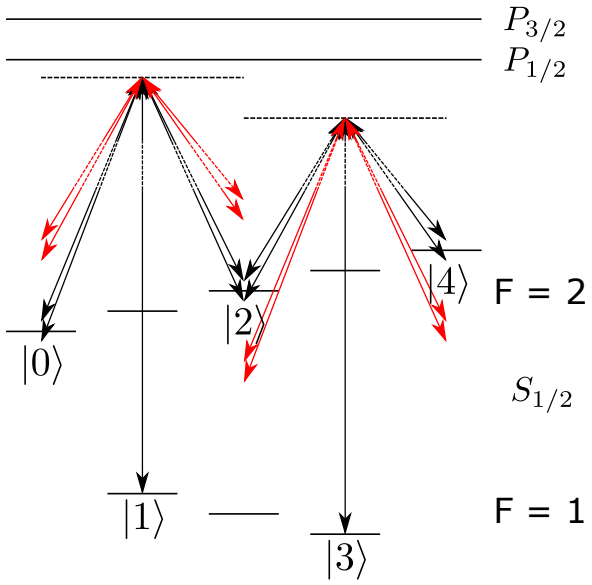

Figure C.1: Schematic of laser frequencies applied to implement a 5-level qudit entangling gate for $^{137}Ba^{+}$. Black arrows indicate the desired frequencies to be applied to the energy levels. Red arrows are the (unwanted) off-resonant frequencies.

$\Delta k\hat{x}' \to 0$ in the off-resonant component of the Hamiltonian. We employ the Magnus expansion again to evaluate the time-evolution operator generated by this Hamiltonian.

The first term in the Magnus expansion is

$$\begin{aligned} M_1(t) &= -\frac{i}{\hbar}\int_0^t \hat{H}_{ideal}(t_1) + \hat{H}_{OR}(t_1)\, dt_1 \\ &= \left(\alpha(t)\hat{a}^\dagger - \alpha^*(t)\hat{a}\right)\sum_{n=1}^{N}\hat{S}_{x,n} \\ &\quad + \frac{\hbar\Omega}{2}\sum_{n=1}^{N}\sum_{j=1}^{2}\left(\sum_{l=0}^{1}\frac{C_l}{\mu_j}\left[(e^{i(-1)^l\mu_j t}-1)|l+1\rangle\langle l|_n + (e^{-i(-1)^l\mu_j t}-1)|l\rangle\langle l+1|_n\right]\right. \\ &\quad \left. + \sum_{l=2}^{3}\frac{C_l}{\mu_j}\left[(1-e^{-i(-1)^l\mu_j t})|l+1\rangle\langle l|_n + (1-e^{i(-1)^l\mu_j t})|l\rangle\langle l+1|_n\right]\right). \end{aligned} \tag{C.2}$$

By changing the laser frequencies or Zeeman splitting, such that $(1-e^{\pm i(-1)^l\mu_j t}) = 0$ when $t = K\frac{2\pi}{|\omega_M-\mu|}$, it is still possible to minimize the error contribution of the off-resonant

frequencies in the first Magnus expansion. The second order Magnus expansion with this Hamiltonian is

$$\begin{aligned} M_2(t) &= -\frac{1}{2\hbar^2}\int_0^t dt_1 \int_0^{t_1} \left[\hat{H}_{ideal}(t_1)+\hat{H}_{OR}(t_1), \hat{H}_{ideal}(t_2)+\hat{H}_{OR}(t_2)\right] dt_2 \\ &= -\frac{1}{2\hbar^2}\int_0^t dt_1 \int_0^{t_1} \left[\hat{H}_{ideal}(t_1), \hat{H}_{ideal}(t_2)\right] + \left[\hat{H}_{ideal}(t_1), \hat{H}_{OR}(t_2)\right] \\ &+ \left[\hat{H}_{OR}(t_1), \hat{H}_{ideal}(t_2)\right] + \left[\hat{H}_{OR}(t_1), \hat{H}_{OR}(t_2)\right] dt_2. \end{aligned} \tag{C.3}$$

The first term in the integral is the desired term, which is found in Equation 6.30. For the rest of the terms, $\int_0^t dt_1 \int_0^{t_1} \left[\hat{H}_{ideal}(t_1), \hat{H}_{OR}(t_2)\right] + \left[\hat{H}_{OR}(t_1), \hat{H}_{ideal}(t_2)\right] dt_2$ result in terms that are bounded with t. Evaluating $\left[\hat{H}_{OR}(t_1), \hat{H}_{OR}(t_2)\right]$ gives

$$\begin{aligned} &\hat{H}_{OR}(t_1)\hat{H}_{OR}(t_2) \\ &= \frac{\hbar^2\bar{\Omega}^2}{4}\sum_{n=1}^{N}\sum_{j=1}^{2}\sum_{j'=1}^{2}\left(\sum_{l=0}^{1} C_l^2\left[e^{i(-1)^l(\mu_j t_1-\mu_{j'}t_2)}|l+1\rangle\langle l+1|_n + e^{-i(-1)^l(\mu_j t_1-\mu_{j'}t_2)}|l\rangle\langle l|_n\right]\right. \\ &+ \sum_{l=2}^{3} C_l^2\left[e^{-i(-1)^l(\mu_j t_1+\mu_{j'}t_2)}|l+1\rangle\langle l+1|_n + e^{i(-1)^l(\mu_j t_1-\mu_{j'}t_2)}|l\rangle\langle l|_n\right] \\ &+ C_0C_1\left(e^{-i(\mu_j t_1-\mu_{j'}t_2)}|0\rangle\langle 2|_n + e^{-i(\mu_j t_1-\mu_{j'}t_2)}|2\rangle\langle 0|_n\right) \\ &+ C_1C_2\left(e^{-i(\mu_j t_1+\mu_{j'}t_2)}|1\rangle\langle 3|_n + e^{i(\mu_j t_1+\mu_{j'}t_2)}|3\rangle\langle 1|_n\right) \\ &\left.+ C_2C_3\left(e^{i(\mu_j t_1-\mu_{j'}t_2)}|2\rangle\langle 4|_n + e^{i(\mu_j t_1-\mu_{j'}t_2)}|4\rangle\langle 2|_n\right)\right) \end{aligned} \tag{C.4}$$

With this, the commutator, $\left[\hat{H}_{OR}(t_1), \hat{H}_{OR}(t_2)\right]$, is

$$\begin{aligned}
&\left[\hat{H}_{OR}(t_1), \hat{H}_{OR}(t_2)\right] \\
&= \frac{i\hbar^2\bar{\Omega}^2}{2} \sum_{n=1}^{N} \sum_{j=1}^{2} \sum_{j'=1}^{2} \left(\sum_{l=0}^{1} C_l^2 \left[(-1)^l \sin\left(\mu_j t_1 - \mu_{j'} t_2\right) |l+1\rangle\langle l+1|_n \right.\right. \\
&- \left. (-1)^l \sin\left(\mu_j t_1 - \mu_{j'} t_2\right) |l\rangle\langle l|_n \right] \\
&+ \sum_{l=2}^{3} C_l^2 \left[-(-1)^l \sin\left(\mu_j t_1 - \mu_{j'} t_2\right) |l+1\rangle\langle l+1|_n + (-1)^l \sin\left(\mu_j t_1 - \mu_{j'} t_2\right) |l\rangle\langle l|_n \right] \\
&+ C_0 C_1 \left(-\sin\left(\mu_j t_1 - \mu_{j'} t_2\right) |0\rangle\langle 2|_n - \sin\left(\mu_j t_1 - \mu_{j'} t_2\right) |2\rangle\langle 0|_n \right) \\
&\left. + C_2 C_3 \left(\sin\left(\mu_j t_1 - \mu_{j'} t_2\right) |2\rangle\langle 4|_n + \sin\left(\mu_j t_1 - \mu_{j'} t_2\right) |4\rangle\langle 2|_n \right) \right)
\end{aligned} \tag{C.5}$$

The integral of the commutator gives

$$\begin{aligned}
&\int_0^t dt_1 \int_0^{t_1} \left[\hat{H}_{OR}(t_1), \hat{H}_{OR}(t_2)\right] \, dt_2 \\
&= \frac{i\hbar^2\bar{\Omega}^2}{2} \int_0^t \sum_{n=1}^{N} \sum_{j=1}^{2} \sum_{j'=1}^{2} \left(\sum_{l=0}^{1} \frac{C_l^2}{\mu_{j'}} \left[(-1)^l \left(\cos\left(\mu_j t_1 - \mu_{j'} t_1\right) - \cos\left(\mu_j t_1\right) \right) |l+1\rangle\langle l+1|_n \right.\right. \\
&- \left. (-1)^l \left(\cos\left(\mu_j t_1 - \mu_{j'} t_1\right) - \cos\left(\mu_j t_1\right) \right) |l\rangle\langle l|_n \right] \\
&+ \sum_{l=2}^{3} \frac{C_l^2}{\mu_{j'}} \left[-(-1)^l \left(\cos\left(\mu_j t_1 - \mu_{j'} t_1\right) - \cos\left(\mu_j t_1\right) \right) |l+1\rangle\langle l+1|_n \right. \\
&+ \left. (-1)^l \left(\cos\left(\mu_j t_1 - \mu_{j'} t_1\right) - \cos\left(\mu_j t_1\right) \right) |l\rangle\langle l|_n \right] \\
&+ \frac{C_0 C_1}{\mu_{j'}} \left(- \left(\cos\left(\mu_j t_1 - \mu_{j'} t_1\right) - \cos\left(\mu_j t_1\right) \right) |0\rangle\langle 2|_n \right. \\
&- \left(\cos\left(\mu_j t_1 - \mu_{j'} t_1\right) - \cos\left(\mu_j t_1\right) \right) |2\rangle\langle 0|_n \Big) \\
&+ \frac{C_2 C_3}{\mu_{j'}} \left(\left(\cos\left(\mu_j t_1 - \mu_{j'} t_1\right) - \cos\left(\mu_j t_1\right) \right) |2\rangle\langle 4|_n \right. \\
&\left.\left. + \left(\cos\left(\mu_j t_1 - \mu_{j'} t_1\right) - \cos\left(\mu_j t_1\right) \right) |4\rangle\langle 2|_n \right) \right) dt_1
\end{aligned} \tag{C.6}$$

Dropping the terms bounded with t, only the terms $\mu_j = \mu_{j'}$ need to be kept. The integral

can then be approximated to be

$$
\begin{aligned}
&\int_0^t dt_1 \int_0^{t_1} \left[\hat{H}_{OR}(t_1), \hat{H}_{OR}(t_2)\right] \, dt_2 \\
&= \frac{i\hbar^2\bar{\Omega}^2}{2} \int_0^t \sum_{n=1}^{N} \sum_{j=1}^{2} \left(\sum_{l=0}^{1} \frac{C_l^2}{\mu_j} \left[(-1)^l \left(1 - \cos\left(\mu_j t_1\right)\right) |l+1\rangle\langle l+1|_n \right.\right. \\
&- \left.\left. (-1)^l \left(1 - \cos\left(\mu_j t_1\right)\right) |l\rangle\langle l|_n \right] \right. \\
&+ \sum_{l=2}^{3} \frac{C_l^2}{\mu_j} \left[-(-1)^l \left(1 - \cos\left(\mu_j t_1\right)\right) |l+1\rangle\langle l+1|_n + (-1)^l \left(1 - \cos\left(\mu_j t_1\right)\right) |l\rangle\langle l|_n \right] \\
&+ \frac{C_0 C_1}{\mu_j} \left(- \left(1 - \cos\left(\mu_j t_1\right)\right) |0\rangle\langle 2|_n - \left(1 - \cos\left(\mu_j t_1\right)\right) |2\rangle\langle 0|_n \right) \\
&+ \left. \frac{C_2 C_3}{\mu_j} \left(\left(1 - \cos\left(\mu_j t_1\right)\right) |2\rangle\langle 4|_n + \left(1 - \cos\left(\mu_j t_1\right)\right) |4\rangle\langle 2|_n \right) \right) \, dt_1 \\
&\approx \frac{i\hbar^2\bar{\Omega}^2}{2} \int_0^t \sum_{n=1}^{N} \sum_{j=1}^{2} \left(\sum_{l=0}^{1} \frac{C_l^2}{\mu_j} \left[(-1)^l |l+1\rangle\langle l+1|_n - (-1)^l |l\rangle\langle l|_n \right] \right. \\
&+ \sum_{l=2}^{3} \frac{C_l^2}{\mu_j} \left[-(-1)^l |l+1\rangle\langle l+1|_n + (-1)^l |l\rangle\langle l|_n \right] \\
&+ \left. \frac{C_0 C_1}{\mu_j} \left(-|0\rangle\langle 2|_n - |2\rangle\langle 0|_n \right) + \frac{C_2 C_3}{\mu_j} \left(|2\rangle\langle 4|_n + |4\rangle\langle 2|_n \right) \right) \, dt_1 \\
&= \frac{i\hbar^2\bar{\Omega}^2}{2} t \sum_{n=1}^{N} \sum_{j=1}^{2} \left(\sum_{l=0}^{1} \frac{C_l^2}{\mu_j} \left[(-1)^l |l+1\rangle\langle l+1|_n - (-1)^l |l\rangle\langle l|_n \right] \right. \\
&+ \sum_{l=2}^{3} \frac{C_l^2}{\mu_j} \left[-(-1)^l |l+1\rangle\langle l+1|_n + (-1)^l |l\rangle\langle l|_n \right] \\
&+ \left. \frac{C_0 C_1}{\mu_j} \left(-|0\rangle\langle 2|_n - |2\rangle\langle 0|_n \right) + \frac{C_2 C_3}{\mu_j} \left(|2\rangle\langle 4|_n + |4\rangle\langle 2|_n \right) \right)
\end{aligned}
\tag{C.7}
$$

Thus, the contribution of the off-resonant terms to the second-order Magnus expansion is

$$
\begin{aligned}
&-\frac{1}{2\hbar^2}\int_0^t dt_1 \int_0^{t_1} \left[\hat{H}_{OR}(t_1), \hat{H}_{OR}(t_2)\right] \, dt_2 \\
&\approx -\frac{i\Omega^2}{4} t \sum_{n=1}^{N}\sum_{j=1}^{2}\left(\sum_{l=0}^{1}\frac{C_l^2}{\mu_j}\left[-(-1)^l|l\rangle\langle l|_n + (-1)^l|l+1\rangle\langle l+1|_n\right]\right. \\
&+\sum_{l=2}^{3}\frac{C_l^2}{\mu_j}\left[(-1)^l|l\rangle\langle l|_n - (-1)^l|l+1\rangle\langle l+1|_n\right] \\
&\left.-\frac{C_0C_1}{\mu_j}\left(|0\rangle\langle 2|_n + |2\rangle\langle 0|_n\right) + \frac{C_2C_3}{\mu_j}\left(|2\rangle\langle 4|_n + |4\rangle\langle 2|_n\right)\right)
\end{aligned}
\tag{C.8}
$$

which consists of error terms due to Stark shifts and internal transitions of each qudit between $|0\rangle$ and $|2\rangle$ states and between $|2\rangle$ and $|4\rangle$ states. This term is comparable in magnitude to the desired term in the second Magnus expansion in Equation 6.30 and thus introduces a significant error.